Dual Modality CT/SPECT Scanner for Small Animal Imaging

Alexander Vyacheslavovich Stolin
Moscow Russian Federation

Physics Engineer, Moscow Institute of Physics and Technology, 1999

A Dissertation presented to the Graduate Faculty
of the University of Virginia in Candidacy for the Degree of
Doctor of Philosophy

Department of Physics

University of Virginia
May 2007

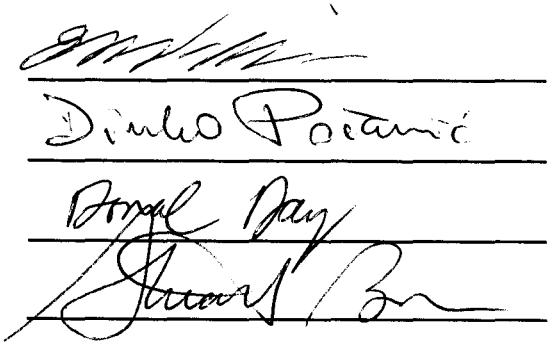

Acknowledgements

I am indebted to many people for their assistance and support in the completion of this work, and I will try to list most them here. First, I would like to thank my research advisor, Professor Mark Williams, who provided me the perfect balance of scientific freedom and careful guidance. I greatly appreciate all the help I got from my colleagues at the UVa Detector Lab – Donald Pole, Patricia Judy, Mitali More, Bijoy Kundu, Deepa Narajanan. Enormous contribution to my work was given by wonderful people from Jefferson Laboratory Detector Group Drs Stan Majewski, Andrew Weisenberger, Randolph Wojcik, Vladimir Popov, Brian Kross, and Benjamin Welch. I would like to thank my collaborators from Brandeis University Drs Alexander Stewart, Walter Phillips, and Martin Stanton for their support and helpful insights. This work would not be completed without help from Physics machine shop at the UVa. I am greatly indebted to Roger Ashley, Benjamin Kent, Frank Henderson and David Wimer for the excellent job they have done for me.

I would also like thank Dr Scott Metzler of University of Pennsylvania for numerous valuable conversations we had during my studies. My fellow graduate students and friends have been an invaluable resource, as well as a source of inspiration and support. I would like to thank Dr Maxim Bychkov for his patience and expertise. I would also like to thank the same person, but now as my friend Max along with his wife Evgenia and their little zoo for all their help and support.I am thankful to the National Institutes of Health (NIH) for funding my PhD research and education through RO1 CA69452-05.

Last but not least I thank my family for their abundant love and support.

Abstract

This work describes the design and performance of a dual-modality system for small animal imaging combining a high spatial resolution SPECT component with an x-ray CT component. All components are mounted on a barrel type gantry which is able to rotate in 0.001 degrees increments about the animal. The SPECT subsystem consists of a four custom-built gamma cameras. The cameras can be equipped with either parallel hole or pinhole collimators depending on the study in question. The cameras can be operated in pairs to implement a unique half-cone geometry setup in order to decrease the overall acquisition time as well as maximize spatial resolution. The intrinsic spatial and energy resolutions of the gamma detectors are measured to be 1.75 mm and 17.9 % respectively. Novel type of pinhole collimators was introduced. Square shape aperture with pyramid shape acceptance volume collimator was characterized both theoretically and experimentally. This type of a collimator allows for about 23 % of efficiency increase without significant reduction in spatial resolution. The x-ray CT subsystem combines various interchangeable microfocus x-ray sources with either a high resolution CCD based detector or a flat panel Hamamatsu C7940 CMOS array. The CCD detector employs a 7k by 4k Phillips CCD chip with dimensions of 5 cm x 9 cm, large enough to require no minification between the gadolinium oxysulfate phosphor and the chip. The both subsystems have been installed and successfully used in phantom imaging and in a variety of small animal studies. Spatial resolutions of 50 μm for CT and 0.9 mm for SPECT have been achieved for live animal imaging. The scanner is able to obtain a lower resolution CT set in 4.5 minutes and SPECT data set in 30 minutes.

Contents

List of figures and tables

Figures

Tables

CHAPTER 1
Introduction

Medical imaging is one of the most important and widely used techniques for detection and diagnosis of disease. The history of medical imaging can be dated back to the early 1900s. Around that time, radiology established itself as a medical sub-specialty, utilizing Roentgen's discovery of x-rays as a novel non-invasive diagnostic tool. The development of radiology grew steadily until World War II. Extensive use of x-ray imaging during the Second World War, the advent of the digital computer, and new imaging modalities have combined to create an explosion of diagnostic imaging techniques. Starting in the late 1940s, at least one new imaging modality has made its way into clinical diagnostic centers every ten years. Nuclear Medicine, Ultrasound imaging, X-ray Computed Tomography, and Magnetic Resonance Imaging have now become common in everyday clinical medical practice. Recently, those same tools have been widely employed in a variety of pre-clinical research settings. Recent advances in genetic engineering have significantly improved our understanding of the genotype, the genetic makeup of any living creature. Scientists are now able to determine and manipulate genetic structure, but phenotype characterization, the identification of the outward manifestation of a particular genotype, can be difficult to assess. Phenotype characterization and other particularly engineered gene sequence has not been thoroughly studied yet. Some of the needs of biomedical research can be satisfied with medical imaging.

Imaging modalities can be roughly divided into two groups according to depending on the sort of information that they provide. The first group, referred to here as structural modalities, includes X-ray Computed Tomography (CT), Magnetic Resonance Imaging (MRI) and Ultrasound (US). These modalities excel in conveying information about the internal structure of the imaged object. Skeletal structures, soft tissues (like muscles and fat), and lung tissue can be recognized from these images. What these structural imaging technologies lack is the ability to provide functional information, namely information about biological processes going on inside the living organism. These needs are addressed by the second group imaging modalities, referred to as functional modalities, which includes Single Photo Emission Computed Tomography (SPECT), Positron Emission Tomography (PET) and optical imaging. Those three have established firm ground in the biomedical research field, the first two in clinical and all three in pre-clinical (animal) imaging. Despite their differences, these three functional imaging modalities have similarities in that they all rely on detection of electromagnetic radiation originating from within the subject. Radiation emitting substances are introduced into the study subject from the outside, usually by intravenous injection. These substances, called radio- or optical tracers, are designed to interact with biologically active materials, like cells, proteins, antibodies and such. After the introduction of the tracer into the living body, external detectors are used to detect the emitted radiation in order to provide an overview of the location and intensity of the target biological processes.

Nowadays, both groups are treated not as rivals, but rather as complimentary components useful for obtaining a more complete description of biological processes. With this in mind, the two types of technologies are being actively merged, giving rise to

multimodality imaging devices such as CT/SPECT, CT/PET, and PET/MRI. The work presented here focuses on the development of a dedicated dual modality CT/SPECT scanner for small animal imaging, so we will explore the concepts of CT, SPECT and small animal imaging in more detail.

1.1 X-ray Computed Tomography (CT)

In some imaging modalities, the 3-dimensional internal structure of an unknown object can be mathematically reconstructed from a series of 2-dimensional projection images. This is the basic idea of Computed Tomography (CT). In the case of x-ray CT, the projections are acquired by irradiating the subject with x-rays and measuring the transmitted x-ray distribution. X-ray Computed Tomography (CT) was invented independently by British engineer Sir Godfrey Hounsfield [1] at EMI Laboratories, England, and Dr. Alan Cormack at Tufts University, MA, USA. The first X-ray CT prototype was built in 1974. For their work, Hounsfield and Cormack were jointly awarded the Nobel Prize in 1979.

As shown in Fig.1.1, an x-ray CT system consists of three major components: an X-ray source, a detector array, and a rotating gantry. Both the source and detector are mounted on a gantry, and they move around the object while acquiring projection images in quick succession.

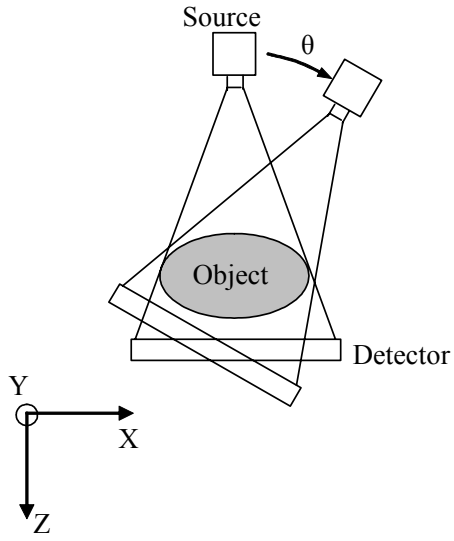

Fig.1.1. *X-ray CT imaging system*

In the following sections we will discuss the major components of a typical medical CT scanner.

1.1.1 X-ray production

X-rays belong to the family of electromagnetic radiation. The wavelength of x-rays ranges from a few picometers to a few nanometers. Typical energies of x-rays suitable for diagnostic use are from 10 to 150 keV.

X-ray photons are produced when high-speed electrons bombard a target material. The interaction between electrons and the target takes the form of several kinds of collisions. The majority of these collisions involve energy transfer that leads to heat dissipation. In fact, well over 99% of the electron's kinetic energy is dissipated as heat.

Two types of interactions lead to the production of x-ray photons. First, high-speed electrons traveling in the vicinity of positive nuclei experience sudden deceleration because of the Coulomb force between opposite charges. This deceleration produces

bremsstrahlung or braking radiation, emitted with a continuous photon energy distribution. It is also possible to produce bremsstrahlung radiation from the collision of an electron with a nucleus. The entire energy of the electron appears as bremsstrahlung in this case. This also defines the upper limit of the possible x-ray photon energies, and the overall probability of such a process is low.

A second type of radiation is emitted when a high-speed electron collides with and liberates an inner-shell electron of the target atom, leaving a hole in the atomic shell. Characteristic radiation results when an electron from an outer shell fills the hole. The energy of the emitted radiation is the difference between the binding energies of the two shells. A sample spectrum generated by 35 keV electrons incident on a molybdenum target is shown in Fig.1.2.

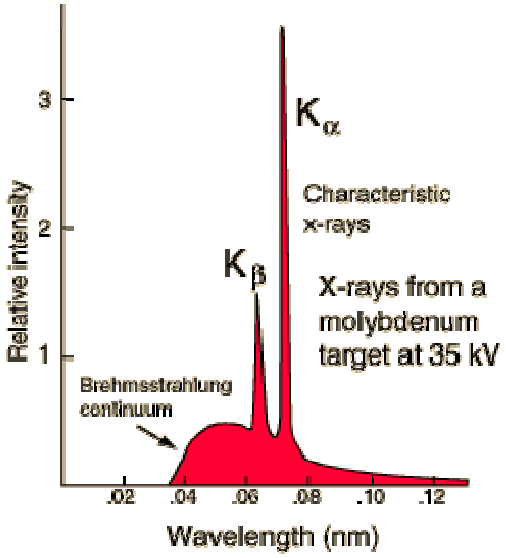

Fig.1.2. *Sample x-ray emission spectrum*

1.1.2 X-ray interaction with matter

The linear attenuation coefficient of a material depends on the photon energy and the elemental composition of the material. In the diagnostic range of x-ray energies, three mechanisms of x-ray interaction with matter dominate attenuation [2].

The first is coherent (or Rayleigh) scattering. The incident radiation excites electrons that in turn produce radiation at the same wavelength. Coherent scattering is material dependent and its cross section varies with the fourth power of the material's atomic number. Since high atomic number materials are not found abundantly in abundance in biologic tissue, this effect is not very strong in the CT diagnostic range and leads only to a slight broadening of the x-ray beam.

The second mechanism of x-ray absorption is the photoelectric effect, which dominates at lower energies. Here, the x-ray photon is absorbed by interacting with and releasing a tightly bound electron. An outer shell electron quickly fills the hole left by the ejected electron and emits characteristic radiation in the process.

The final important mechanism for tissue attenuation is Compton scattering, where an x-ray photon collides with a free or loosely-bound electron in an outer shell. The x-ray photon is deflected through some angle and suffers a partial loss of its energy. The scattered photon may still possess energy within the diagnostic range, and may exit the imaged object and be recorded by the detector. Scattered photons do not follow their original trajectory, and therefore are detrimental to image quality.

1.1.3 X-ray generating equipment

X-ray radiation suitable for diagnostic imaging is most commonly produced by electronic vacuum devices called the x-ray tubes. The basic components of the x-ray tube are the cathode and the anode. A sealed glass or metal enclosure houses the tube electronics in vacuum. Thermionic emission boils electrons off the cathode when electric current is passed through it. The electrons are accelerated across the tube by a high potential difference between the cathode and anode, and collide at high speeds with the target area of the anode. This collision produces x-rays as discussed earlier.

The x-ray production is a very inefficient process as most of the energy is lost to heat. The balance between heat build up and heat dissipation in the target material places an upper limit on the achievable tube output. In theory, high power density x-ray generators are able to achieve target material temperatures of the order of 2000°C, which is beyond the melting point of most materials used as targets. Rotating anode tubes permit the energy to be deposited over a larger target area, thereby permitting higher radiation output compared to stationary target tubes.

Fig.1.3 is a general schematic of a stationary target x-ray tube.

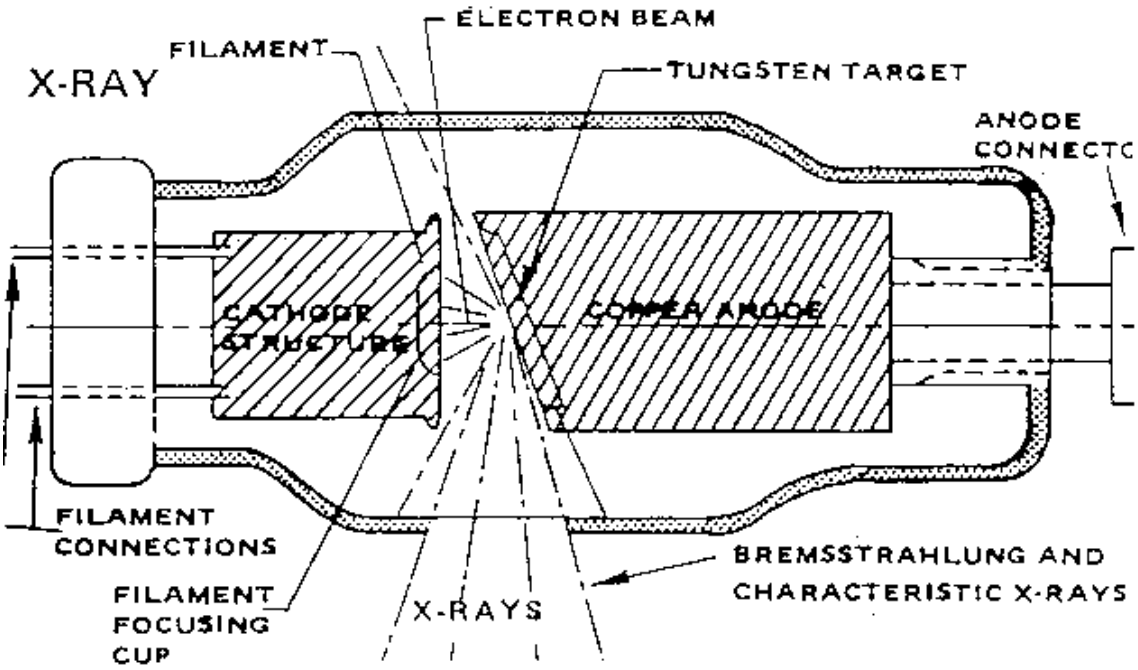

Fig.1.3. *Schematic of an x-ray tube*

The output flux of x-rays is confined to a limited solid angle by the tube housing. In diagnostic imaging, the output x-ray beam is filtered to remove lower energy photons, since the majority of the lower energy particles are absorbed by an imaged object. Those particles therefore do not contribute to the image, but do contribute to the absorbed radiation dose.

1.1.4 Image formation and x-ray detectors

The intensity of an x-ray beam passing through an object changes according to Beer's law:

$$I = I_0 e^{-\int_L \mu(\bar{x})dl} \tag{1.1}$$

where I_0 is the incident intensity of the beam, I is an attenuated intensity, $\mu(l)$ is the position-dependent linear attenuation coefficient of an imaged object and L is the length of the path of an x-ray beam. The point-to-point detected spatial variations in the transmitted intensity on the detector surface constitute the image. In other words, an x-ray image is a projected attenuation map of the imaged object. In order to obtain such a map, an x-ray beam intensity distribution needs to be measured.

Many x-ray detection methods have been developed since the beginning of x-ray imaging. The earliest one utilized photographic plates, consisting of an inert substrate coated with a radiation sensitive emulsion. The photo-emulsion is comprised of small size crystals of silver halide salt, suspended in gelatin. When exposed to radiation, some electrons are knocked out from the halide anions and then recombine with silver ions to form small specks of metal silver. The specks constitute a latent or invisible image, which can be turned into a permanent image by chemical development. Advances in the photographic industry, photo-plates were replaced with photographic film. This detection method, though more than 100 years old, is still dominant in radiographic diagnostics. Photo emulsions are not very sensitive to higher energy radiation such as x-rays, thus modern systems use a layer of phosphorescent material to absorb the x-rays and emit visible light that is efficiently detected by the film. The use of film as an x-ray image receptor is usually referred to as analog radiography. In this approach the film is both a detector and a display medium, thus it is impossible to change the displayed image contrast of an image once the film has been developed. This interconnection between acquisition and display is one of the limitations of analog radiography, and has in part

motivated the development of electronic detectors as alternates to film-based image receptors.

A step up from film radiography is the utilization of photo-stimulable phosphors (PSPs) as an x-ray detection medium. PSPs are typically sandwiched between a flexible plastic support and a thin protective layer of about 10 μm thick polyethylene terephthalate. PSPs are a special class of phosphors that trap a fraction of the incident x-ray energy in spatially localized regions within a 150-250 μm thick phosphoric layer. Rather than resulting in prompt emission of light, the deposited energy remains trapped for hours in the phosphor. This permits the energy absorption distribution in the phosphor to be determined (read out) at a later time, by exposing the phosphor to light or heat, resulting in de-excitation of the metastable energy traps and the release of light photons. Typically, the phosphor is read out by scanning it with a laser beam whose wavelength is different from that of phosphor's emission spectrum, allowing the emitted photons to be detected in the presence of the stimulation light. At each laser beam position, the emitted light is detected by a photo-multiplier tube (PMT) or charge coupled device (CCD) with the light intensity proportional to the x-ray energy deposited at that location. The information stored in the phosphor is read using a laser beam to scan the phosphor-coated plate in fine steps. Emitted light is detected by a photo-multiplier tube (PMT) at every scanning step, allowing an image to be formed from the digital values of the PMT readout. Unlike x-ray film, PSPs are reusable, since the stimulation light de-excites the PSP molecules to their original state. Following logarithmic transformation, the digital is stored in a computer for subsequent image processing and display. The digital image

formed by PSP readout electronics can be stored in a computer and manipulated by changing the contrast and brightness.

Progress in semiconductor technology has given rise to digital x-ray detectors in which the image is formed during the acquisition process, as opposed to during post-acquisition processing or readout as with film and PSPs. This type of detectors generates a position-dependent electric charge distribution to form the x-ray image. Detectors can be divided into two classes based on the method the charge is created. Direct-conversion detectors have an x-ray photoconductor, such as amorphous selenium, that directly converts x-ray photons into an electric charge. Indirect conversion detectors employ a two-stage procedure for x-ray detection. A scintillator is the primary material for x-ray interaction. When x-ray strikes the scintillator, the x-ray energy is converted into visible light, and that light is then converted into an electric charge by means of photo-detectors such as amorphous silicon photodiode arrays or charge-coupled devices (CCDs). In both direct- and indirect-conversion detectors, the electric charge pattern that remains after x-ray exposure is sensed by an electronic read-out mechanism and analog-to-digital conversion is performed to produce the digital image. A deeper look into semiconductor digital x-ray detectors will be taken in chapter 2.

1.1.5 Rotating gantry

Another important component of the CT scanner is the gantry. All scanner components, weighing hundreds of kilograms, are mounted on the gantry, which has to rotate at very high speed with extreme stability. The gantry must maintain angular and position accuracy, and must be free of significant vibrations that can cause artifacts.

Current technology, employed in commercial clinical scanners, enables collection of 1000 views in about 0.5 seconds.

1.1.6 Data acquisition and tomographic reconstruction

Tomographic imaging systems acquire a series of x-ray projections from a range of angles around the object. Each projection represents a value (or a collection of values in a multi-elemental x-ray detector) of the x-ray attenuation line integral through the object along the line from x-ray source to the x-ray detector element. Imaging the object at equiangular-spaced views over the scan angle equal to 180 degrees + the x-ray output cone angle forms a mathematically complete set of projection data. This fundamental condition was formulated in [3] and later complemented in [4] and [5]. Tomographic image reconstruction creates 2-D image (or 3-D volume) from the measured projection data. The measured projection along x-ray path L is given by the line integral in equation (1.1). Taking a logarithm of both sides of (1.1) and rewriting the equation in discrete form yields:

$$\ln(\frac{I}{I_0}) \equiv p_{ij\theta} = -\sum_{j \in L_i} \mu_j L_{ij} \tag{1.2}$$

where i is an index of an x-ray beam, j is an index of object element, L_i is the set of object elements through which x-ray beam i passes, L_{ij} is the intersection length of beam i with object element j, and μ_j is the attenuation coefficient for element j. If we let f(x,y) represent the 2-D image to be reconstructed, the line integral projection through f(x,y) defines a transformation in coordinate space. This kind of transformation was first introduced by Czech mathematician Johann Radon in 1917 and is known now as Radon

transform. The Radon transform of the target image is precisely what is measured when tomographic projection data is acquired. The collection of projections in the Radon transform domain is commonly referred to as a sinogram. The process of image reconstruction may be defined as converting projection data in the Radon transform domain to an image in the spatial domain. There are three major classes of algorithms that use fundamentally different approaches to accomplish this conversion: (1) Fourier-transform-based backprojection algorithms [6-9], (2) statistical algorithms [10-13] and (3) Radon-inversion algorithms [6-7]. Fourier-transform-based reconstruction techniques are most commonly used in CT and will be discussed in more detail in chapter 5.

1.1.7 Reconstructed image display

The visualization unit used for CT image display is called the Hounsfield unit (HU). It is also sometimes referred to as the CT number. The HU is defined as:

$$HU = \frac{\mu - \mu_{water}}{\mu_{water}} \times 1000 \tag{1.3}$$

where μ denotes a linear attenuation coefficient. Air, with $\mu \approx 0$, has a value of -1000 HU. Water is at 0 HU. Body tissues can have values ranging from a few HU to thousands. Because the range of values is so large, it is often necessary to modify the gray level scale to display only a small range of HU values that correspond to the tissue of interest. The CT display window is described by its window level and window width. The window width represents that range of HU that the gray scale displays, and the window level is the mid point of that range. A typical soft tissue display window may have a window

level of 20 HU and a window width of 100 HU. This means that the gray scale is displaying range of -30 to 70 HU.

1.2 Single photo-emission computed tomography (SPECT)

The concept of SPECT was first introduced in the 1960s [14] by Kuhl and Edwards, who developed the first tomographic nuclear medicine system known as emission computed tomography (ECT). SPECT is an emission tomography method used to determine the distribution of radioactivity within an imaged object [15]. The high-energy photons emitted from radioisotopes are called gamma rays. They travel through the object and are captured by a radiation detector called gamma camera. The spatial distribution of recorded counts forms a projection image. Generally, SPECT data acquisition is performed by rotating the gamma camera around the object while recording the gamma ray counts into a computer at all angles [16]. The radiolabeled tracers emitting gamma rays are usually injected into the subject and distributed within the subject proportional to the function to be measured. Several single photon emitting radiotracers have been employed in nuclear medicine diagnostic scans, with energies ranging from ~ 30 keV (Iodine-125) to 245 keV (Indium-111). For many years the most popular isotope for clinical use has been Tc-99m. This isotope is used in about 80% of roughly 100,000 nuclear medicine scans performed worldwide. Tc-99m emits 140 keV gamma rays and has a half life of ~ 6 hours.

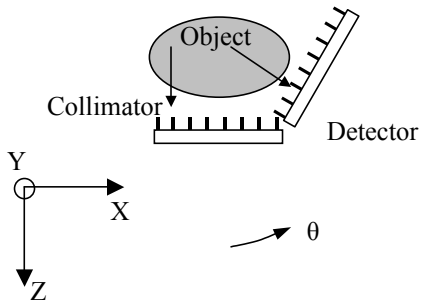

Fig.1.4 *Schematic of SPECT imaging system*

A general schematic of a SPECT setup is shown in Fig.1.4. The SPECT imaging system has three essential components: an imaging detector, an image-forming element and a rotating gantry. When equipped with a collimator, an imaging detector is usually referred to as a camera, so the following discussion will comply with this distinction.

Requirements for the gantry are similar to those of CT systems in terms of sturdiness and accuracy. But unlike CT nuclear medicine scans, SPECT scans employ significantly fewer projection images. Therefore, high-speed rotation is not a necessity for SPECT scanners. A quantitative assessment of a gantry performance will be given in chapter 4.

In the following section we will take a look at the existing technology of gamma ray imaging. An overview of detectors and collimators will be presented.

1.2.1 Gamma ray imaging detectors

The interaction of gamma rays with matter is not different from that of x-rays. Though different in origin, both rays are identical in their properties. Thus, detector technology used in x-ray imaging can be successfully applied to detect gamma radiation. The main difference in detectors comes from the amount of radiation that needs to be

detected. Due to a high flux of x-ray radiation, x-ray detectors are primarily of integrating type. That is, the detector integrates and digitizes total energy of the entire radiation flux incident onto the detector during data acquisition, as opposed to a photon counting detector, which detects individual particles and their energy. It wouldn't be right to assume that photon counters are used only in SPECT, while integrators are utilized only in CT. Both types of detectors were effectively employed in either modality, depending on the task requirement. An overview of gamma radiation imaging detectors can be viewed as an addition to the technology described above.

1.2.1.1 Scintillation detectors

Scintillation materials

Scintillation gamma detectors are the most common type of detection systems employed in medical imaging. These detectors are based on scintillators, materials that emit visible light in response to ionizing radiation. The interaction of ionizing radiation creates an inner shell vacancy and an excited primary electron. Subsequently, a cascade of excited electrons is generated by radiative decay, auger processes, and inelastic electron-electron scattering. However, much of the energy dissipates as thermal energy, and the efficiency for generating ionized electrons can be relatively low (15-50%). When the electron energies decrease below the ionization threshold, further nonradiative processes (thermalization, lattice relaxation, and charge trapping) can result, lowering the scintillation efficiency further. Processes resulting in the production of light can be divided into three categories. Self-trapped, excitonic, and recombination luminescence occurs due to unbound electrons and holes or bound e-h pairs (excitons), mostly

unperturbed motion in a perfect crystal structure. Examples of materials that exhibit this scintillation process are BaF_2 and pure NaI. Intrinsic ion activated luminescence is caused in some materials by an intrinsic ionic component undergoing a charge-transfer transition or an intra-ionic transition. Examples of such ions are Bi^{2+} in BGO ($Bi_4Ge_3O_{12}$) and WO_4^{2-} in $CdWO_4$. Dopant ion-activated luminescence has essentially the same scintillation mechanism as the one above, except for the material is intentionally doped with impurity ions to activate luminescence. Example materials with ion activators are $LaBr_3$:Ce and Lu_2SiO_5:Ce (LSO). More information on scintillation materials and their use in medical imaging can be found in [17].

Scintillators commonly used in SPECT include thallium doped NaI (NaI:Tl) and either thallium- or sodium-doped CsI. However, over the past several decades, there has been an intense search for brighter, faster, more reliable, and cost-effective alternatives [18-20].

Light detection

Several options for detecting output light exist today. Since their conception in 1940's, *photomultiplier tubes (PMTs)* have been a workhorse in the amplification of low intensity optical signals. PMTs provide large gain, on the order of 10^6 or more, and amplification noise is typically small. For scintillation cameras, the most important characteristics of PMTs are the spectral response and the quantum efficiency of the photocathode. Spectral response must be chosen to match the emission spectrum of the scintillator used. Photocathode quantum efficiency (QE) is critical in scintillation detectors because the spatial and energy resolutions are fundamentally limited by the Poisson statistics of the photoelectrons liberated at the photocathode. Typical QE values

of common bialkali (for example Sb-Rb-Cs or Sb-K-Cs) photocathodes are about 20% in the visible range. *Multi-anode or position-sensitive PMTs (MAPMTs or PSPMTS)* offer significant improvement in spatial localization of the detected light over their single anode relatives. Methods of position detection using PSPMTs will be discussed further in chapter 3. *Silicon photodiodes* are the products of highly-developed technology and have high quantum efficiency, so it would be natural to use them in scintillation cameras. But unlike PMTs, photodiodes do not have an internal gain mechanism; thus, the noise associated with the detector and the external electronics will have much more dramatic effect on detector performance. Silicon photodiode-based detectors are an example of a technology that performs well for detecting high flux x-rays, but has very limited abilities for reliable detection of single gamma rays. Some researchers were successful in using materials other than silicon for photodiodes in scintillation-counting applications [21]. Recent advances in *CCD* technology raised interest in creating CCD-based gamma detectors. If inherent noise problems are overcome, a very high spatial resolution detector can be constructed. *Avalanche photodiodes* (APDs) are recently developed light collection detectors. APDs are silicon diodes operated at a large reverse bias so that the charge cariers gain enough energy to excite new electron-hole pairs. Thus they function like PMTs, as photodetectors with internal gain. Because the gain can occur at any point in the semiconductor depletion region, rather than on discrete dynodes of the PMTs, the gain noise tends to be larger in APDs. The up side of APDs is that their bias voltage is much lower than that of PMTs and they are not susceptible to magnetic fields. This feature enables the use of APD-based detectors inside the MRI scanners to create dual modality MRI/PET devices [22].

1.2.1.2 Semiconductor detectors

Unlike scintillation devices, semiconductor detectors employ direct sensing of charge produce by ionizing radiation. When a voltage bias is applied to the semiconductor detector, it creates an electric field in the interior of the semiconductor material. The field distribution depends on the nature of the electrode contacts and the bias voltage. If blocking (diode-like) electrodes are used, and the bias is high enough, then any free charge carriers that might arise from thermal excitation are swept out and the device is said to be fully depleted. If the transverse direction of the crystal is large compared to its thickness and the material is homogeneous, then the electric field in the device is uniform, just as it would be in a dielectric-filled parallel-plane capacitor. The electrons in this uniform field move toward the anode, while the positively charged holes move toward cathode creating an electric current on the readout electrodes. Various semiconductor materials can be used in such solid-state devices. Silicon-strip detectors, devices based on Ge and CdTe crystals and most recently CdZnTe (CZT) have been widely accepted by the medical imaging community. Although this technology constitutes the biggest rival to well-established scintillation detectors (often outperforming them), semiconductor detectors can not be reliably manufactured in large quantities at this time. However, CZT-based detectors should have a bright future ahead of them once crystal growth technology matures.

1.2.1.3 Other potential detectors detector technologies

Proportional counters

In a gas, constant-gain ion multiplication can be achieved within a range of electric field strengths denoted by proportionality regions [23]. Ion multiplication results from the large mean free path of the electrons. Above critical field strength, the free electrons gain enough energy to ionize additional gas molecules before they collide. The heavier ions have a larger interaction cross section and do not gain enough energy between collisions to ionize other molecules. Proportional counters are useful in detection and spectroscopy of low-energy radiation (2-60 keV). However, energy resolution can be very sensitive to nonuniformities of the ionization chamber and of the anode wire. In addition, instabilities in the gas can result in spurious pulses.

Gas-electron multiplication (GEM) devices

Building on the concept of gas-ionizing detectors, a number of research groups have developed alternative methods to generate position- and energy-sensitive devices capable of single-photon detection and imaging. One of the more recent of these gas-ionizing detectors is the GEM. A GEM detector consists of metal-insulator-metal foil with an array of double conical, hourglass holes drilled through the foil. The foil is suspended in a gas filled chamber between two electrodes with an applied potential, divided across the electrodes and the GEM metal layers. Ionized electrons accelerate and converge on the holes, where the electric field intensifies, causing charge multiplication. The amplified charge pulse then passes out of the foil, where it transfers to either another GEM layer or to collection electrodes. Most ions generated in the avalanche region drift

along field lines away from the holes, mitigating the charge buildup on the insulating layer. GEM detectors can achieve relatively high spatial resolution (of the order of 200 μm), but as in the case of any gas detectors, the sensitivity to noncharged radiation is small.

1.2.2 Image forming elements – gamma collimators

Unlike x-rays, which are confined by a target material and tube housing, gamma radiation is emitted isotropically. This fact necessitates use of image forming elements, which would collimate incoming radiation. Several types of collimating techniques have been adopted. Here we will review several possible options.

1.2.2.1 Parallel-hole collimators

The most common type of collimator used in clinical gamma cameras is the so-called parallel-hole or parallel-bore collimator. It is constructed out lead or some other highly attenuating material and is essentially a slab of material with a large number of closely spaced holes. This type of collimator allows only gamma rays that are normally incident to the detector surface to pass through to the detector and contribute to the image. The field of view of a camera equipped with a parallel-hole collimator is limited only by a detector active surface and is irrespective of location of radioactive source. Parallel-hole collimator efficiency, as defined by a ratio between number of gamma rays passing through the collimator and total number of emitted gamma rays, is also independent of the source position. Efficiency is defined by internal collimator parameters, such as attenuation coefficient of the material, the height and shape of the

holes, and the distance between them. The typical efficiency for a parallel-hole collimator is ~ 10^{-4}. The spatial resolution of the parallel-hole collimator is dependent on the location of the source and degrades with increasing distance between the source and the camera.

1.2.2.2 Pinhole collimators

Another option for gamma ray collimation is the pinhole collimator. This concept of collimation has been extensively used in photography since it allows changing the size of the image depending on the relative locations of the object and the detector. Of course, photographic pinholes have to be adapted to gamma ray energies, but the concept stays the same. Pinhole collimators for gamma imaging are made out of highly attenuating materials like lead, tungsten, gold, and uranium. Internal parameters of the pinhole collimator are: the size of pinhole aperture, the opening angle of the pinhole, and the attenuation coefficient of the pinhole material. Two types of pinhole collimators are distinguished: a knife-edge collimator and a channel or keel-edge collimator. Differences between two types can be seen in Fig.1.5.

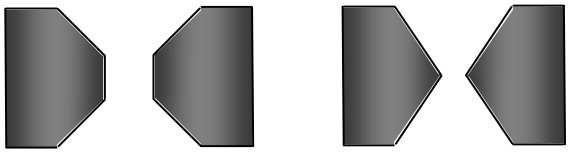

(a) (b)

Fig.1.5. *Cross section of channel (a) and knife-edge (b) type pinhole collimator*

Efficiency and spatial resolution of pinhole collimators depend on the intrinsic properties of the collimator as well as the relative positions of the source and the detector.

The efficiency of a pinhole collimator is usually less than that of a parallel-hole one, but the resolution is higher due to possible magnification of the image. Pinhole imaging will be explored in greater detail in chapter 3.

1.2.2.3 Multiple pinhole collimators

A way of increasing pinhole collimator efficiency while preserving spatial resolution is to use multiple collimating apertures. Efficiency of the gamma camera scales linearly with increase of number of pinholes. However, as the number of pinholes increases, overlapping, or multiplexing, of the pinholes images will occur. In this case, the system performance is no longer simply related to the collection efficiency. While it is true that total number of collected gamma events scales with the number of pinholes used, each photon conveys less information about its original location because of the uncertainty about which pinhole it came through. Several techniques of recovering missing information have been developed [24-26], all of them based on careful simulation of camera response.

1.2.2.4 Slit-slat collimators

An interesting approach to collimating is so called slit-slat collimator. It combines a slit in one direction with a set of perpendicularly oriented septa. This type of collimator provides magnification only in one direction -- the one perpendicular to the slit. Efficiency and resolution of this type of collimator are somewhere in between parallel and pinhole types of collimators. Several groups are working on incorporating slit-slat collimators in their scanners [27, 28].

1.3 Small animal imaging

In this section, motivation for small animal imaging will be presented. The main differences between human and small-animal scanning will be outlined. Specific tasks posed by small-animal imaging will be formulated. A short general overview of the current state of small-animal imaging technology will be offered. Finally, design goals for our scanner will be stated.

1.3.1 Importance of small animal imaging

Small animals are used widely in biomedical research. Mice in particular are preferred animal subjects: they are economical, reproduce rapidly, and can provide models of human diseases. Mice with compromised immune systems have been used for many years in studies of human tumor xenografts. The sequence of the mouse genome has been determined, and knockout mice (in which expression of a particular gene has been disabled) are available as models of various metabolic abnormalities.

Most studies in mice and other small animals are translational studies of human disease. Such studies are supported by government and private-sector research grants and by major pharmaceutical corporations. Other research studies are directed at cellular and subcellular processes that do not necessarily have immediate applications in human disease. Small animals are also used for some studies of animal diseases that do not have direct human analogues, but these studies are mostly confined to veterinary centers.

In all of these biomedical studies of small animals, imaging can play a key role. Imaging studies can determine whether a new drug reaches the intended target tissue or

organ and whether it also reaches other sites that may result in toxic effects. More detailed studies of biodistribution and pharmokinetics are possible, provided the spatial resolution and dynamic capabilities of the imaging system are adequate.

Imaging studies have significant advantages over postmortem tissue distribution studies. Although a few animals may need to be sacrificed to validate the imaging data, far fewer must be sacrificed than with conventional tissue biodistribution studies. Longitudinal experiments with the same animals are possible, and the effects of interventions such as drug treatment can be assessed.

1.3.2 Challenges of small animal imaging

An obvious challenge in small-animal imaging comes from the geometric size of the object. Roughly speaking, the field of view for small animals is ten times smaller than for humans, but the spatial resolution must be about ten times finer than for human imaging. Another distinction is that the object being imaged is typically much less scattering and absorbing in small-animal applications than clinically. The attenuation coefficients are the same in two cases, but the body dimensions are different. At 140 keV the attenuation of soft tissue is almost entirely due to Compton scattering, and the total attenuation coefficient is about 0.14 cm^{-1}. Thus, the attenuation length is about 7 cm, which is large compared to a mouse but small compared to a human. Clinical detectors can be adapted to animal studies, especially when it comes to SPECT, but their use is limited due to large size and high cost. Dedicated small-animal imagers need to be developed for both CT and SPECT. The typical requirement for spatial resolution in small-animal CT is of the order of 100 μm for a live animal scan and about 1 mm for small-animal SPECT. Both systems

are expected to minimize data acquisition time, since animals have to be immobilized to avoid degradation of images due to motion. This restriction leads to requirement of high efficiency for gamma cameras and fast frame rate acquisition for CT detectors. Interest in small animal research has significantly increased in the past decade, so a great variety of scientific and engineering approaches emerged to address the need for dedicated small animal imaging instrumentation.

1.3.4 Overview of small animal imaging scanners

Small animal CT

The history of high resolution x-ray computed tomography (micro CT) can be dated back to early 1980s. At that time the available X-ray detector elements were too large to provide the resolution required to image rodents, so some early investigators [29] replaced the detector block with a translating X-ray film cassette. The X-ray film was subsequently processed and digitized, providing data sets with sufficient resolution (~150 microns) to reconstruct useful images of small animal organs. By 1984 high-resolution X-ray detector technology had improved, and Burstein *et al.* [30] reported a ~50-μm resolution image of a mouse thorax obtained using a 90-kVp X-ray source and a 512-element linear array of X-ray detectors. During this period, conventional clinical CT systems were also employed to simultaneously image multiple mice [31] with low resolution (>800 μm) but very high throughput (eight mice at a time, 9.6 seconds per image). In 1987 Flannery *et al.* brought X-ray micro CT into a new era with the introduction of a three-dimensional imaging system using a two-dimensional detector consisting of a phosphor plate optically coupled to a charge-coupled detector (CCD)

array [32]. To acquire a large number of X-ray photons in each micro-pixel (~2.5 μm x 2.5 μm), these investigators employed a synchrotron X-ray source beam line in place of the conventional X-ray tube. During this time the Ford Motor Company Research Laboratories also developed a three-dimensional micro CT system for industrial applications using a laboratory X-ray tube for the source and an image intensifier screen coupled to a video readout. A fundamental contribution of the Ford group was the development of a new three-dimensional "cone-beam" image reconstruction algorithm, which remains one of the most widely used volumetric reconstruction algorithms [33].

In the 1990's a number of groups have developed micro CT systems for high-resolution specimen analysis [34-39]. Most of these systems employ CCD-based detector arrays, microfocus x-ray tubes, and have spatial resolution between 20 and 100 microns. It has to be noted that all of the early micro CT scanners utilized rotation of the object, rather than the source-detector scanner. This approach is justified for extracted specimen imaging, but delivers a great deal of uncertainty when imaging live animals. Shifts of internal organs due to gravity and animal rotation degrade image quality in high resolution scanners. This issue was addressed with the introduction of first dedicated small-animal micro CT system [40]. This scanner featured a CCD-based x-ray detector and a microfocus x-ray tube mounted on a rotating gantry, while the animal was rested on a stationary table. Reconstructed spatial resolution was estimated to be around 50 microns. The scanner received a name of Micro CAT I and it was the first commercially available dedicated small-animal microtomography system. Since its introduction in 2000, Micro CAT I underwent several upgrades and it is now marketed under Siemens Medical Inveon trademark. Rapidly growing interest in small animal research has

attracted commercial manufacturers of medical equipment to the field. Small-animal CT scanners are now offered by GE, Philips, Siemens, Toshiba and several other companies. Laboratory scanners are also being developed utilizing recent improvements in detector technology [41-45].

Small-animal SPECT

Small-animal SPECT, by analogy with microCT termed microSPECT, emerged as a separate field of SPECT technology in the late 1980s - early 1990s, when researchers started utilizing pinhole collimation on clinical gamma cameras [46-49]. As mentioned earlier, human scanners are bulky and expensive, therefore small-animal SPECT technology was progressing toward the construction of dedicated compact gamma cameras. Smaller sized cameras offer more flexibility in scanner geometry, so modular design of small-animal scanners has become predominant. Modular design allows for easy reconfiguration of a scanner to accomplish a specific task. For example, imaging of a mouse brain or heart does not require the whole animal to be in the field of view of a scanner. Instead, the camera or cameras need to be focused on particular areas of the rodent's body. Compact imagers are often installed on translation stages for radial position adjustment to optimize image acquisition geometry for a particular imaging application. Up until late 1990s microSPECT scanners were based on a rotating object approach. Even first ever commercial microSPECT scanner, released in 2002 by Gamma Medica IDEAS Corp under the name of A-SPECT, had an animal holder rotating in front of two 10 cm x 10 cm gamma cameras. Then, following in the footsteps of micro CT, researchers and commercial manufacturers migrated toward a rotating detector design [50-55]. The most recent trend is to avoid any rotation at all by utilizing rings of detectors

around the animal. Completion of one such scanner (U_SPECT) has been reported to date [56].

Combining two modalities on the same scanner is a natural next step in small animal imaging. A number of groups have entered the challenge of developing and implementing dual modality small animal scanner [57-60], including the Detector Development Group at UVa.

1.3.5 Design goals for UVa small-animal CT-SPECT scanner

The design objectives for the system are high spatial resolution, good signal-to-noise ratio, and acceptable acquisition times. Both modalities are planned to image a volume of view of ~ 4 cm x 4 cm x 6 cm to accommodate typically sized mice and small rats. The desired spatial resolution for the CT system is 100 microns, while the SPECT component is expected to achieve spatial resolution of 1 mm or less. Data acquisition time is limited to 1 hour. This is set by an empirical estimate of safe anesthesia time for a common mouse. SPECT subsystem is supposed to image animals injected with medium and low energy clinical isotopes, like I-125, Tc-99m and In-111.

References

[1] Hounsfield G.N., "*Computerized transverse axial scanning (tomography): 1. Description of system"*, British Journal of Radiology, vol.46, pp.1016–1022, 1973

[2] Jones E.J., Cunningham J.B. "*The physics of radiology"*, 4-th ed., Charles C. Thomas-Publisher, Springfield, IL, 1983

[3] Orlov S.S., "*Theory of three dimensional reconstruction. 1. conditions for complete data set"*, Sov. Phys. Crystallography, vol.20, no.3, pp.312–314, 1975

[4] Tuy H.K., "*An inversion formula for cone-beam reconstruction"*, SIAM J.Appl.Math., vol.43, no.3, pp. 546-552, 1983

[5] Smith B.D., *"Image reconstruction from cone-beam projections : necessary and sufficient conditions and reconstruction methods"*, IEEE Trans. Med. Imaging, vol.MI-4, pp.14-25, Jan 1985

[6] Kak A.C., Slaney, M., *"Principles of Computerized Tomographic Imaging",* New York, NY; IEEE Press, 1988

[7] Herman G.T., *"Image Reconstruction from Projections: The Fundamentals of Computerized Tomography",* New York, NY; Academic Press, 1980

[8] Shepp L.A, Logan B.F. ,*"The Fourier reconstruction of a head section",* IEEE Trans Nucl Sci., vol. 21, pp.21–43, 1974

[9] Ramachandran G., Lakshminarayanan A.,*"Three-dimensional reconstructions from radiographs and electron micrographs",* Proc Natl Acad Sci USA, vol. 68, pp.2236–2240, 1971

[10] Lange K., Carson R.E., *"EM Reconstruction algorithms for emission and transmission tomography",* J. Comput. Assist. Tomogr., vol. 8, pp.306–316, 1984

[11] Ollinger J.M., *"Maximum-likelihood reconstruction of transmission images in emission computed tomography via the EM algorithm",* IEEE Trans. Med. Imaging, vol. 13, pp. 89–101, 1994

[12] Lange K., Fessler J.A., *"Globally convergent algorithms for maximum a posteriori transmission tomography"*, IEEE Trans. Image Process., vol. 4, pp. 1430–1438, 1995

[13] Gleason S.S., Sari-Sarraf H., Paulus M.J., Johnson D.K., Norton S.J., Abidi M.A., "*Reconstruction of multi-energy X-ray computed tomography images of laboratory mice*", IEEE Trans. Nucl. Sci., vol. 46, pp. 1081–1086, 1999

[14] Kuhl D. E., Edwards R. Q. *"Image separation radioisotope scanning",* Radiol., vol. 80, pp.653–662, 1963

[15] Jaszczak R. J., Tsui B. M. W., "*Single photon emission computed tomography",* in Principles of Nuclear Medicine, H. N. Wagner and Z. Szabo Eds. Philadelphia, PA: Saunders, pp. 317–328, 1995

[16] Groch M. W., Erwin W. D., *"SPECT in the Year 2000: Basic Principles",* J. Nucl. Med. Tech., vol 28, pp. 233–244, 2000

[17] Kupinski M. A., Barrett H.H.,(Editors) *"Small animal SPECT imaging",* Springer science and media, 2005

[18] Derenzo S.E., Moses W.W., *"Experimental efforts and results in finding new heavy scintillators",* Heavy Scint. for Sci. and Indust. Apps, De Notaristefani, F., LeCoq, P.,Schneegans, M.eds., Gif-sur-Yvette, France, Editions Frontieres, pp. 125-135, 1993

[19] van Eijk C.W.E., *"Inorganic scintillators in medical imaging"*, Phys Med Biol, vol.47, pp. R85-106, 2002

[20] Weber M.J., "Inorganic scintillators: today and tomorrow", J. Lums, vol. 100, pp. 35-45, 2002

[21] Wang Y.J., Patt B.E., Iwanczyk J.S., Cherry S.R., *"High efficiency CsI(Tl)/HgI_2 gamma ray spectrometers*", IEEE Trans. Nucl. Sci., vol. 42, no. 4, pp. 601-605, 1995

[22] Schlyer D., Rooney W., Woody C., Vaska P., Kriplani A., Stoll, S., "*Development of a simultaneous PET/MRI scanner"*, IEEE Nucl. Sci. Symp. Conf. Rec., vol. 6, pp. 3419 – 3421, 16-22 Oct. 2004

[23] Knoll G.F., "*Radiation detection and measurement"*, 3rd ed., New York, Wiley, 1999

[24] Barrett H.H., Swindell W., "*Radiological Imaging: Theory of image formation, detection and processing"*, New york, Academic Press, 1996

[25] Meikle S.R. et.al., *"A prototype coded aperture detector for small animal SPECT"*, IEEE Trans. Nucl. Sci., vol. 49, pp. 2167-2171, 2003

[26] Schramm N. et.al., "Multi-pinhole SPECT for small-animal research", J. Nucl. Med., vol.43, no. 5, pp.S.913, 2002

[27] Metzler S. D., Accorsi R., Novak J. R., Ayan A.S., Jaszczak R. J., *"On-axis sensitivity and resolution of a slit-slat collimator "* **,** Journal of Nuclear Medicine, vol. 47, no. 11, pp.1884-1890

[28] Mahmood S.T., Hutton B.F., *"A prototype synthetic slit-slat collimator",* Nuclear Medicine Communications, vol. 28(3), pp.A16-A17, 2007

[29] Kujoory M.A., Hillman B.J., Barrett H.,*"High-resolution computed tomography of the normal rat nephrogram"*, Invest Radiol. 1980, vol.15, pp.148–154

[30] Burstein P.J., Bjorkholm R.C., Chase R.C., Seguin F.H., *"The largest and smallest X-ray computed tomography systems",* Nucl Instrum Methods Phys Res., vol.221, pp.207–212, 1984

[31] Miller G.G., Dawson D.T., Battista J.J., *"Compute tomographic assessment of radiation induced damage in the lungof normal and WR 2721 protected LAF1 mice"*,Int. Journ. Radiat. Oncol. Biol. Phys., vol.12, pp.1971-1975

[32] Flannery B.P., Deckman H.W., Roberge W.G., D'Amico K.L., "*Three-dimensional X-ray microtomography"*, Science, vol. 237, pp. 1439–1444, 1987

[33] Feldkamp L.A., Davis L.C., Kress J.W., "*Practical cone-beam algorithm",* J. Opt. Soc. Am., vol.1, pp. 612–619, 1984

[34] Holdsworth D.W., Drangova M., Schulenberg K., Fenster A., *"A table-top CT system for high-resolution volume imaging",* SPIE, vol.1231, pp. 239–245, 1990

[35] Holdsworth D.W., Drangova M., Fenster A., *"A high-resolution XRII-based quantitative volume CT scanner",* Med. Phys., vol.20, pp. 449–462, 1993

[36] Reid B.K., Cunningham I.A., *"High resolution X-ray imaging at soft diagnostic energies using a silicon photodiode array",* Med. Phys., vol. 20, pp. 1497–1504, 1993

[37] Hearshen D.O., Reimann D.A., Flynn M.J., "*Measurement of CT resolution in 3 dimensions*", Radiology, vol.17, pp.197-291, 1995

[38] Flynn M.J., Hames S.M., Reimann D.A., Wilderman S.J., "*Microfocus X-ray sources for 3-D microtomography*", Nucl. Instrum. Methods Phys. Res. Sect A., vol. 353, pp.312–315, 1994

[39] Elliott J.C., Anderson P., Davis G.R., Wong F.S.L., Dover S.D., "*Computed tomography: Part II. The practical use of a single source and detector*", JOM-J Min. Met. Mat. Soc., vol. 46, pp.11–19, 1994

[40] Paulus M.J., Sari-Sarraf H., Gleason S.S., Bobrek M., Hicks J.S., Johnson D.K., Behel J.K., Thompson L.H., Allen W.C., *"A new X-ray computed tomography system for laboratory mouse imaging*", IEEE Trans. Nucl. Sci., vol.46, pp. 558–564, 1999

[41] Cho M.H. et.al., "*A flat panel detector based micro CT system: performance evaluation for small-animal imaging*", Phys.Med.Biol., vol.43, pp. 4173-4185, 2003

[42] Krol A., Kieffer J.-C., Nees J.A., Liming Chen, Toth R., Bixhue Hou, Kincaid R.E., Coman I.L., Chamberlain C.C., Lipson E.D., Mourou G.A., *"Development of novel ultrafast-laser-based micro-CT system for small-animal imaging",* IEEE NSS Conf. Rec., vol. 3, pp. 1993 – 1996, 19-25 Oct. 2003

[43] Kim H.K. et. al., "Use of a flat-panel detector for microtomography: a feasibility study for small-animal imaging", IEEE Trans. Nucl. Sci., vol. 52, no. 1, part 1, pp. 193 – 198, 2005

[44] Badea C., Hedlund L.W., Johnson G.A., *"Micro-CT with respiratory and cardiac gating"*, Med.Phys., vol.31, no. 12, 2004

[45] Arai Y. et.al., *"Micro-computed tomography newly developed for in vivo small animal imaging"*, Oral Radiology, vol. 21, no.1, 2005

[46] Jaszczak R.J., Coleman R.E., "Single photon emission computed tomography (SPECT). Principles and instrumentation", Invest. Radiol., vol. 20, pp. 897–910, 1985

[47] Palmer J., Wollmer P., *"Pinhole emission computed tomography:method and experimental evaluation*", Phys. Med. Biol., vol.35, pp. 339–350, 1990

[48] Jaszczak R., Li J., Zalutski M., Coleman R., *"Pinhole collimation for ultra-high-resolution, small-field-of-view SPECT*", Phys. Med. Biol., vol. 39, pp. 425–437, 1994

[49] Weber DA, Ivanovic M, Franceschi D, et al. *"Pinhole SPECT: an approach to in vivo high resolution SPECT imaging in small laboratory animals",* J. Nucl. Med., vol. 35, pp. 342–348, 1994

[50] Kastis G.A., Wu M.C., Balzer S.J., et al. *"Tomographic small-animal imaging using a high-resolution semiconductor camera",* IEEE Trans. Nucl.Sci., vol. 49, pp.172–175, 2002

[51] Woon-Seng Choong, William W. Moses, Craig S. Tindall, and Paul N. Luke, *"Design for a high-resolution small-animal SPECT system using pixellated Si(Li) detectors for in vivo Iodine-125 imaging"* Lawrence Berkeley National Laboratory, Paper LBNL-54037, August 1, 2004

[52] Wu M.C., Hasegawa B.H., Dae M.W., *" Performance evaluation of a pinhole SPECT system for myocardial perfusion imaging of mice",* Med. Phys., vol.29, pp. 2830–2839, 2002

[53] Meikle S.R., et.al., "*Performance Evaluation of a Multipinhole Small Animal SPECT System*", IEEE NSS-MIC Conf. Rec., 2003

[54] Peterson T. E. et.al., *"SemiSPECT: A small-animal imaging system based on eight CdZnTe pixel detectors",* 2002 IEEE Nuclear Science Symposium and Medical Imaging Conference, Norfolk, VA, USA, Nov. 2002.

[55] L. R. Furenlid, D. W. Wilson, P. J. Pietraski, H. K. Kim, Y. Chen, H.H. Barrett, "*FASTSPECT II: A second-generation high-resolution dynamic SPECT imager*", 2002

IEEE Nuclear Science Symposium and Medical Imaging Conference, Norfolk, VA, USA, Nov. 2002.

[56] Beekman F., Vastenhouw B., *"Design and simulation of a high-resolution stationary SPECT system for small animals"*, Phys. Med. Biol., vol. 49, pp. 4579-4592

[57] Iwata K., Hwang A.B., Wu M.C., Tang H.R., Da Silva A.J., Wong K.H., Dae M.W., Hasegawa B.H., "Design and utility of a small animal CT/SPECT system", IEEE Nucl. Sci. Symp. Conf. Rec., vol.3, pp. 1849–1851, 2001

[58] M. B. Williams et. al., "Integrated CT-SPECT system for small animal imaging," *Proceedings SPIE vol. 4142-Penetrating Radiation Systems and Applications II*, F. P. Doty, H. B. Barber, H. Roehrig, and E. J. Morton eds., pp. 265-274, Dec. 2000

[59] A. G. Weisenberger, R. Wojcik, E. L. Bradley, P. Brewer, S. Majewski, J.Qian, A. Ranck, M. S. Saha, K. Smith, M. F. Smith, and R. E. Welsh, "*SPECT-CT system for small animal imaging*," Conference Record of the 2001 IEEE Nuclear Science Symposium and Medical Imaging Conference, San Diego, CA, USA, vol. 3, pp. 1840 - 1844, Oct. 2001

[60] Iwata K., MacDonald L. R., Li J., Williams S. P., Sakdinawat A. E., Hwang A. B., Wu M. C., Patt B. E., Iwanczyk J. S., and Hasegawa B. H., *"Dual isotope imaging with a dedicated small animal CT-SPECT system"* , Mol. Imag. Biol., vol. 4, no. 4(suppl. 1), pp. S21, 2002

CHAPTER 2
X-ray subsystem

The two major components of a small animal CT subsystem are an x-ray generating tube and a digital detector. Various options for each component exist today, but the unique challenges inherent in the task of small animal imaging impose strong restrictions, with the requirement for high spatial resolution being at the top of the priority list. Several research groups, including ours, have published studies on the performance of candidate imaging components for small animal CT [1]-[4]. As a result of those investigations we have incorporated two x-ray detectors and two x-ray sources in our scanner. All of the incorporated parts are described and characterized in this chapter.

2.1 Digital X-ray detectors

An overview of digital x-ray detector technology was given in the introduction. This subchapter will describe the detectors used in our scanner with deeper insights into their underlying technology.

2.1.1 CCD detectors

CCDs, or charge-coupled devices, are semiconductor solid state light sensors that were first introduced in 1970 by Bell Telephone Laboratories. Semiconductors are materials that have a band gap on the order of 1eV. What makes semiconductors useful as light detectors is that energy deposited by an absorbed photon can excite an electron into

the conduction band via the photoelectric effect. CCDs work by generating, collecting, transferring and detecting charge. Charge is generated by incoming photons with energy greater than the silicon's band gap energy (1.14eV). Excited valence electrons move across the band gap to the conduction band, creating electron-hole pairs. Photons with energies greater than 5 eV will produce multiple e-h pairs. After the charge is read out, the e-h pairs will recombine in approximately 100 μs.

The physics of CCDs is based on the principle of a metal oxide semiconductor (MOS) capacitor. Those capacitors are formed by placing a metal electrode, insulated by a film of silicon dioxide, onto a silicon substrate. Fig.2.1 shows a schematic representation of the MOS capacitor. A thin layer of metal attached to an electrode forms the gate. A bias voltage may be applied to the gate in order to change the shape of the underlying potential. Beneath the gate, a 0.1 μm-thick oxide layer (usually SiO_2) functions as the dielectric of the capacitor.

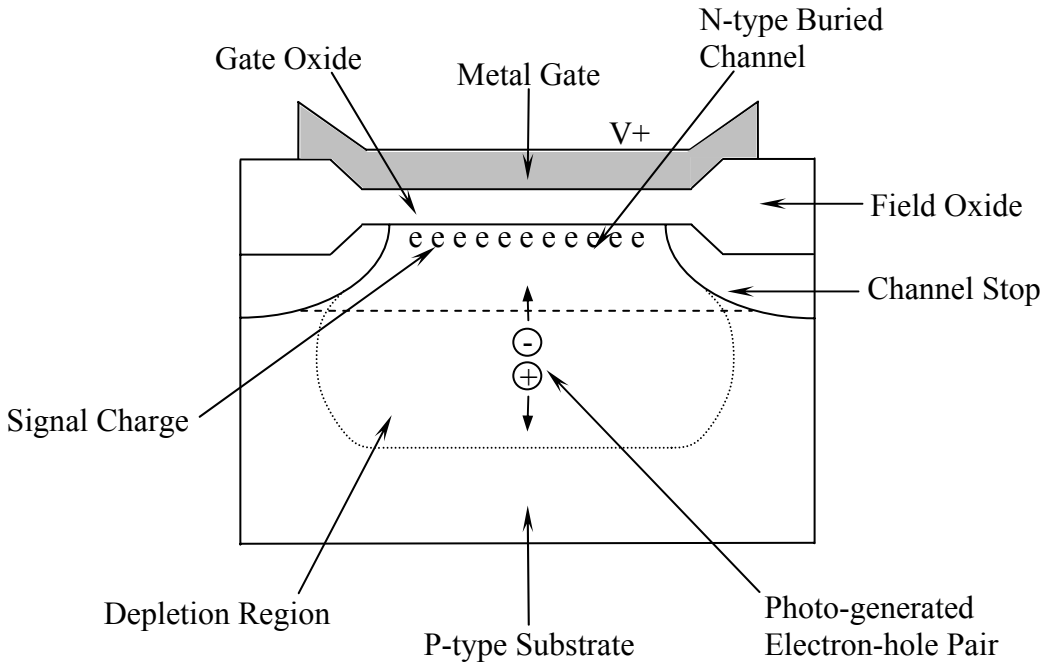

Fig.2.1. *Cross section of a MOS capacitor*

The oxide is thickened to ~ 0.5-1.5 μm above the channel stops to insulate the channel stops from changes in gate voltage. The purpose of the channel stops is charge confinement. They are made of heavily doped P-type materials with an extra oxide layer over the top. P-type semiconductors are materials doped with lower atomic number impurities such that positive "holes" are created in the valence states. Most modern CCDs have N-type buried channels which are created by adding an N-type layer (1-3 μm thick) between the gate and the oxide. The purpose of the N-type layer is to eliminate fast surface states, which cause problems with charge transfer, by moving the potential minimum away from the Si-SiO_2 interface. N-type semiconductors are materials with an excess of free electrons in the conduction band due to the presence of higher atomic number impurities. Surrounding the N-type region is the depletion region, where electrons from the N-type region can combine with holes from the P-type region. This

results in the formation of a potential field since the P-type region becomes positively charged while the N-type region becomes negatively charged. The P-type region surrounds the depletion region and is usually a substrate of at least 15 μm thick [5].

CCD arrays are formed by a series of closely spaced MOS plates on the surface of a semiconductor. Application of bias voltages to the MOS plates results in the creation of localized potential wells in the semiconductor under each plate. Charge packets can be confined in the potential wells and shifted along the surface under the influence of appropriate clocking waveforms applied to the gates. In CCDs with three phase architecture, for example, the charge created by the e-h pairs is confined and collected by three overlaying gates that induce a potential profile. Each pixel in a CCD consists of these three gates or electrodes see Fig.2.2. In CCDs with four-phase architecture (as in the case of our detector), the fourth electrode is used to control antiblooming. The antiblooming process prevents charge spill from the well onto neighboring pixels if the total charge collected in the well exceeds its storing capacity.

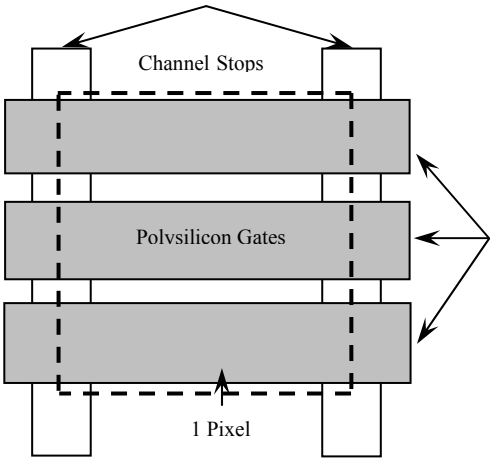

Fig.2.2. *Schematic of a single pixel of three-phase CCD*

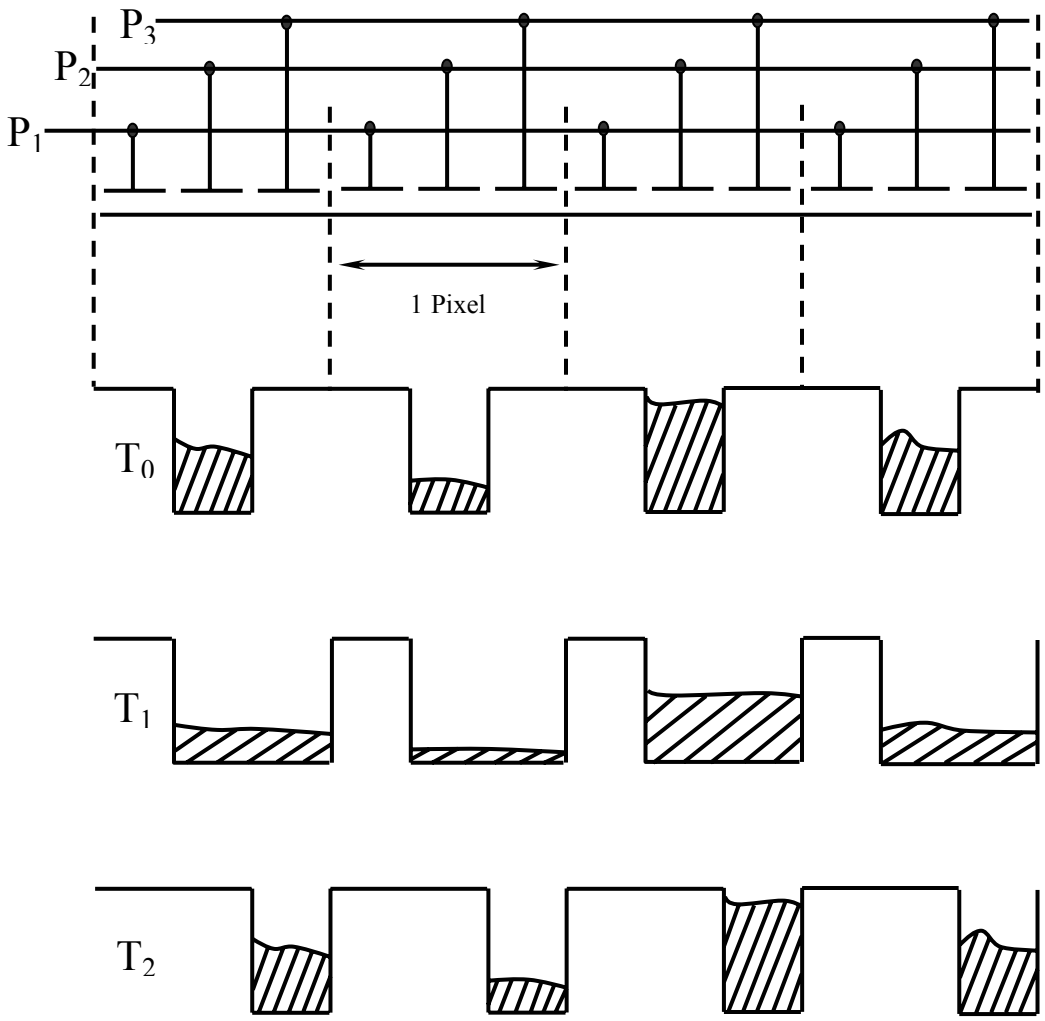

Fig.2.3. *Charge transfer in three-phase CCD*

Fig.2.3 shows the transfer of charge during the readout of each pixel by clocking the gate potentials in a coordinated fashion. Signal electrons move down the vertical registers (columns) to the horizontal registers (rows). The horizontal registers are then read out one at a time serially by an on-chip amplifier. Finally, the individual charge packets are converted to an output voltage and then digitized by an analog-to-digital converter (ADC).

Imaging detectors based on CCD technology have become ubiquitous during the past two decades. CCDs can be found in a range scientific applications (such as

astronomy, astrophysics, electron microscopy, crystallography and so on) as well as in general public-oriented digital photographic equipment. The main limitation of using CCDs in medical imaging applications is their size. Typical CCDs nowadays have an active area range from 2 cm by 2 cm to 5 cm by 5 cm, thus optical demagnification must typically be employed between the object or x-ray converter and the CCD for imaging of objects even as small as rodents. For a regular 25 g mouse an imaging area of about 5 cm by 10 cm is required. Different approaches to demagnification can be utilized, such as optical lenses or fiber optic tapers. But each option introduces light losses and image distortions and as a consequence reduces image quality. However, the recent availability of larger size scientific quality CCD chips allows a detector to be designed without the use of image demagnification components. The chip is manufactured by Philips Corp. It contains a 4k by 7k array of 12 μm by 12 μm pixels for a total imaging area of 49 mm by 86 mm.

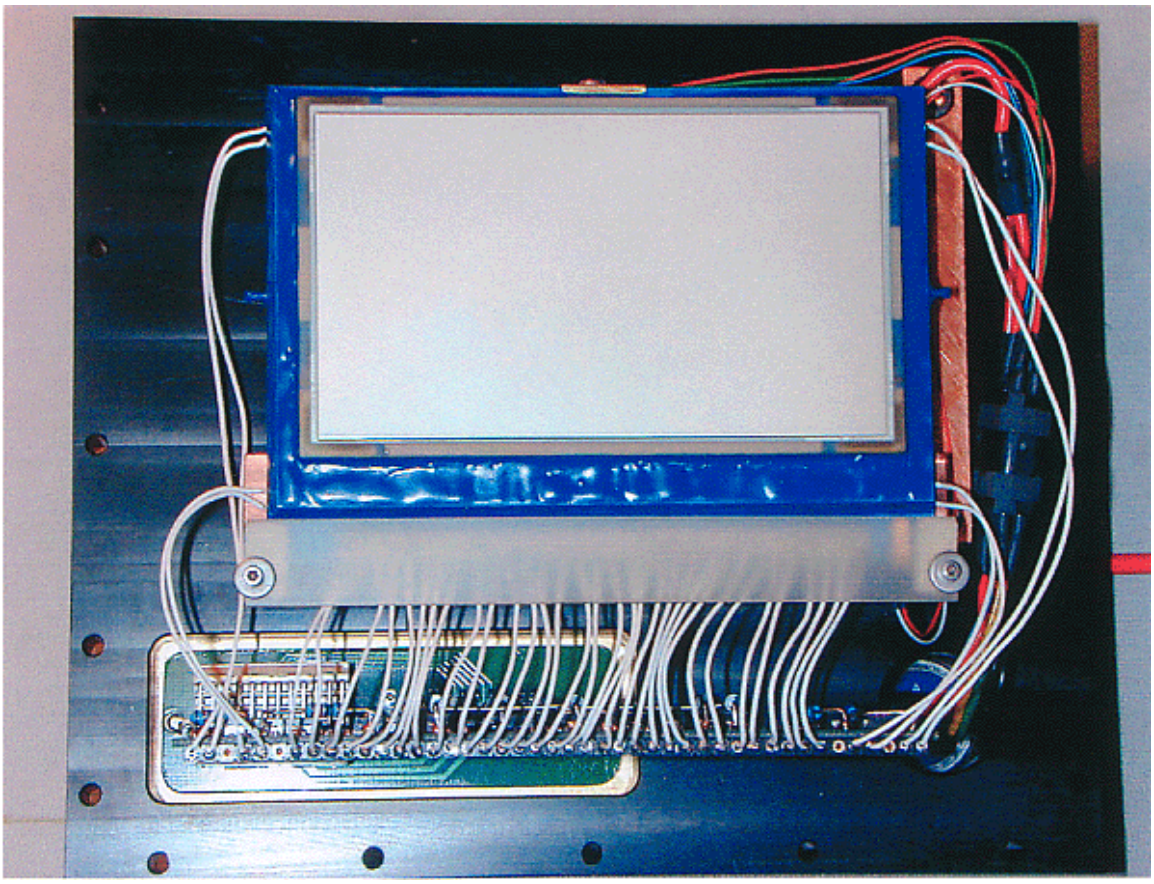

Fig.2.4. *CCD chip assembly*

A photograph of the Philips CCD chip is shown in Fig.2.4. This chip boasts 4 on-board read out amplifiers and, as mentioned above, is based on 4- electrode pixel architecture.

2.1.2 CCD detector design

Since the principle of CCD operation is based on photoelectric conversion, its quantum efficiency, the ability to convert incoming radiation into charge, depends strongly on radiation energy. For a CCD to work in an x-ray detector it should be coupled to a material that converts x-rays (typical energies 10-90 keV) into visible light (1-3 eV).

Popular converters presently are columnar-grown CsI doped with elements such as thallium or sodium, and rare earth phosphors such as terbium-doped gadolinium oxy-sulfide. Our detector, which is commonly referred to as the Big Chip (BC), utilizes a 45 μm thick Gd_2O_2S:Tb phosphor with a density of 18 mg/cm^2. This choice is a result of a thorough study, carried out by our collaborators from Brandeis University in cooperation with scientists from RMD (Radiation Monitoring Devices Inc, Watertown, MA) [6].

Fig.2.5 is a schematic of the Big Chip detector.

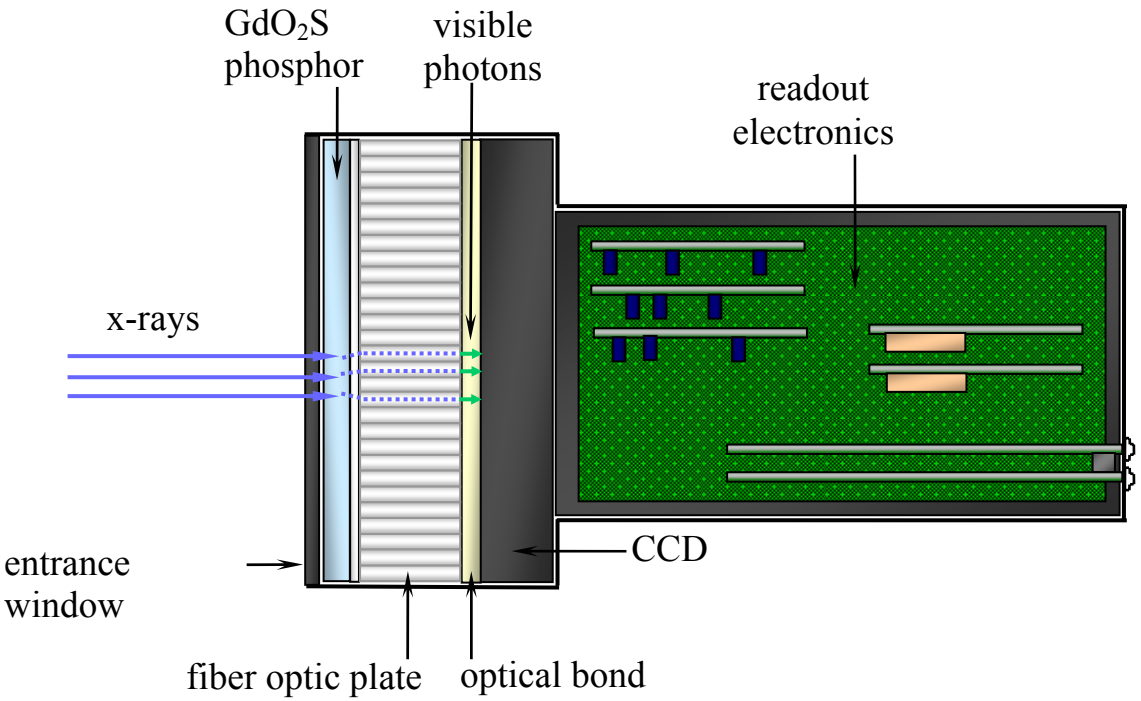

Fig.2.5. *Schematic of Big Chip detector*

The CCD chip is permanently bonded to a 1:1 ratio fiber optic plate. The conversion phosphor is coupled to the plate with an optical grease compound to ensure strong optical attachment. The CCD chip is affixed to an electronic printed board that contains the chip's power connections and communication lines. The CCD board is connected to the

main signal distribution board which holds a 1 MHz ADC board custom-made by Aviex Electronics (Naperville, IL) as well as input clocking lines and output data lines. The whole CCD-electronics assembly is enclosed in a two compartment aluminum casing, with the compartment for the CCD and its board being air-tight. A front view photograph of the Big Chip detector is shown in Fig.2.6

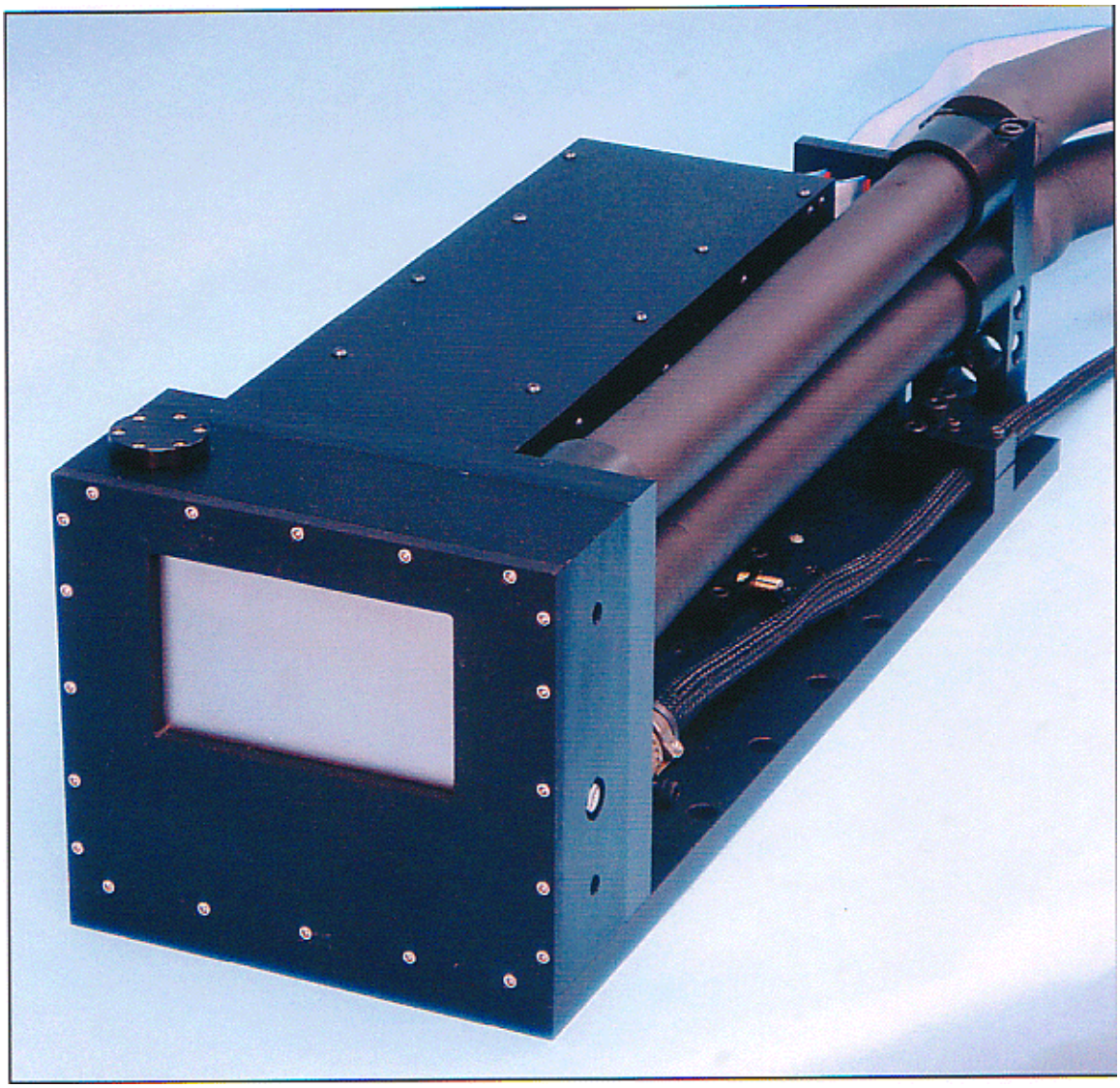

Fig.2.6. *Photograph of Big Chip detector*

Water cooling of the CCD (described below) is used to decrease detector thermal noise, and water condensation on the chip and its associated electronics is possible. To prevent moisture build-up on the CCD, a container with desiccant is suspended inside the CCD-holding compartment.

2.1.3 Thermoelectric cooling

Typical thermoelectric (TE) modules are manufactured using thin ceramic wafers with a series of positively (P) and negatively (N) doped bismuth-telluride semiconductor materials (pellets) sandwiched between them. They vary in size from approximately 0.5 cm by 0.5 cm to 5.0 cm by 5.0 cm. The ceramic material on both sides of the semiconductor adds rigidity and provides the necessary electrical insulation. The thermoelectric couples (pairs of P/N pellets) are connected electrically in series and thermally in parallel. They can function individually or stacked (multi-stage modules). A thermoelectric module can contain one to several hundred couples. As the electrons move from the P-type material to the N-type material through an electrical connector, the electrons jump to a higher energy state, absorbing thermal energy from the cold side. Continuing through the lattice of material, the electrons flow from the N-type material to the P-type material through an electrical connector, dropping to a lower energy state and releasing energy as heat to the heat sink (hot side). The charge carriers in the semiconductor material act in a manner similar to the compressed refrigerant in mechanical systems. Instead of a compressor, thermoelectric coolers use DC power.

When DC voltage is applied to the module, positive and negative charge carriers in the semiconductor material absorb heat energy on one substrate surface and release it on

the opposite surface. Fig. 2.7 illustrates the process. Peltier coolers are also power generators because they convert heat energy into electricity. When a temperature gradient exists across thermoelectric module, a voltage potential occurs at the terminals. This typical junction phenomenon is known as Peltier Effect, discovered in 1834, by which DC current applied across two dissimilar materials causes a temperature differential.

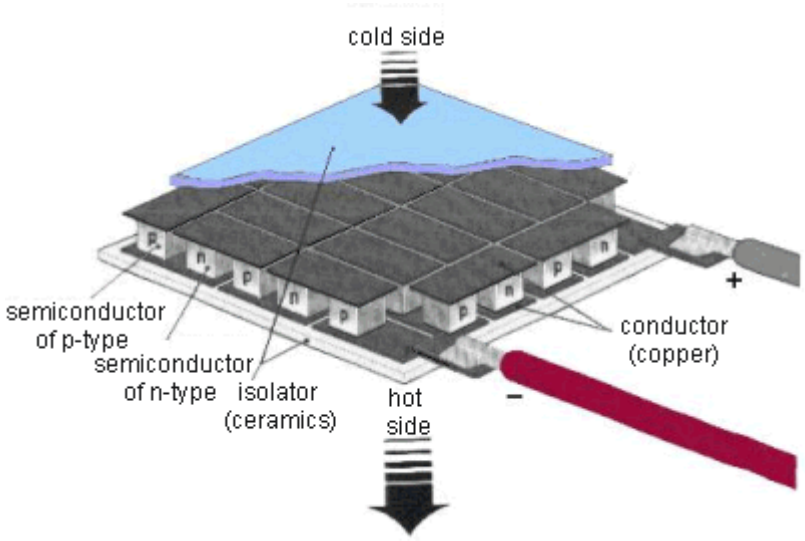

Fig.2.7. *Single stage thermoelectric module or Peltier cooler*

TE coolers offer several distinct advantages. They have no moving parts and, therefore, substantially reduced maintenance requirements. TE coolers contain no materials requiring periodic replenishing. Precise temperature control to within fractions of a degree can be maintained with appropriate circuitry. Finally, they function in environments that are too severe, too sensitive, or space too limited for conventional refrigeration.

To reduce noise caused by the thermally generated electrons, the BC detector's CCD chip is cooled by a single stage TE module (Melcor Corp, Trenton, NJ). The rate at which heat energy can be pumped by a thermoelectric cooler is influenced by many

factors, like ambient temperature, the physical and electrical characteristics of the module, and the efficiency of the heat dissipation system. Thermoelectric cooling applications involve heat loads ranging from several milliwatts to hundreds of Watts. In this particular application, the load for cooling a CCD to -10°C is approximately 15 Watts. A heat dissipation system is provided by means of a water-cooled manifold, which has chilled water running continuously through it. Water is chilled and pumped through the manifold by a Neslab model M25 water chiller (Thermo-Neslab, Newington, NH). Provisions were made to ensure that the internal plumbing of the cooling system does not leak or corrode thereby preventing CCD damage and failure.

The detector cooling system is controlled by a custom-written program implemented in Delphi. The program is installed on a dedicated computer. The program keeps track of several control parameters such as Peltier element temperature, water temperature and flow rate, heat load, power overload and uninterruptible power supply (UPS) state. In case a fault is detected in any of the controlled parameters, a controlled CCD warm-up sequence starts automatically without user confirmation. This is necessary to ensure that the CCD is warmed up at a steady slow rate (about 1°C/min) to prevent cracking of the bond between the CCD and fiber optic plate.

2.1.4 External electronic components

Fig.2.8 shows the input/output connectors on the back side of the detector for connection to external, rack-mounted electronic components. The layout of the rack can be seen in Fig.2.9. The rack contains two CPUs for temperature control and detector management, respectively, one single-channel and one dual-channel power supply for the

detector on-board electronics and cooling system, a power distribution and monitoring box and a UPS for the temperature control computer. The purpose of monitoring box is to receive feedback from the temperature sensors, located on the CCD block and chilling water connection, and reroute to the temperature controlling CPU for further analysis. The interconnection between components is shown on the diagram.

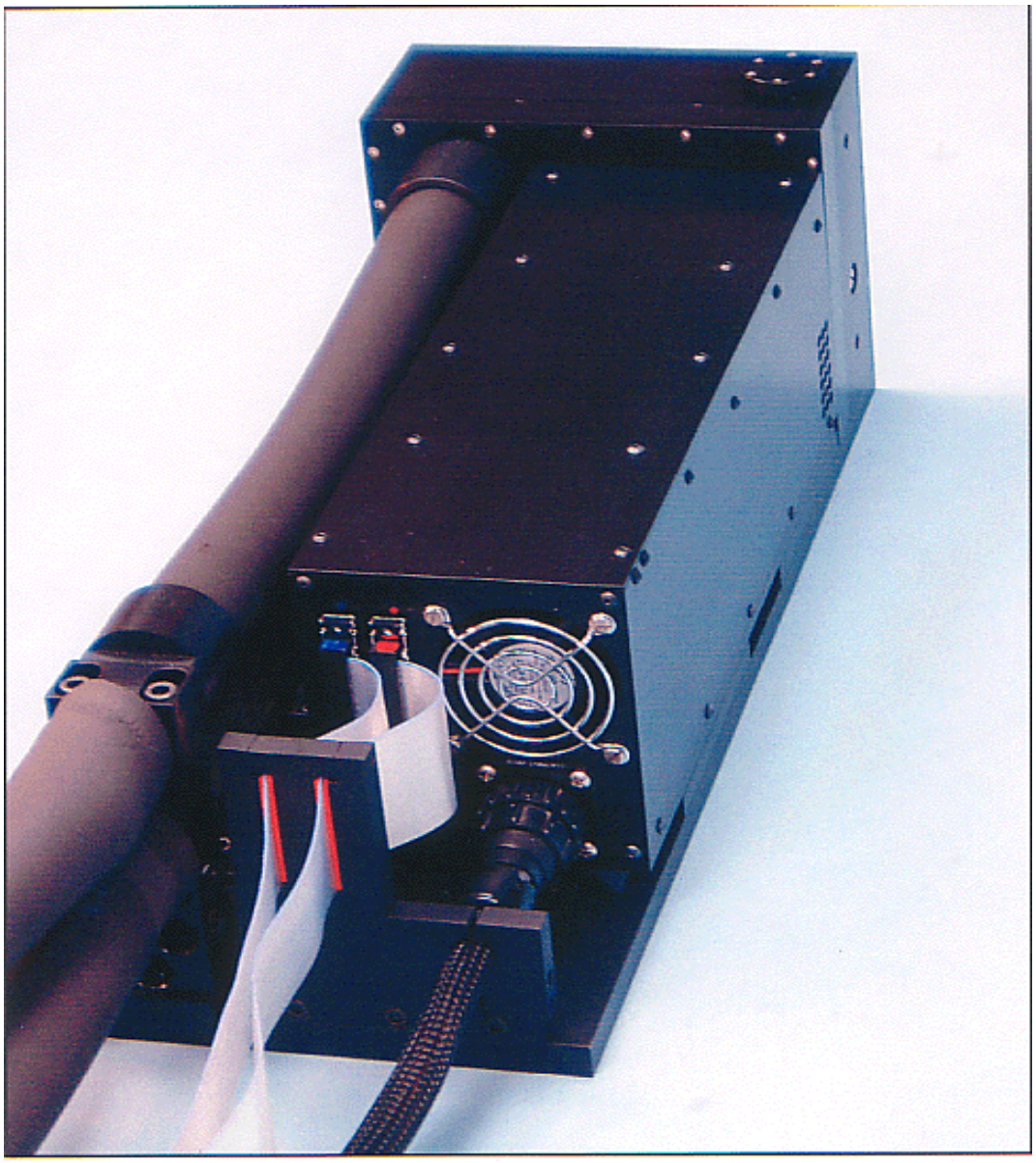

Fig.2.8. *Back view of the Big Chip detector*

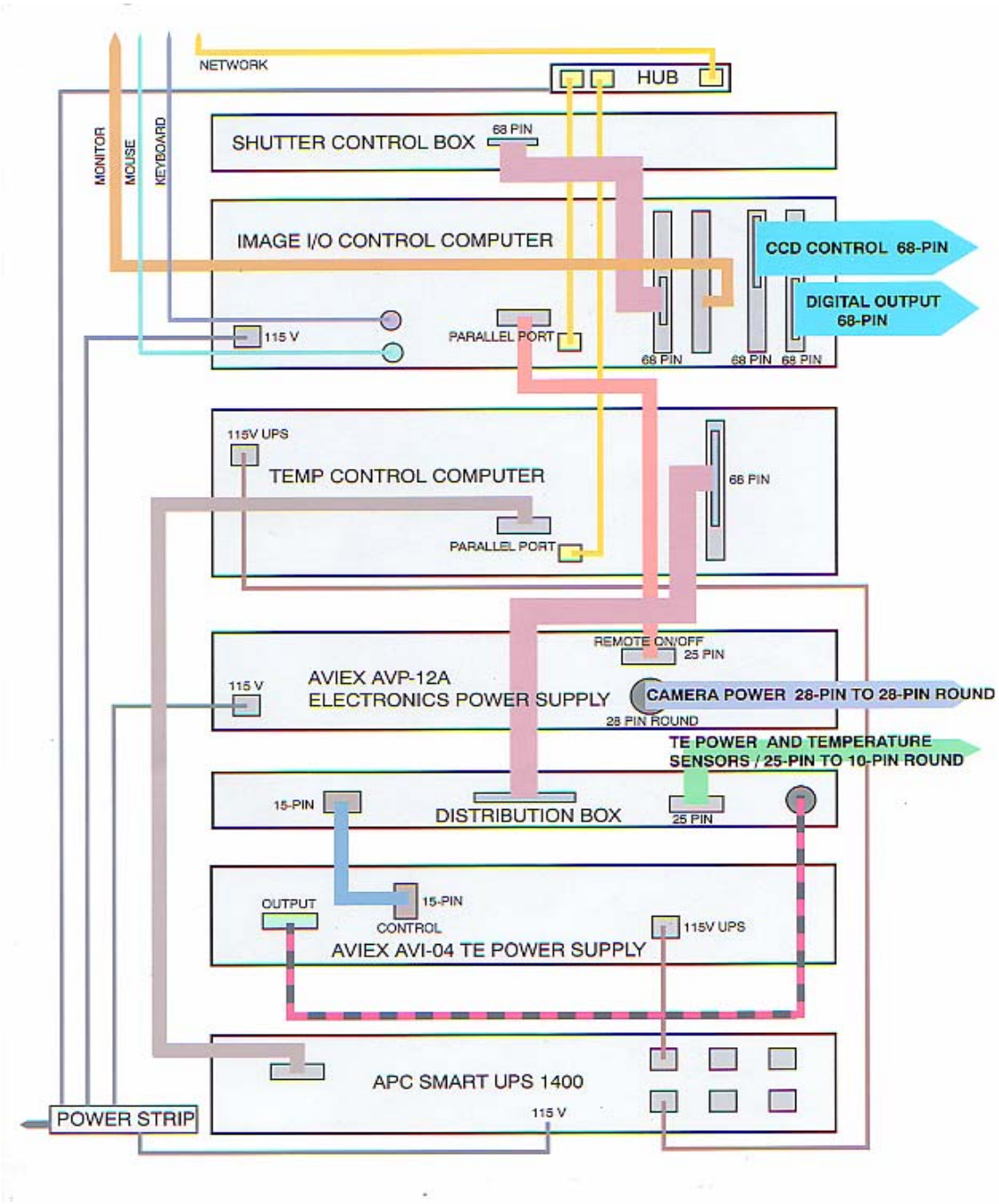

Fig.2.9. *Big Chip detector electronics layout*

The detector computer contains two National Instruments PCI-32DIO-HS digital I/O cards. Both cards are connected to the detector by 68-pin flexible ribbon cables. One of

the cards provides the CCD with clocking sequence pulses by switching on and off appropriate the digital channels whiles the other acts as a recipient of the digital signals from the ADC.

A custom-written interface program runs on the detector computer. This program is used for image acquisition and can be run directly from the detector computer or from a separate main scanner control computer via TCP/IP connection. Upon receipt of the digitized pixel data the program forms an image array, performs optional calibrations, displays the image and stores image files on local hard drive. Calibrations include dark correction and flat-fielding. Dark correction consists of the subtraction of a stored dark calibration image. The dark calibration image is obtained by taking three dark images (no x-ray input to the detector) for the same integration time as the one to be corrected and averaging those three images. The purpose of the dark correction is to remove spatially correlated thermally generated noise from the image.

Flat-fielding is a process of compensation for detector x-ray sensitivity non-uniformities. It is carried out according to the following formula:

$$I_{ij} = (I\_raw_{ij} \times \overline{F}) / F_{ij} \tag{2.1}$$

where I_raw_{ij} is the uncorrected image, F_{ij} is a stored flat field or food image, $\overline{F}$ is the average pixel value of the flood image, I_{ij} is the corrected image. The flood image is an image taken with an attenuator of uniform thickness such as a block of acrylic in between an x-ray source and a detector. Since our detector produces relatively large size images (~14 MB), an inverse of the flood image multiplied by the average is stored as a correction map. This is done in order to reduce the calculation time because

multiplication is about 50 times faster than division. A snapshot of the program interface is shown in Fig.2.10.

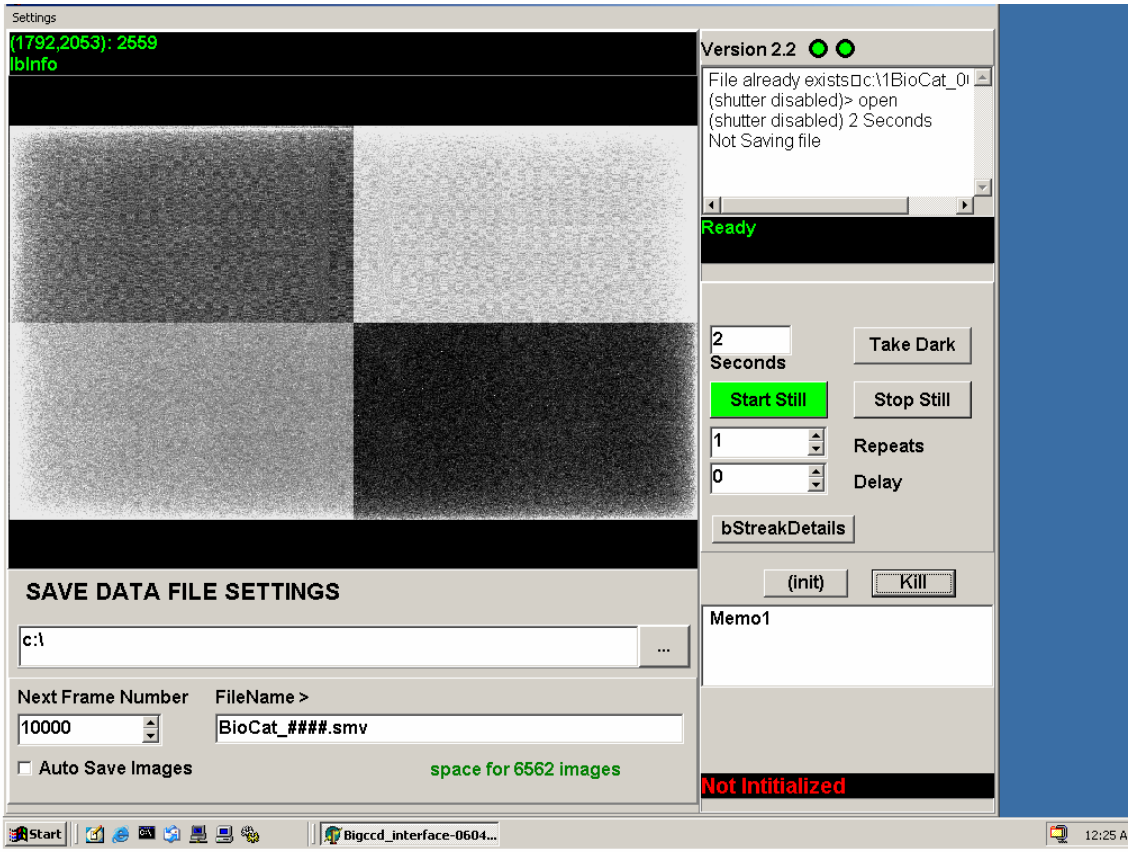

Fig.2.10. *Acquisition program interface*

2.1.5 CMOS flat-panel detectors

Complimentary metal-oxide-semiconductor (CMOS) imaging sensors were introduced in the late 1960s. Built on the same MOS technology as CCD, this type of sensor employs complementary p- or n-type MOSFET transistors to form logic gates. CMOS detectors are so called active pixel sensors (APS). Unlike a CCD pixel, which is in essence a capacitor, CMOS pixels include an amplifier. The standard CMOS APS

pixel, shown in Fig.2.11 consists of three transistors and a photo detector, usually a photodiode. More sophisticated designs can employ 4, 5 or 6 transistor configurations.

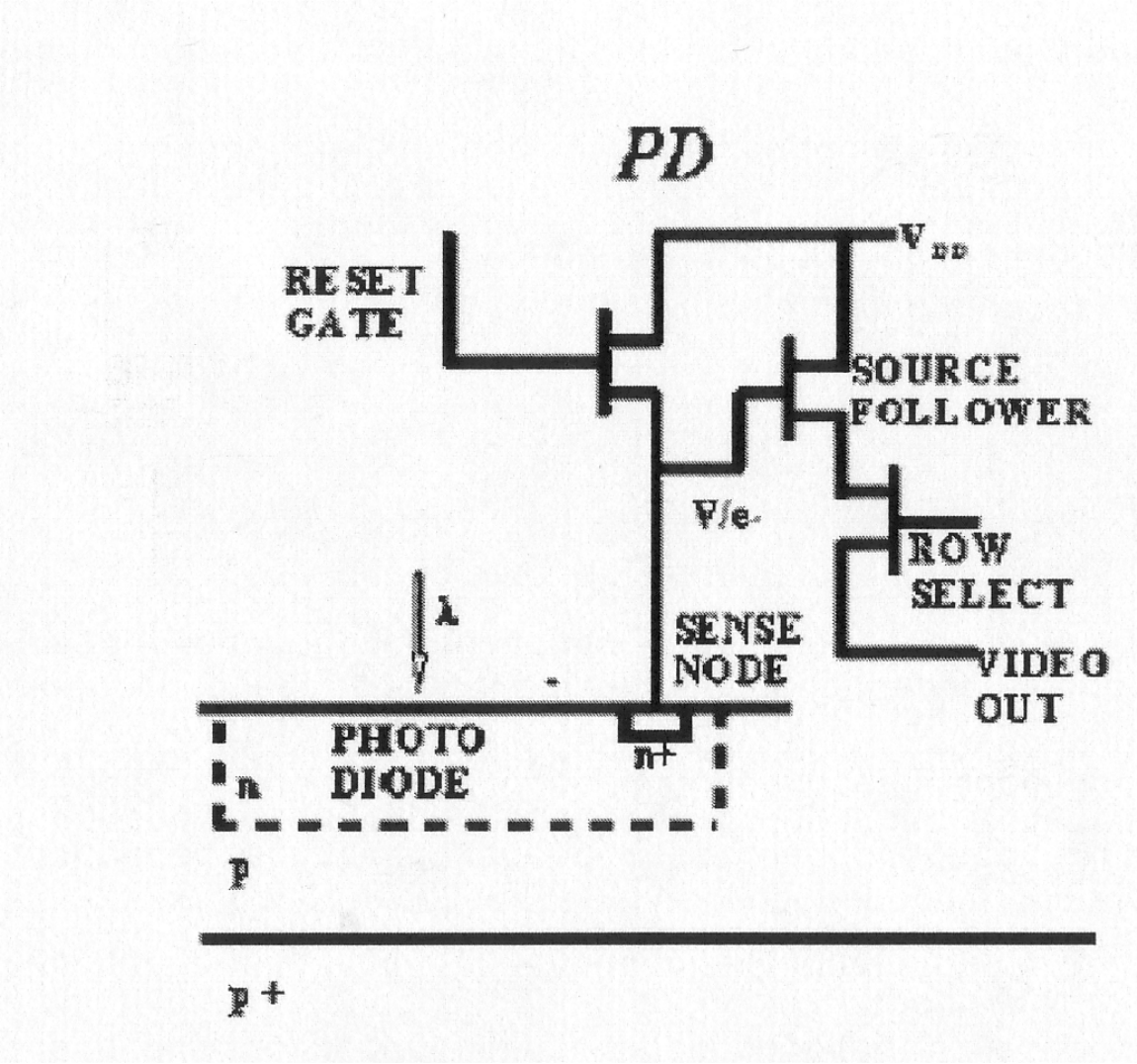

Fig.2.11. *Schematic of a three-transistor CMOS APS detector element*

Incident light results in the integration of charge on the photodiode's internal capacitance. The charge accumulation gives rise to a voltage change, proportional to the intensity of the incoming photon fluence at that point on the detector surface. The reset gate transistor acts as a reset switch. When turned on it effectively connects the

photodiode to the main power supply, clearing out the integrated charge. The source follower transistor is an amplifier that allows the voltage at the sense node to be observed without removing the accumulated charge. The row select transistor is used as a read-out switch to connect a row of pixels to the read-out electronic line.

A typical two-dimensional array of pixels is organized into rows and columns. Pixels in a given row share reset lines, so that a whole row is reset at a time. The row select lines of each pixel in a row are tied together as well. The outputs of each pixel in any given column are interconnected. Since only one row is selected at a given time, no ambiguity as to which pixel in the column is being read out occurs. Further amplifier circuitry is typically on a column basis.

Compared to CCDs, CMOS APS sensors offer several advantages. Since no charge movement is involved in the read out process, CMOS arrays can usually be read faster. Non-destructive read out can be employed for low signal applications. Finally, CMOS manufacturing technology is cheaper than that of CCDs.

Some relative weaknesses of the CMOS detector technology offset its strengths. Since both a light sensor and an amplifier are implemented on the same chip the photosensitive fraction of the detector surface is less than 100%. CMOS arrays often exhibit higher dark current and greater electronic noise than CCD-based detectors. Also CMOS panels suffer from image lag due to incomplete pixel reset. Image lag manifests itself as a residual signal left in the detector after a frame readout.

2.1.6 Hamamatsu C7940DP-03 CMOS flat-panel detector

As a result of the investigation of several x-ray detectors [3], we chose the Hamamatsu C7940DP-03 CMOS flat panel x-ray image sensor as a lower resolution, but faster readout alternative to the BC detector. Such an approach can be useful for situations in which a somewhat coarse anatomic map of the animal is to be acquired. The detector is comprised of a 2240 by 2344 rectangular matrix of 50 μm x 50 μm pixels. A165 μm thick CsI (Tl) converter with a columnar structure is directly deposited onto the imaging array. During readout, the image can be binned down by factors of 2 and 4, thus reducing data acquisition time. The sensor is able to acquire data at speeds of 2, 4 and 9 frames/seconds in 1x1, 2x2 and 4x 4 binning modes respectively.

The CMOS detector is connected via a differential RS-422 bus to a National Instruments PCI-1424 video frame grabber card installed in the host computer. The card digitizes the incoming video stream to 12 bits. An external detector trigger (to trigger image integration in the detector) is connected to one of the digital outputs of a NI PCI-6024E multifunctional data acquisition board, residing in the same PC. A custom-written interface, implemented in the LabView programming environment, controls the trigger and data read-out sequences and displays the acquired data frames. A snapshot of the interface main control panel is shown in Fig.2.12.

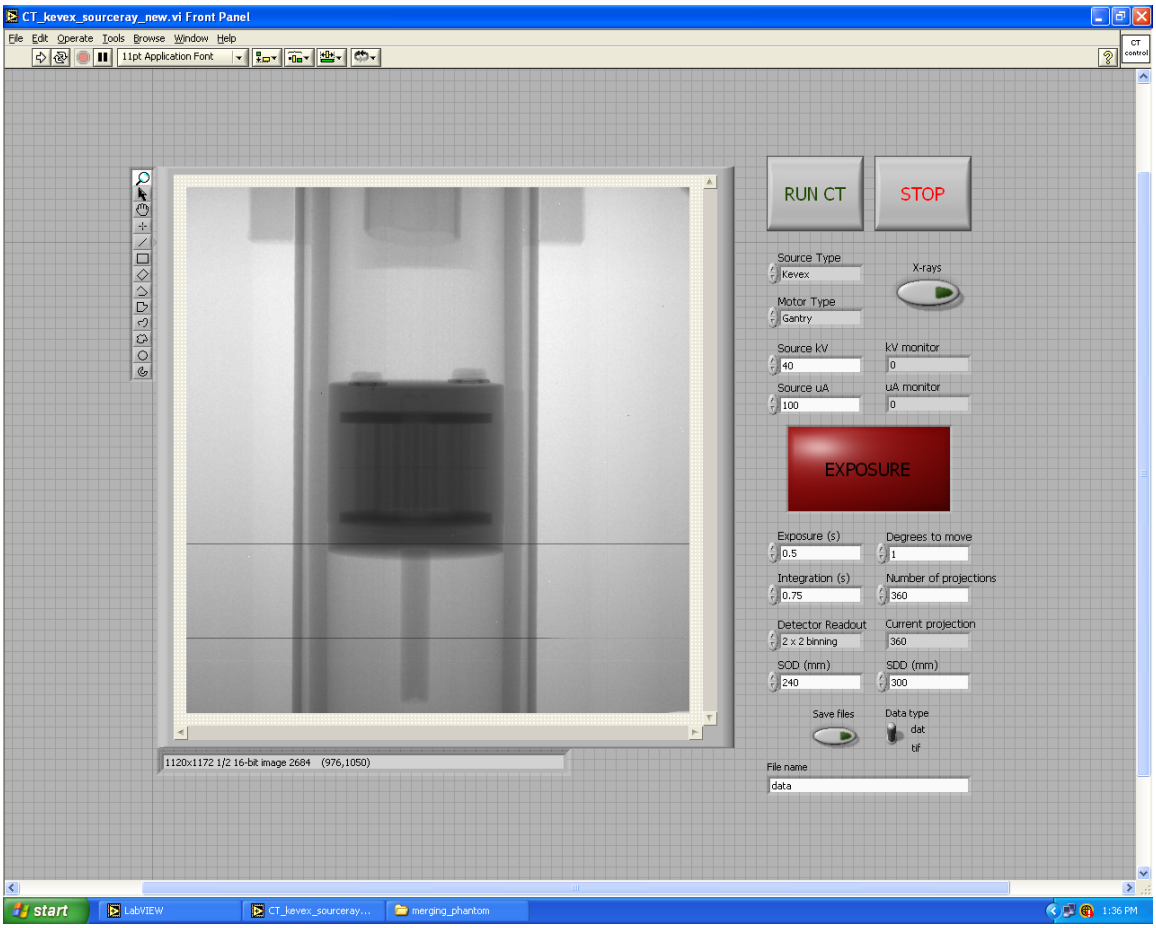

Fig.2.12. *Snapshot of CMOS detector interface*

CMOS detector interface does not contain any image correction algorithms. Instead raw data files are saved on a hard drive for external processing to increase the speed of data acquisition. Each image undergoes the same correction procedures as the images from CCD detector. This detector will sometimes be referred to as Hamamatsu.

2.2 X-ray sources

The X-ray source is an essential part of the x-ray CT imaging system. A general overview of x-ray physics was given in the introduction, so this subchapter will focus on the specific choices x-ray sources from the standpoint of small animal imaging.

The requirement for high spatial resolution rejects the possibility of using x-ray tubes employed in human scanners. The focal spot size of a typical tube used in general radiography varies from 0.2 mm to 1 mm. The effect of penumbra, created by the nonzero focal spot size, significantly degrades the spatial resolution of the system. This effect becomes more pronounced when a geometric magnification comes into play. The diagram in Fig.2.13 illustrates the phenomenon.

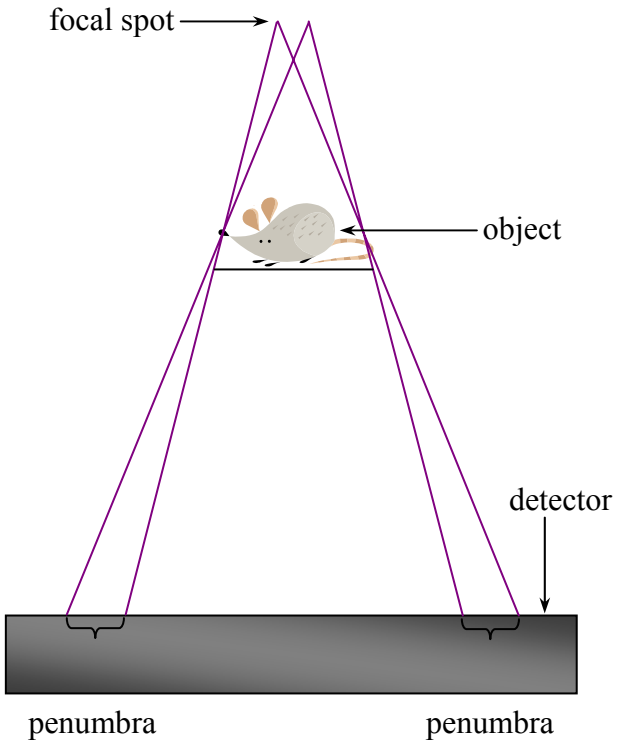

Fig.2.13. *Spatial resolution degradation due to a finite focal spot size*

For applications such as small animal imaging, micro-focus x-ray tubes have to be employed in order to achieve the desired spatial resolution. The spot size of micro-focus tubes varies from 5 μm to 75 μm depending on the output power. These tubes can be integrated into a small animal scanner with a digital detector with detector element size around or below 50 μm to achieve spatial resolution at the AOR that is under 50 μm.

In order to prevent radiation from reaching the animal and the detector when the gantry is being rotated in step-and-shoot mode, or during detector readout, a fast turn on/off response is a desirable feature in a micro-focus x-ray tube. However, the danger of damaging the anode target by excessive energy deposition requires careful control of high voltage and current ramping times. The achievable ramp timing depends on the focal spot size and it is common for a tube with 5-7 μm focal spot size to have a beam rise time of several seconds. Slow ramping is necessary because of a small energy deposition area and rapid delivery of electron beam can damage the target. Under those circumstances one must employ an x-ray mechanical shutter to control exposure.

The choice of the optimal target material and external filtration for small animal CT was based on the research published in [8]-[9]. Tungsten target tubes with approximately 1 to 2 mm aluminum of external filtration have been identified as the most advantageous choice. Unfiltered tungsten spectrum is dominated by characteristic L-shell emission lines with energies of 8.7 and 9.9 keV. 1 to 2 mm of aluminum provides adequate attenuation of these lower energy lines without significantly effecting useful higher energy x-rays.

2.2.1 Ultra-small focal spot size X-ray source

In order to take a full advantage of the high spatial resolution offered by the Big Chip detector it was paired with an ultra-small focal-spot size x-ray tube. Several manufacturers offer this type of tube. Our choice was the Kevex PXS5-926EA MicroFocus Portable X-ray Source from Thermal Electron Corporation (Scotts Valley, CA). This source combines the x-ray tube and high voltage power supply in a compact

package that is powered from a 12 VDC source. The tube is equipped with a tungsten target. The maximum target voltage is limited to 90 kV. The maximum electron beam current depends on the applied voltage and the focal spot size. The maximum dissipated power (tube voltage x beam current) is 8 W when using the largest available focal spot size.

The focal spot size and power rating vary from less than 5 μm in the 55-90 kV range with 4 W maximum power, to less than 9 μm over the 45-90 kV range with a maximum power of 8 W. The focal spot is located only 8.5 mm from the source's exit window allowing for high magnification factors. The exit window is made out of 0.13 mm thick beryllium. X-rays are confined to an output cone of illumination of 45 degrees wide. The source is governed via an external control module; the Kevex PSX5 Digital Controller. The controller can be connected to a PC or be run manually from its control panel. For tube safety, the electron beam current rise time for this source is extremely long, about 5 seconds for voltages between 0 to 50 kV, necessitating an x-ray shutter.

A simple yet robust shutter was implemented utilizing two general purpose pull-action 12VDC solenoids and an electromechanical relay (Omron G5A-234PH). The electric diagram of the shutter is shown in Fig. 2.14.

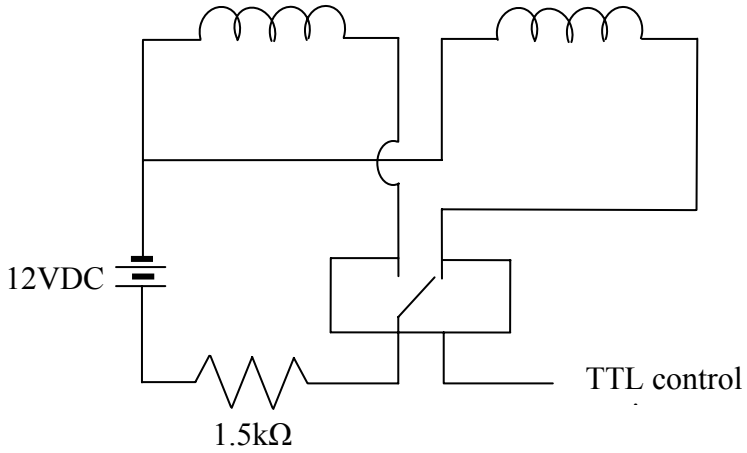

Fig.2.14. *Schematic of shutter electric circuit*

A carbon fiber plate with an approximately 40 mm x 40 mm x 2 mm piece of lead glued to it is mounted to the ends of solenoid shafts. A KGComp SPA05-12S power supply provides 12 VDC to the solenoids coils. One of the digital IO lines of the NI PCI-6024E card is used to control the relay output selection. Fig. 2.15 describes the shutter action. The shutter open/close times are about 100 milliseconds, limited mainly by the solenoid energizing time. The solenoids are rated at about 10^8 on/off cycles per life time and should last about 10 years at the normal rate of scanner operation.

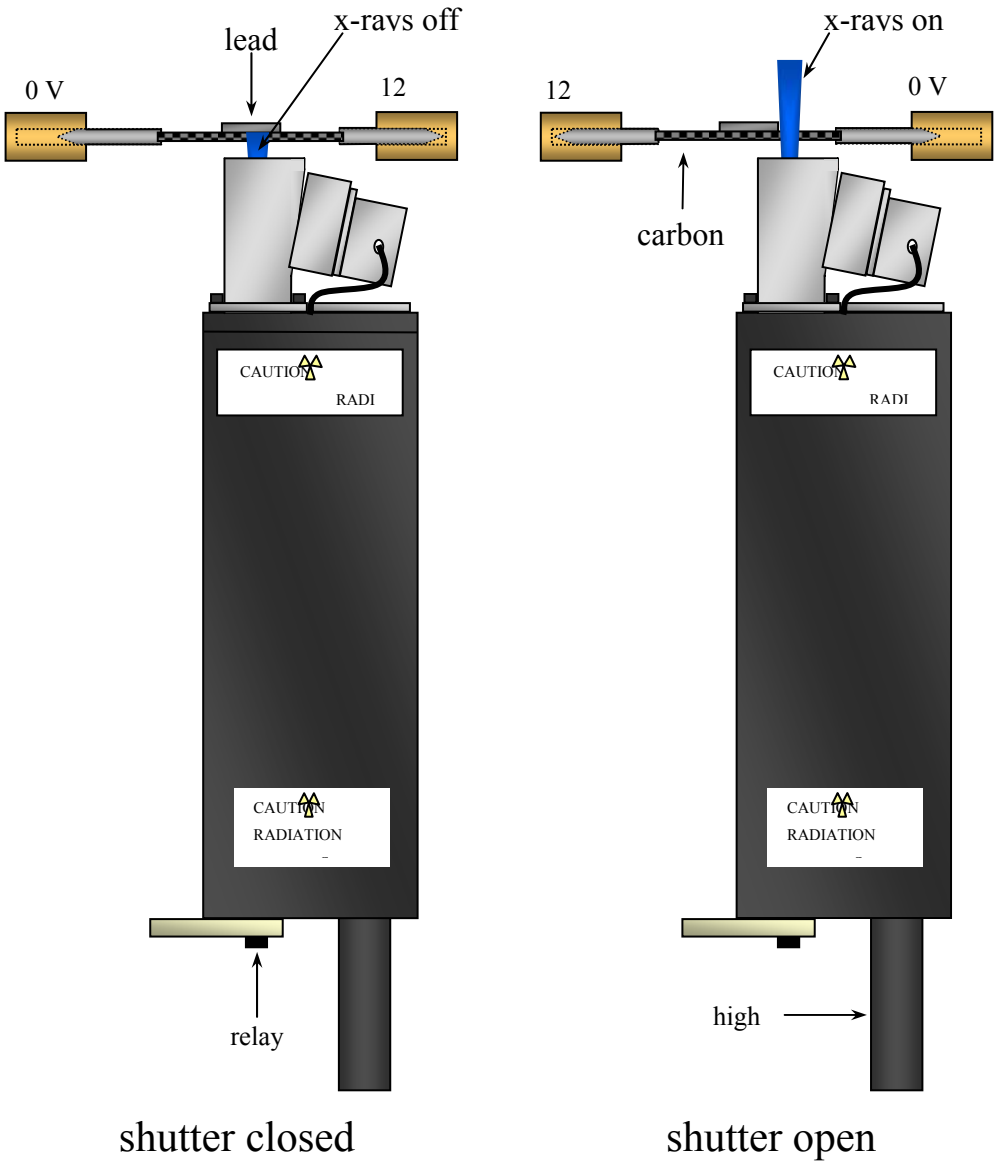

Fig.2.15. *Cartoon describing operation of a solenoid-based shutter*

A collimating aperture is installed between the tube output and the shutter plate. The purpose of this collimator is to confine x-rays to the detector surface, preventing unnecessary exposure to the animal and operator and reducing scattered radiation. The aperture accommodates a 1 mm thick aluminum beam filter.

2.2.2 High output microfocus X-ray source

Many small animal imaging studies do not require very high spatial resolution, but instead are very demanding in terms of image acquisition time. To keep image time short, these experiments require the use of high x-ray flux, necessitating a high output power x-ray source. For these situations, our scanner makes use of the Source-Ray Inc (Bohemia, NY) SB-80-1k fully integrated x-ray source. The source is capable of delivering 80 W of output power at a maximum voltage of 80 kV. It utilizes an Apogee-series x-ray tube from Oxford Instruments Plc (Scotts Valley, CA). The high voltage generator of the source is incorporated inside a common housing with the tube. External 24 VDC power is supplied by the Volgen model SPN150-24S power supply. The source is controlled from a host PC via the RS-232 serial bus. The focal spot size is estimated by the manufacturer to be 40-60 μm without a strong dependence on the output power. The maximum rise time of the electron beam is around 250 milliseconds. The x-ray beam is internally filtered by 1.8 mm of aluminum equivalent. The output cone is limited to 40 degrees, with the focal spot located 24.6 mm away from the output window.

2.3 Characterization of x-ray detectors

This subchapter presents the methodology and the results of measurements of basic imaging characteristics such as detectors' dark current and dark noise, dynamic range, sensitivity, the modulation transfer function (MTF), the noise power spectrum (NPS), and the detective quantum efficiency (DQE). Results will be presented graphically first and then summarized in a table for easier comparison of detectors.

2.3.1 Calculation of dark current and noise

Dark noise is an accumulation of heat-generated electrons in the sensor. The term "dark current" refers to the rate of generation of these electrons, most of which come from boundaries between silicon and silicon dioxide in the sensor. Constant bias introduced by thermally generated charge can be subtracted from an image. Thermal noise is random by nature and has an effect of reducing detector dynamic range by increasing lower detectable threshold.

To measure the detectors' dark noise, images were obtained with no x-ray source for a range of integration times, acquiring two dark images at each integration time. The images were acquired continuously with no time delay. Additionally, CMOS detector was read out prior to the dark frame acquisition in order to clean up the pixel wells from previously accumulated charge. Difference images were obtained by subtracting a dark image from the other one with the same integration time. The remaining noise in the difference image is characteristic of the dark noise in an x-ray image since dark frames are routinely subtracted from x-ray frames. Each difference image was divided into regions of interest (ROIs) of approximately 100 x 100 pixels. The RMS pixel-to-pixel fluctuations in analog-to-digital units were recorded for each ROI and the average across the ROIs is reported as the dark noise.

Dark current was obtained by plotting an average pixel count of every dark image versus detector integration time. Figs. 2.16 and 2.17 exhibit results of dark current measurement for CCD and CMOS detectors respectively.

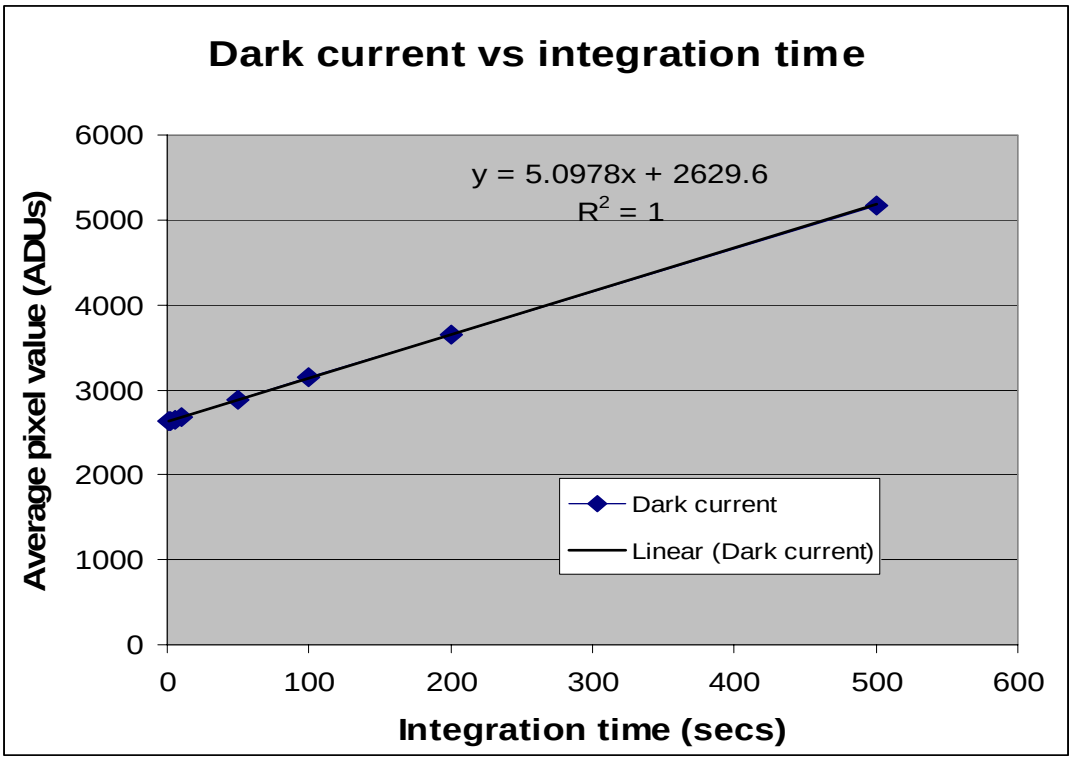

Fig.2.16. *Graph of CCD detector dark current*

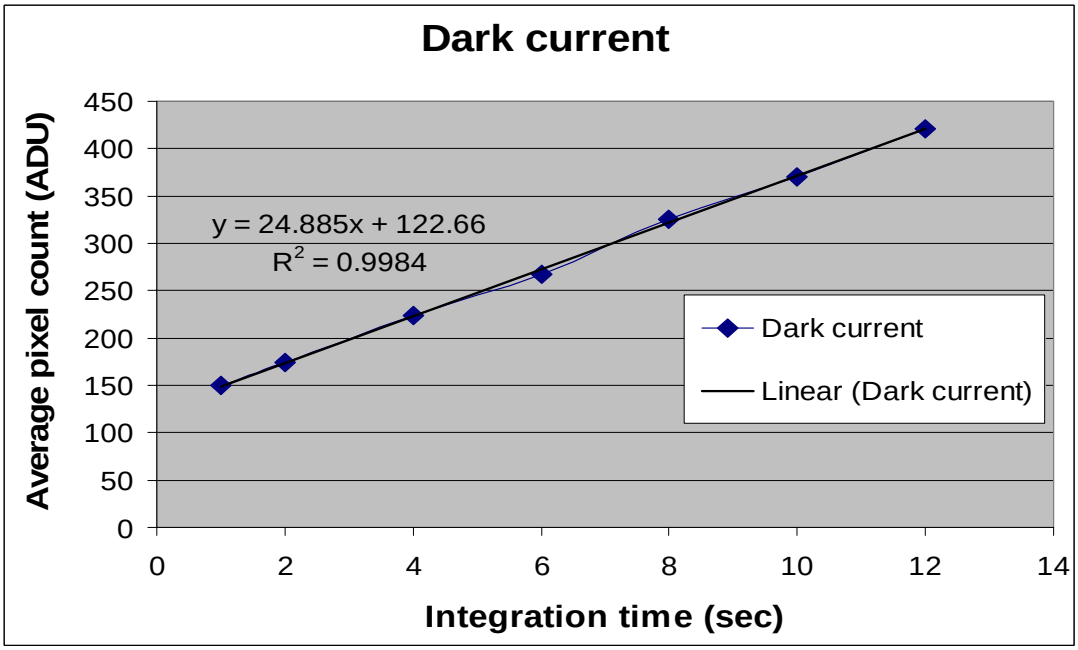

Fig.2.17. *Graph of CMOS detector dark current*

2.3.2 Calculation of sensitivity and dynamic range

Important characteristic of an imaging detector is its dynamic range. Dynamic range represents the range of usable signal in the image. The dynamic range of is defined as $\frac{I_{\max}}{I_{noise}}$, where $I_{\max}$ is the pixel value resulting from the maximum x-ray exposure for which the pixel value was a linear function of increasing exposure, and I_{noise} is the RMS dark noise calculated as described above. The sensitivity is defined as the rate of increase of the average pixel value in the image with increasing x-ray exposure. Only linear section of detector response curve is considered while calculating detector sensitivity. Figs.2.18 and 2.19 display dynamic range curves of CCD and CMOS detectors respectively. Linear part of detectors' response curve was conservatively chosen to end at the last data point that belongs to a linear fit within one standard deviation.

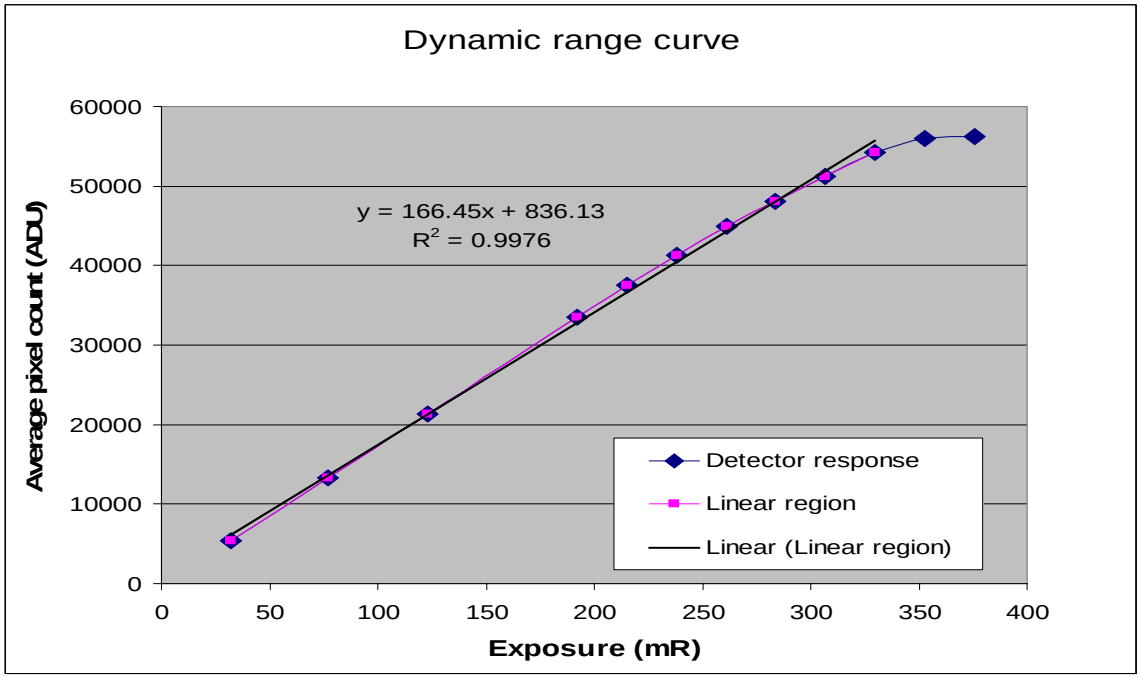

Fig.2.18. *Dynamic range curve with a linear response region CCD detector*

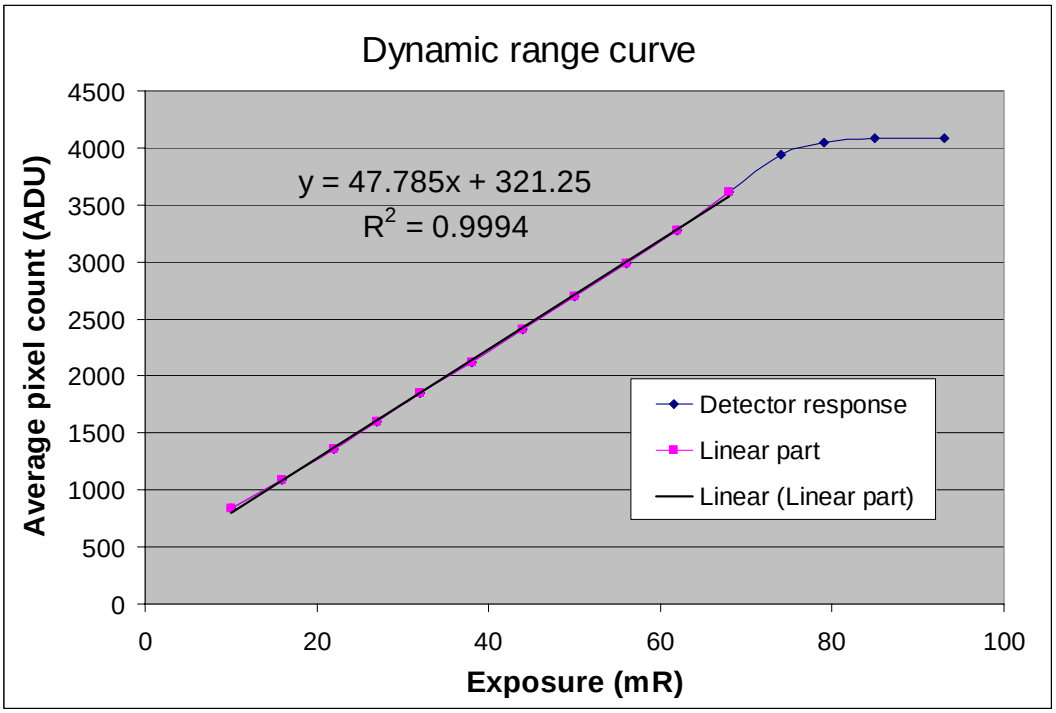

Fig.2.19. *Dynamic range curve with a linear response region CMOS detector*

A useful quantity directly observable from the curves above is a maximum detectable exposure. This quantity describes an upper limit on detector's ability to reliably detect incoming radiation.

2.3.3 Calculation of modulation transfer function

Since the performance of a detector depends on the size of the object being imaged, a single analysis in the spatial frequency domain can be used to predict detector response to all possible inputs. All real objects can be decomposed into sine waves of different frequencies, amplitudes and phases. Fourier transform is commonly used to convert from the spatial domain to spatial frequency domain. The modulation transfer function (MTF) of a system is a measure of spatial resolution and determines image sharpness. This means that the MTF measures the attenuation of each sinusoidal component from input to

output of a detecting system. In order to determine system MTF experimentally one must use sinusoidally varying x-ray inputs. Although sine wave patterns exist, it is very hard to generate one with high frequencies. More practical approach is to measure a system line spread function (LSF), which is a response of a system to infinitely narrow line input. Input signal can be described as a δ-function, so its Fourier transform is a constant in frequency domain. In other words input signal contains all possible spatial frequencies with the same amplitude. Then taking a Fourier transform of the output signal and normalizing it to its value at zero frequency will produce system's MTF.

The pre-sampling MTF was measured using a 10 μm wide slit positioned at a small angle with respect to the pixel matrix. The method has been introduced in [9]. MTF calculation algorithm was implemented in IDL (Interactive Data Language, ITT Visual Solutions, Boulder, CO).

The general method applied in the program is as follows: for a slit slant ratio *r*, a finely sampled line spread function (LSF) is obtained by making use of the different alignments of the center of the slit relative to pixel centers. Applying the Fourier transform to the highly sampled LSF produces the pre-sampling MTF of the system. This processed is repeated several times over the length of the slit to acquire an average pre-sampling MTF. MTFs of both detectors are presented in Fig.2.20. As can be observed from the graph, Big Chip detector exhibits superior modulation transfer properties than Hamamatsu detector over the entire frequency region. Commonly accepted type of comparison is to compare which spatial frequency corresponds to 10 % of an MTF. Big Chip's MTF falls down to 10% of its original value at ~ 16 cycles/mm, while the same

point for Hamamatsu detector is only ~ 4.5 cycles/mm. We will take a look at detectors' spatial resolution from a slightly different angle in chapter 5.

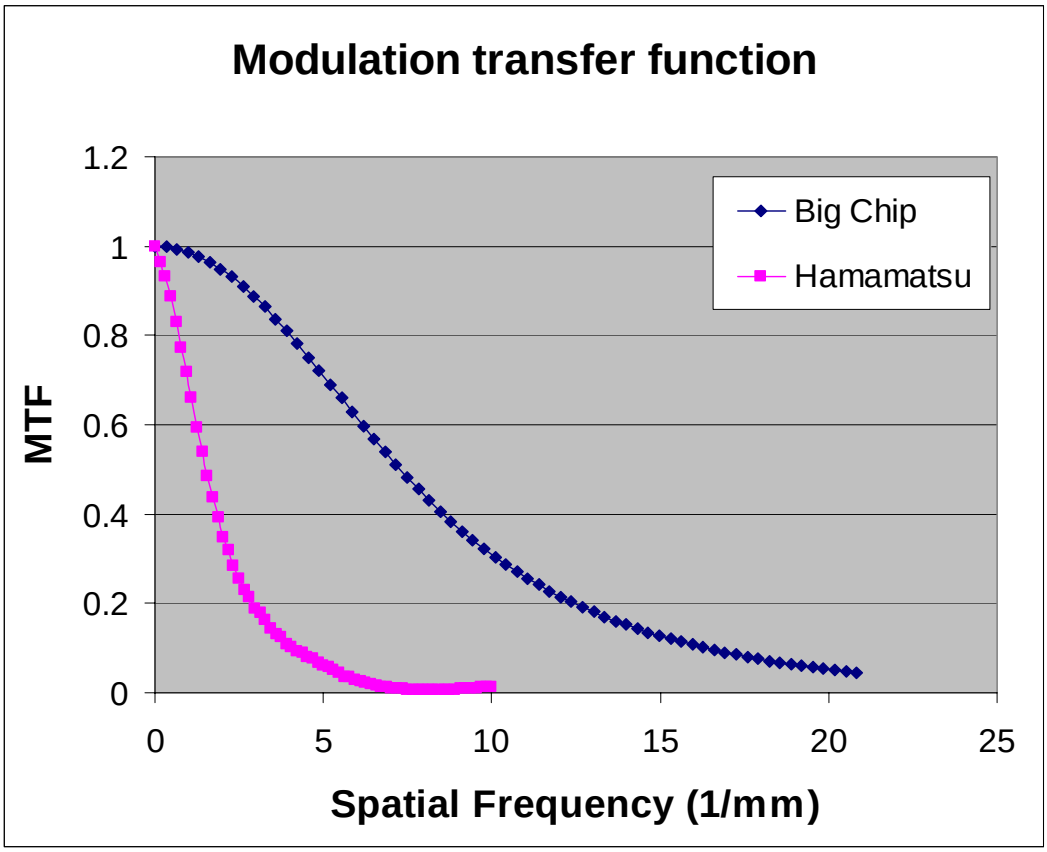

Fig.2.20. *Modulation transfer functions of CCD and CMOS detectors*

2.3.4 Calculation of noise power spectrum

The noise power spectrum (NPS) is a measure of the total noise recorded by an imaging system. The NPS is a Fourier decomposition of the variance (from all the noise contributions) of the system versus spatial frequency. Therefore, the total variance of a system can be obtained by integrating NPS over the entire spatial frequency range. Since NPS is a spectral decomposition of the variance, it provides an estimate of the spatial frequency dependence of pixel-to-pixel fluctuations present in the image. These

fluctuations are due to quantum or shot noise in the x-ray quanta incident on the detector, as well as from noise introduced by the conversion and transmission of the quanta in an imaging system. The mathematical derivation of quantitative application of NPS techniques are described in detail in [7]. NPS can be calculated directly from the square of the modulus of Fourier transform of the data.

Three noise sources can be identified in digital x-ray detectors. First is an x-ray quantum noise, which is due to variations in the number of x-rays interacting in the converter. The second noise source is secondary quantum noise which is due to quanta other than primary quanta, like visible photons produced in the phosphor and electrons generated by digital detector. These secondary quanta produce fluctuations in the number of quanta per unit area observed which is uncorrelated to primary quantum noise. The third noise component in an electronic detector is due to the inherent fluctuations in the output signal of the detector (i.e. random generation of electrons in the readout process). This is called detector or dark noise and it was discussed above.

The methodology for noise power spectrum calculation is described in [8] and will be only summarized here. The NPS was estimated by obtaining a set of uniform illumination images for a range of exposures. An acrylic plate about 1 cm thick was used to emulate realistic x-ray spectrum condition. An ion chamber (model 06-526-5290, Nuclear Associates, Inc, Long Island, NY) was used to measure the exposure at the detector surface. The NPS estimates reported here were obtained from the 2-dimensional Fourier transforms of the difference images, and therefore include contributions only from uncorrelated noise sources, since the difference operation removes spatially fixed noise. For each difference image, contiguous 128 x 128 pixel regions of interest (ROIs)

were extracted, and the 2-D NPS was estimated from each. This resulted in 364 and 253 NPSs for the Big Chip and Hamamatsu detectors respectively. For each detector, the averaged NPS was divided by two to estimate the NPS due to uncorrelated noise in a single image. Finally, the NPSs were normalized by x-ray fluence to test the limit of quantum limited operation. The detector is said to operate in quantum limited regime when x-ray shot noise dominates the other noise sources, approximating total noise of the system to be Poisson distributed. Since NPS is a Fourier decomposed variance, it should be proportional to the total number of incoming quanta, or in other words fluence. Exposure is in turn directly proportional to fluence, so in quantum limited regime fluence normalized NPS should be exposure independent. NPSs are shown in Figs.2.21 and 2.22.

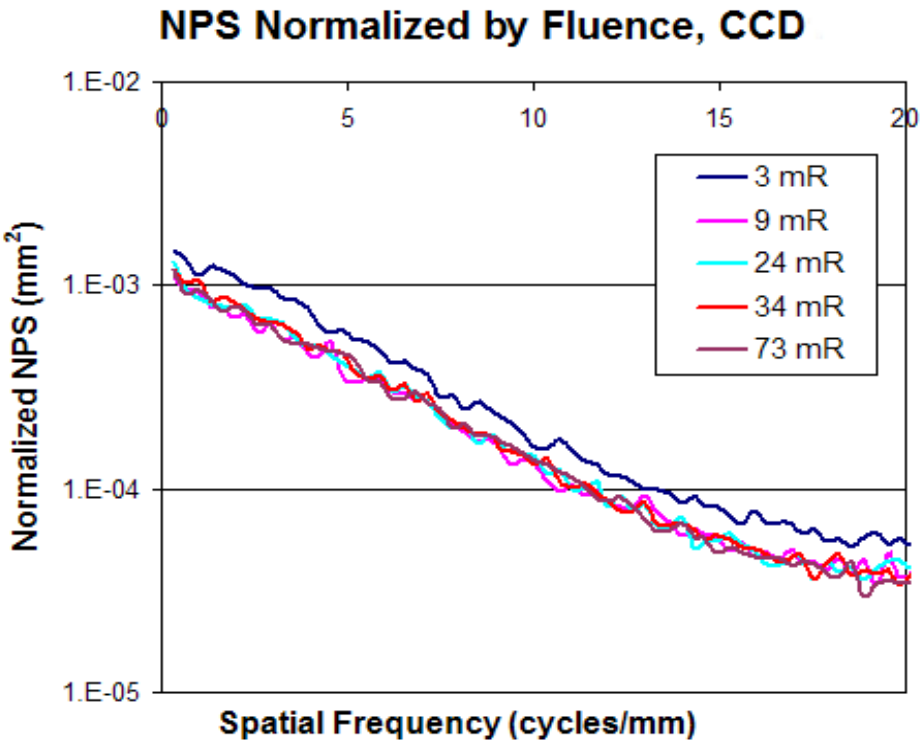

Fig.2.21. *Normalized NPSs of Big Chip detector*

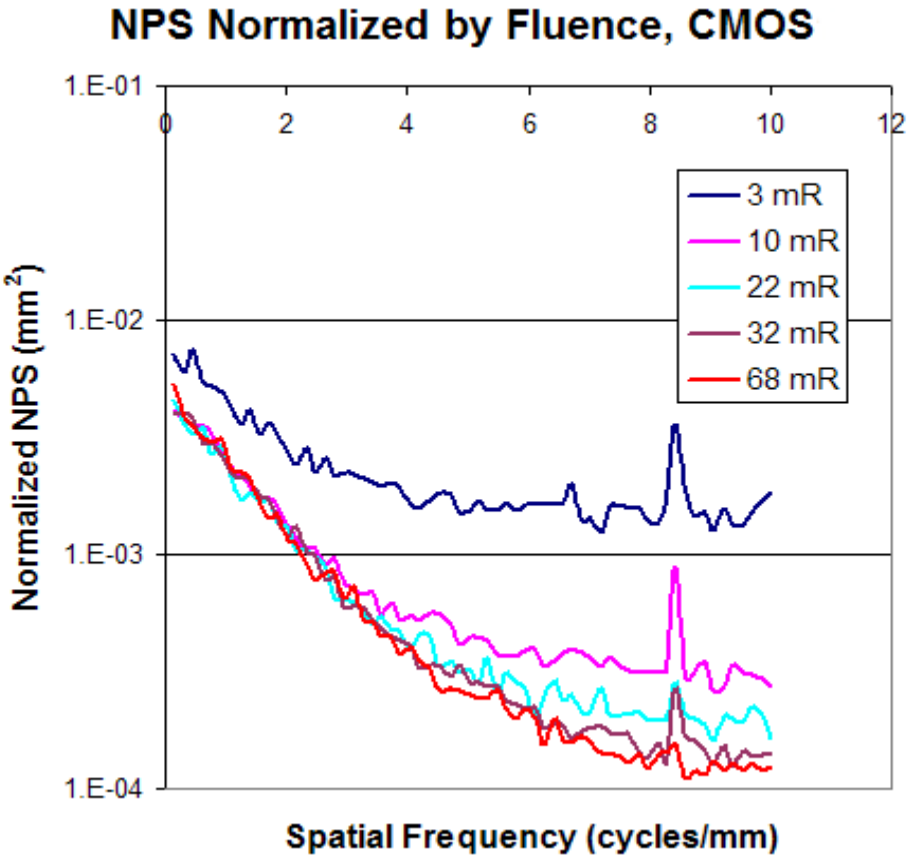

Fig.2.22. *Normalized NPSs of Hamamatsu detector*

It is easy to notice that both detectors are not quantum limited at 3mR of x-ray exposure. The lower detectable limit for both detectors is in between 3 and 9mR, with Big Chip's limit probably lower than that of Hamamatsu detector.

2.3.5 Calculation of detective quantum efficiency

The detective quantum efficiency (DQE) of an imaging system is perhaps the best known way to describe the performance of an imaging system under ideal conditions relying on hard objective data. The DQE is defined as the square of the ratio of the output signal-to-noise ratio (SNR) to the input SNR:

$$DQE \equiv \frac{SNR_{out}^2}{SNR_{in}^2} \tag{2.2}$$

For a system in which the input consists of uncorrelated quanta (Poisson distributed), the square of the input SNR is equal to the average incident quanta per unit area (x-ray fluence, usually represented by symbol Φ). The output signal is equal to the input fluence times the average system gain, G (relates the input and output signals) times system MTF, where the input signal consists of δ-function in the form of slit image. The output noise is actually the NPS described above. Expressed in terms of experimentally measurable quantities, the spatial frequency dependent DQE is given as follows [8]:

$$DQE(f) = \frac{SNR_{out}^2}{SNR_{in}^2} = \frac{\overline{\Phi}\overline{G}^2 MTF^2(f)}{NPS} \tag{2.3}$$

where Φ denotes x-ray fluence and G stands for conversion gain, a quantity that relates detectors' measurable response to a single incoming x-ray photon. The photon fluence per unit exposure for a monochromatic beam of photon energy E is [8] :

$$\frac{\Phi}{X} = \frac{(2.58 \times 10^{-4})W}{Ee\dfrac{\mu(E)}{\rho}} \tag{2.4}$$

where W is the ionization energy of air (33.85 eV), e is the electron charge (1.6×10^{-19} C), and μ(E)/ρ is the mass absorption coefficient of air at energy E. The factor of 2.58 $\times 10^{-4}$ C defines the roentgen as the exposure required to produce 2.58×10^{-4} C per kilogram of air. For a polychromatic beam of known shape, an effective energy approximation can be utilized. Effective energy is calculated as follows

$$E_{eff} = \frac{\sum_i N_i E_i}{\sum_i N_i} \tag{2.5}$$

where N_i and E_i are i-th bin value and i-th bin number of the x-ray spectrum respectively. Substituting E_{eff} to the right hand side into (2.4) fluence is calculated. Gain is calculated by dividing average pixel count of a flood corrected image at given exposure by the fluence per detector pixel. Effective energy of the beam used in this study was calculated to be 17.5 keV.

Figs. 2.23 and 2.24 show calculated detective quantum efficiencies of CCD and CMOS detectors for 4 different exposures.

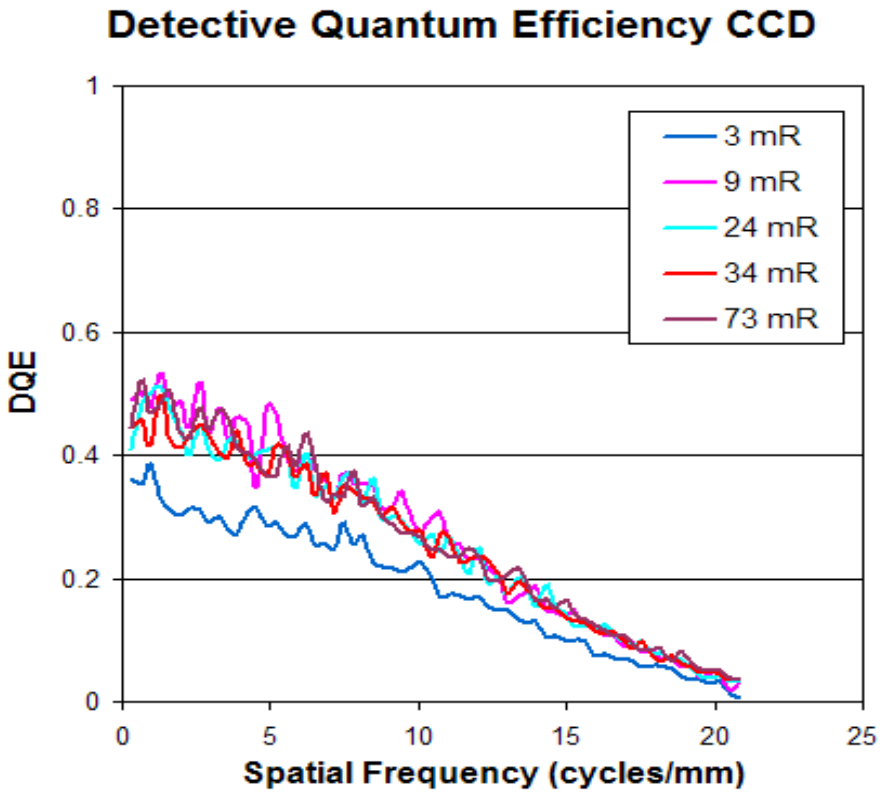

Fig.2.23. *DQE of Big Chip detector*

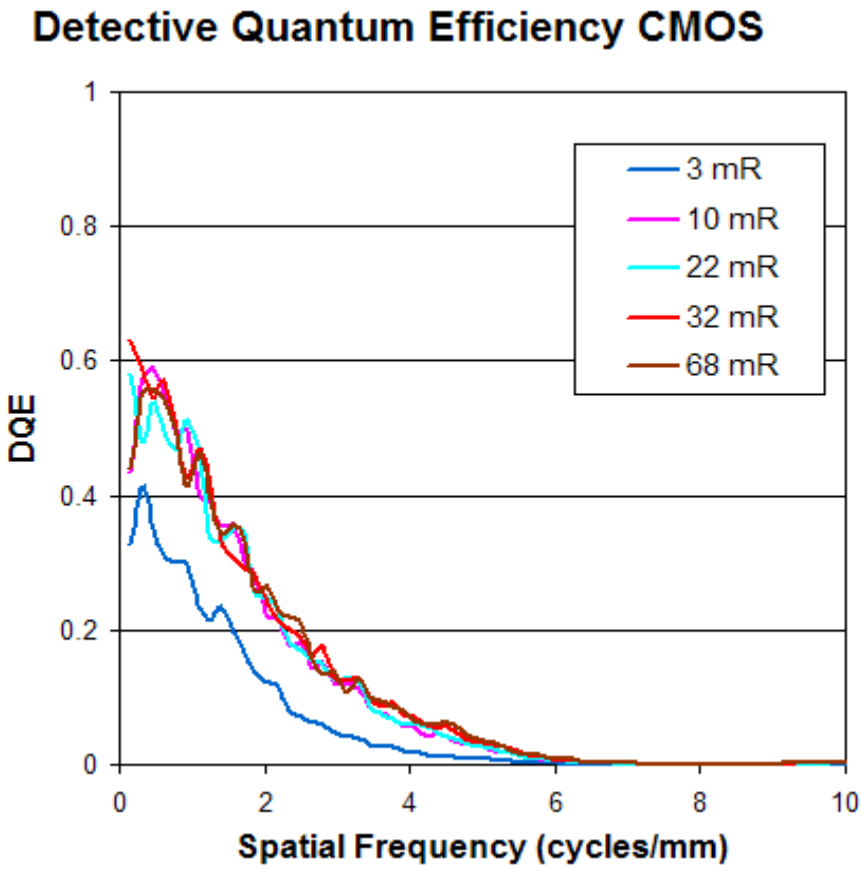

Fig.2.24. *DQE of Hamamatsu detector*

DQE graphs show the deviation from the quantum limited behavior for both detectors at the lowest exposure used. Detective quantum efficiencies of both detectors are shown in Fig.2.25.

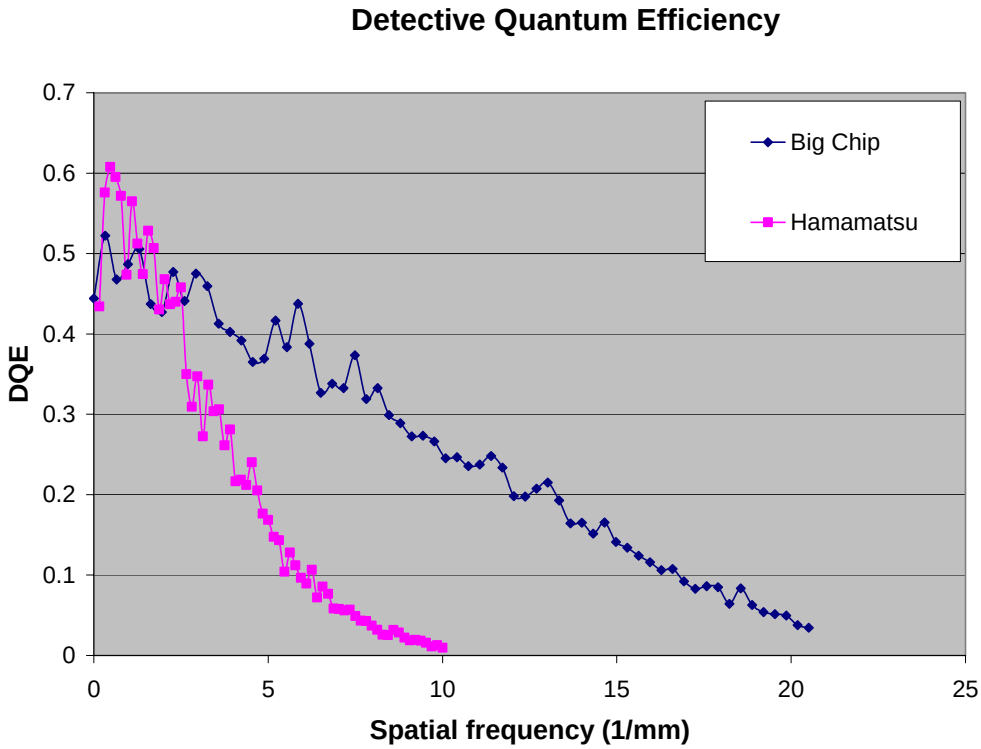

Fig.2.25. *DQE of Big Chip measured at 73 mR and of Hamamatsu measured at 68 mR*

As can be seen DQE of CCD detector outperforms that of CMOS detector everywhere except for very low spatial frequencies. DQE results at low frequency are not out of the ordinary. It can be shown that DQE at zero frequency numerically equals to absorption efficiency of the x-ray converter. Gadolinium oxysulfate phosphor screen used in CCD detector has absorption efficiency ~ 50 % for the given energy, while absorption efficiency of 160 microns thick CsI is ~ 65 %.

2.3.6 Summary and conclusions

Comprehensive evaluation of detector imaging performance has been carried out. Table 2.1 gives basic detector information and summarizes results of the analysis.

	Big Chip	Hamamatsu
Technology	CCD	CMOS
Active area (cm^2)	8.62 x 4.92	11.2 x 11.7
Imaging matrix	3590 x 2054	2240 x 2344
Detector element size (μm)	24 x 24	50 x 50
Maximum linear pixel value (ADU)	54000	3940
RMS dark noise (% of maximum linear pixel value, for 5 seconds acquisition)	0.024	0.4
Sensitivity ($ADU/mR \div ADU_{max}$)	0.0036	0.0121
Maximum detectable exposure	280	82
Dynamic range	4240	990
Spatial frequency corresponding to 10% MTF (cycles/mm)	16	4.5
Maximum frame rate (frames/sec)	.16	2

Table 2.1 *Comparative listing of detectors' parameters*

A quick look at the table reveals that CCD detector is better in almost any respect. It showed higher spatial resolution; exhibited lower noise; it can detect wider range of signals; it is more sensitive than CMOS counterpart. Reasonable question to ask here is "Why do you want to use a CMOS detector at all?" There are two reasons we chose to utilize this detector in the scanner. First, it has larger imaging area than CCD detector. Larger area detector would allow for a greater variety of animal studies. Results of an animal experiment, which would be impossible to conduct with Big Chip detector will be shown in chapter 5. But more importantly Big Chip in its current configuration is a

relatively slow detector. Readout time of 6 seconds per frame is too long for *in vivo* experiments. Attempts to address the problem are under way at the time of writing, but it will take some time to resolve all the issues. Big Chip detector is used as a specimen imager, excelling in imaging extracted small-animal organs. Meanwhile Hamamatsu, though inferior in imaging characteristics, has proven itself to be a reliable fast detector. Many small animal imaging applications require only an approximate organ map of the animal. We're routinely applying 2 x 2 binning to Hamamatsu imaging array to raise its readout speed to 4 frames/sec. In this case the entire scan takes about 4 minutes. So a CMOS detector can provide respectable animal throughput and still deliver decent image quality, as will be demonstrated in chapter 5.

References

[1] Cho M.H. et.al., "*A flat panel detector based micro CT system: performance evaluation for small-animal imaging*", Phys.Med.Biol., vol.43, pp. 4173-4185, 2003

[2] Goertzen A.L., Nagarkar V., Street R.A., Paulus M.J., Boone J.M., Cherry S.R.,*"A comparison of x-ray detectors for mouse CT imaging*", Phys. Med. Biol., vol.49, pp. 5251–5265, 2004

[3] Stolin A.V., Kundu B.K., Pole D.J., Williams M.B., "*Characterization and comparison of X-ray detectors for use in small animal imaging",* 2004 IEEE Nucl. Sci. Symp. Conf. Rec., vol. 6, pp. 3480 – 3483, 16-22 Oct. 2004

[4] Zhao W., Ristic G., Rowlands J.A., *"X-ray imaging performance of structured cesium iodide scintillators",* Med. Phys., vol. 31, no. 9, pp. 2594-2605, 2004

[5] Sheppard S.T., Melloch M.R., Cooper J.A., "*Experimental demonstration of a buried-channel charge-coupled device in 6H silicon carbide*", IEEE Electron Device Letters, vol.17, no. 1,pp. 4-6, 1996

[6] Nagarkar V.V., Gordon J.S., Vasile S., Xie J., Phillips W.C.,"Improved X-ray converters for CCD-based crystallography detectors", SPIE vol.2519, no.2-11, 1995

[7] Cunningham I.A., Westmore M.S., Fenster A., "*A spatial-frequency dependent quantum accounting diagram and detective quantum efficiency model for signal and noise propagation*", Med. Phys., vol.21, pp. 417-427, 1994

[8] Williams M.B. et. al., *"Analysis of detective quantum effeiciency of a developmental detector for digital mammography*," Med. Phys. 26 (11), 2273-2285, 1999

[9] Fujita H. et.al., "*A simple method for determining the modulation transfer function in digital radiography*", IEEE Trans. Med. Imag., vol. 11, pp.34-39, 1992

CHAPTER 3
Gamma imaging subsystem

Constituents of a SPECT subsystem were discussed in general terms in the introduction. Imaging gamma detector and collimator are the main components. Their imaging characteristics will to a large degree determine performance of the whole system. This chapter is devoted to the evaluation of gamma detectors and pinhole collimators. First, the results of investigation of pinhole collimators will be presented and some general conclusions will be drawn. Then gamma imaging detectors will be described and their basic imaging characteristics will be revealed. Based on results of the pinhole evaluation, new image acquisition geometry will be introduced. To take a full advantage of the acquisition geometry, a novel type of pinhole collimator will be brought in and its imaging qualities will be explored and compared to those of conventional apertures.

3.1 Analysis of imaging characteristics of pinhole collimators

In small animal pinhole imaging, the mouse or rat is positioned near the pinhole to maximize detection efficiency. In this geometry, the majority of the gamma rays transmitted by the pinhole originate from points off of the pinhole axis. Gamma rays whose trajectory through the pinhole is at an angle θ with respect to the pinhole axis, strike the surface of planar gamma detectors with incident angle θ relative to the normal to the surface. Thus the angle of incidence on the detector surface can be as large as the

half-angle of the pinhole. The exponential absorption probability in the detector results in a depth-of-interaction (DOI) blur that increases with increasing angle from the pinhole axis, making the effective point spread function (PSF) of the detector vary with the location of the emitting source relative to the pinhole axis. This problem has been recognized by others, and recently the DOI blur has been modeled in the context of small animal SPECT by Hwang et al. [1]. Fig.3.1 shows a diagram visualizing DOI effect.

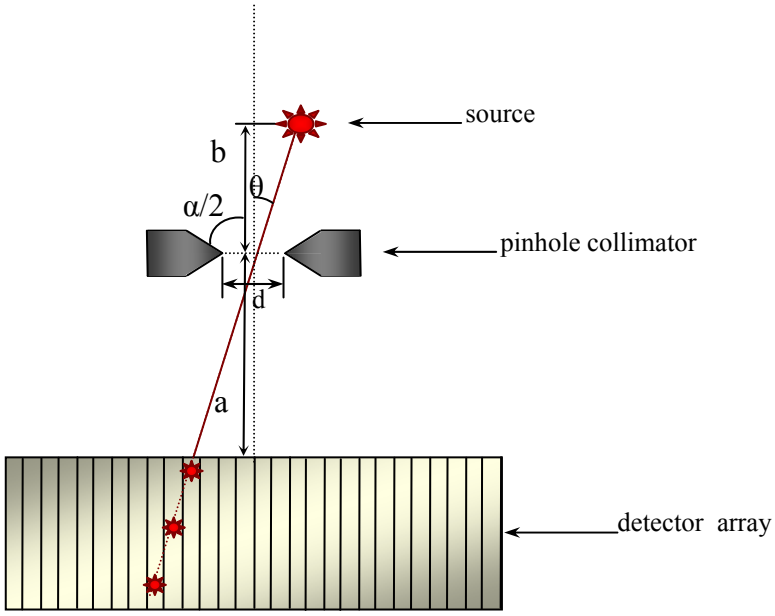

Fig.3.1. *Diagram describing pinhole imaging and depth of interaction effect (DOI).*

A second factor affecting spatial resolution is the changing PSF of the pinhole with increasing angle θ of the source from the pinhole axis. The gamma rays transmitted by the pinhole are the sum of those passing through the pinhole aperture (the geometric component) and those that penetrate the collimator material near the aperture (the penetration component). As θ increases, the solid angle subtended by the pinhole aperture at the point of gamma emission decreases as the aperture is viewed at an increasingly oblique angle. Simultaneously, the path length for penetration through the collimator

material lengthens, thereby decreasing the probability of transmission. Reduction in these two components has the effect of reducing the effective pinhole size in one dimension, for example making the effective shape of a circular pinhole become elliptical. The magnitude of the penetration component at any given angle off axis depends on the pinhole type (knife edge or channel), the pinhole angle, the collimator composition, and on the gamma ray energy.

The reduction in the effective pinhole size with increasing θ also causes the well known decrease in efficiency of pinhole collimators with increasing distance of the source from the pinhole axis [2]. As described above, this decrease is a result of decreases in both the geometric and penetration components.

For the SPECT component of the scanner, the above factors will determine how well spatial resolution and efficiency are maintained throughout the ~ 4 cm x 4 cm x 6 cm volume to be imaged. In principle, degradation of spatial resolution due to DOI blur can be reduced through the use of a thin detector, with an accompanying decrease in efficiency, or by designing a detector capable of measuring the depth of interaction of each event. Another potential way to minimize the impact of DOI blur is to design the detector so that large gamma ray incident angles are avoided. For example, multiple small detectors could be arranged in curved arrays so that the center normal of each detector intersects the pinhole [3]. One goal of this study is to characterize the change in efficiency and overall camera resolution as the source is moved away from the pinhole axis, and a second goal is to determine the impact of DOI resolution loss in planar detectors.

3.1.1. Pinhole sensitivity

The theoretical pinhole sensitivity has been calculated using the formalism of Metzler et al. [2]. As a function of the angle θ between the pinhole axis and the line from the source through the pinhole center, the sensitivity is:

$$S_{total}(\theta) = S_{geom}(\theta) + S_{pen}(\theta) \tag{3.1}$$

where $S_{total}(\theta)$ is the total sensitivity, and $S_{geom}(\theta)$ *and* $S_{pen}(\theta)$ are the geometric and the penetrative components respectively. The corresponding components for efficiency can be obtained by dividing by 37000 cps/μCi. For a circular pinhole of aperture diameter d and pinhole angle α:

$$S_{geom}(\theta) = d^2 \cos^3\theta / 16b^2 \tag{3.2}$$

$$S_{pen}(\theta) = \frac{\cos^3\theta}{4\pi b^2} \int_0^{2\pi} d\phi \int_{d/2}^{\infty} d\rho \; \rho \exp[-\mu \Delta L(\theta, \phi, \rho)] \tag{3.3}$$

The variables θ, ϕ, and ρ define a spherical polar coordinate system with the origin at the pinhole center. The polar angle θ is measured relative to the pinhole axis. In (3.3) the source is presumed to be located at an angle θ, and a distance *b* above the plane of the pinhole (defined by $\theta = \pi/2$). $\Delta L = \Delta L(\theta,\phi,\rho)$ is the path length of the photon through the collimator material, thus $\exp(-\mu\Delta L)$ is the probability of penetration through the collimator material with linear attenuation coefficient μ.

The sensitivity, averaged over the field of view of the pinhole is:

$$\overline{S} = \frac{\int_0^{\alpha/2} S(\theta)d\theta}{\int_0^{\alpha/2} d\theta} \tag{3.4}$$

where α is the pinhole angle, and $S(\theta)$, is the total sensitivity given by (3.1).

3.1.2. Pinhole spatial resolution

The system spatial resolution for pinhole collimation is given by Anger [4]:

$$R_s = \left[d_e^2 \left(1 + \frac{1}{M}\right)^2 + \left(\frac{R_i}{M}\right)^2 \right]^{1/2} \tag{3.5}$$

In (3.5), d_e is the effective pinhole diameter given by:

$$d_e = [d(d + 2\mu^{-1} \tan(\alpha/2))]^{1/2} \tag{3.6}$$

where M is the magnification factor, and R_i is the intrinsic detector resolution. The magnification factor is defined as the ratio a/b, where *b* is the perpendicular distance of the source from the pinhole plane, and *a* is the perpendicular distance between the plane of the pinhole and the plane of the detector (see Fig. 3.1). Although it is used in (3.5) to predict system spatial resolution, the expression for d_e in (3.6) is based on an analysis of pinhole sensitivity rather than on pinhole blurring. That is, it was derived by calculating the diameter of a perfect pinhole ($\mu = \infty$) necessary to result in the same total gamma transmission as a real pinhole with both aperture transmission (the geometric component) and transmission through the collimator material adjacent to the aperture (the penetration component). Thus while this model permits an improved estimate of pinhole resolution

relative to simply ignoring the penetration component, it provides no information about the shape of the pinhole point response function (PRF).

For knife edge pinholes, transmission is a decreasing function of the distance between the pinhole center and the point of incidence of a photon with the pinhole plane. Therefore the spatial distribution of the transmitted photons on the detector surface will not be circular (i.e. the pinhole PRF will not be cylindrical), but instead will have a central region of uniform intensity surrounded by a region in which the intensity decreases with increasing distance from the center of the circular region. Using a model similar to that used by Metzler et al. [2] Smith and Jaszczak [5] derived a more general expression for the effective pinhole diameter when the ray trajectories are no longer parallel to the pinhole axis, as is the case for off-axis sources:

$$d_e(\theta) = \{d^2 + \frac{4}{\pi}\int_0^{2\pi} d\phi \int_{d/2}^{\infty} d\rho\, \rho \exp[-\mu \Delta L(\theta,\phi,\rho)]\}^{1/2} \tag{3.7}$$

In (3.7) the first term under the radical accounts for gamma rays whose path intersects the pinhole aperture (i.e. the geometric term), and the second accounts for gamma rays transmitted through the pinhole material (the penetration term).

Metzler et al. [6] have described a model for the pinhole PRF. For a circular pinhole of aperture diameter d and pinhole angle α, the PRF is:

$$PRF = \begin{cases} \dfrac{\cos^3(\theta)}{4\pi(a+b)^2}, & r \le \dfrac{d(a+b)}{2b} \\ \dfrac{\cos^3(\theta)}{4\pi(a+b)^2}\exp(-\mu\Delta L), & r > \dfrac{d(a+b)}{2b}, \end{cases} \tag{3.8}$$

The imaging plane is parallel to the pinhole plane and is located a distance *a* from it on the opposite side from the point source. The variable r represents the radial distance in

the imaging plane between the point at which the PRF is being evaluated and the projection onto the imaging plane of the source through the pinhole aperture center. As in (3.3), $\Delta L=\Delta L(\alpha,\theta,\beta,\rho)$ is the path length of the photon in the collimator material, where β is the azimuthal angle of the intersection of the gamma ray trajectory with the pinhole plane.

In this study, the theoretical spatial resolution to be compared with the measured resolution was calculated using two different models. In the first model, the value for d_e, determined by numerical integration of (3.7), was substituted into the expression for the system resolution (3.5), taking R_i equal to the FWHM of the measured detector line spread function (LSF). In the second model, both ϕ and β were set equal to 0 in the expression for the angle-dependent path length ΔL, thereby reducing the pinhole PRF of (3.8) to a one-dimensional function of the variable r. The theoretical system LSF was then calculated by numerically convoluting the resulting 1-dimensional function with a Gaussian function representing the LSF of the gamma detector. Figs. 3.2 and 3.3 show examples of the theoretical system LSF calculated in this way for two different magnification factors (M = 1.5, and M = 3.0). Also shown are Gaussian functions fitted to the theoretical system LSF. The FWHM of the fitted Gaussian function was recorded as the theoretical resolution. This was done rather than simply using the FWHM of the theoretical system LSF itself in order to be consistent with the manner in which we report the measured resolution (as the FWHM of a Gaussian function fitted to the spatially averaged LSF). The above two methods for calculating the theoretical system resolution will be referred to as Models 1 and 2, respectively.

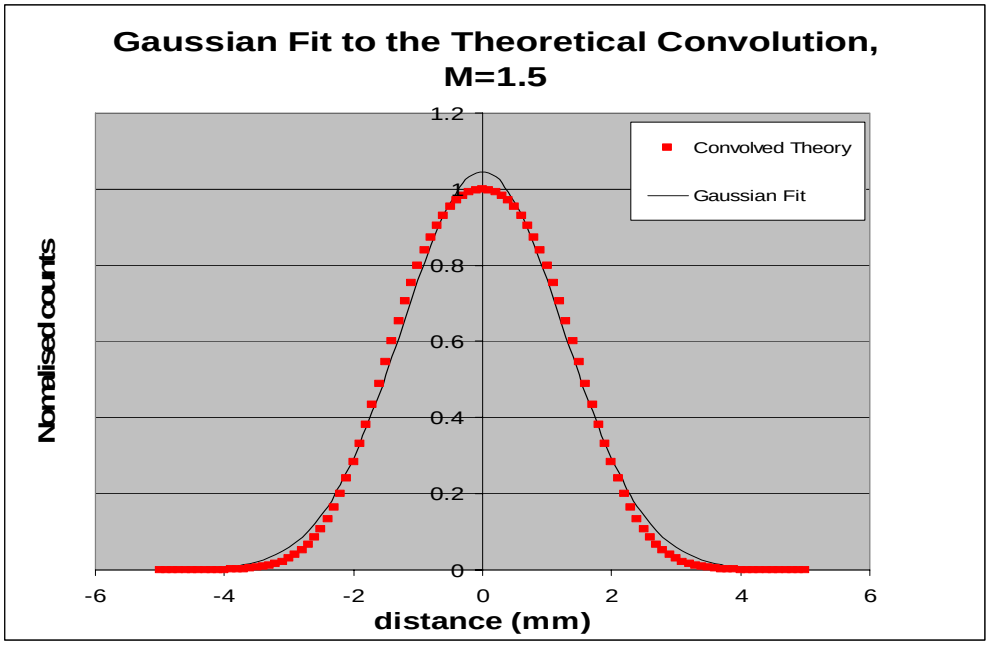

Fig.3.2. *Gaussian fit to the convolution between the 1-dimensional pinhole PRF and the planar detector LSF.*

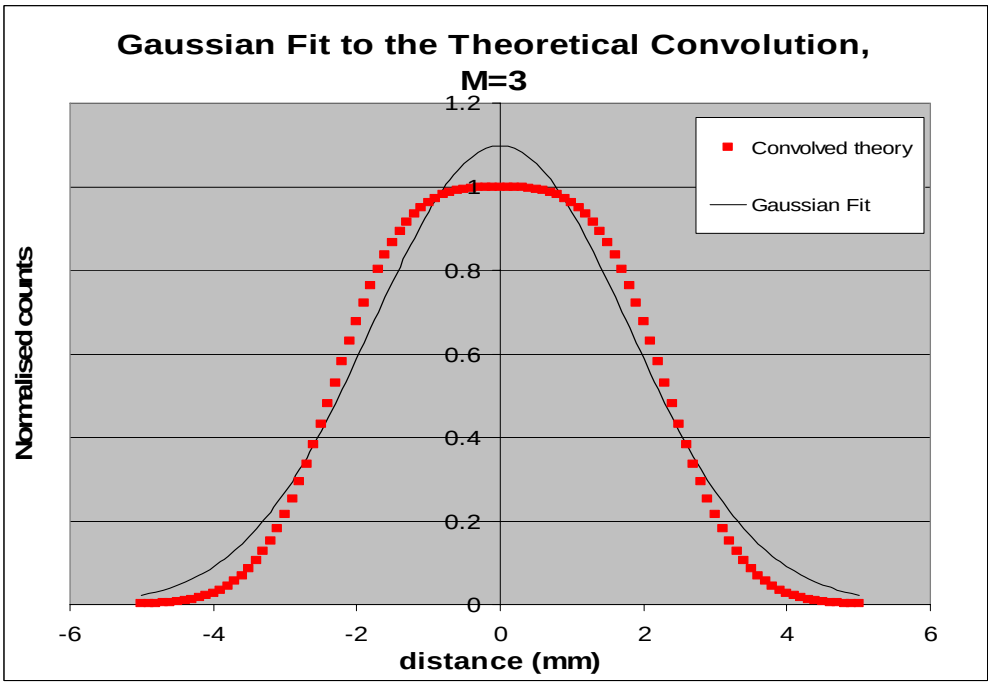

Fig. 3.3.*Gaussian fit to the convolution between the 1-dimensional pinhole PRF and the planar detector LSF.*

Pinhole sensitivity was measured using a point source of ^{99m}Tc. The point source was translated in a direction perpendicular to the pinhole axis, thereby changing θ and the source-to-pinhole distance. At each location the total number of detected counts per unit time, corrected for radioactive decay, was recorded.

A schematic of the experimental setup used for characterizing the off-axis spatial resolution is shown in Fig. 3.4. Two different detectors were tested, one planar and one curved. The planar detector, built at the Thomas Jefferson National Accelerator Facility (TJNAF), contains a pixelated array of NaI(Tl) crystals with 1.8 mm center to center spacing, and 6 mm crystal thickness (~80% absorption at 140 keV). The crystals are read out by a 5 inch diameter R3581 position sensitive photomultiplier tube (PSPMT) from Hamamatsu. The curved detector, built by RayVisions, Inc., Yorktown, VA, contains three detector modules. Each module consists of a 9 x 9 array of CsI(Na) crystals, coupled via optical fibers to Hamamatsu R5900-M64 PSPMTs. The crystals have 2 mm center-to-center separation, and are 3 mm thick (~70% absorption at 140 keV). The three modules are oriented so that the crystal arrays are in contact along one edge, thereby forming a 9 x 21 pixel detector. Each module of a detector is angled so that its center normal passes through the center of the pinhole aperture. Two such 3-module detectors were constructed.

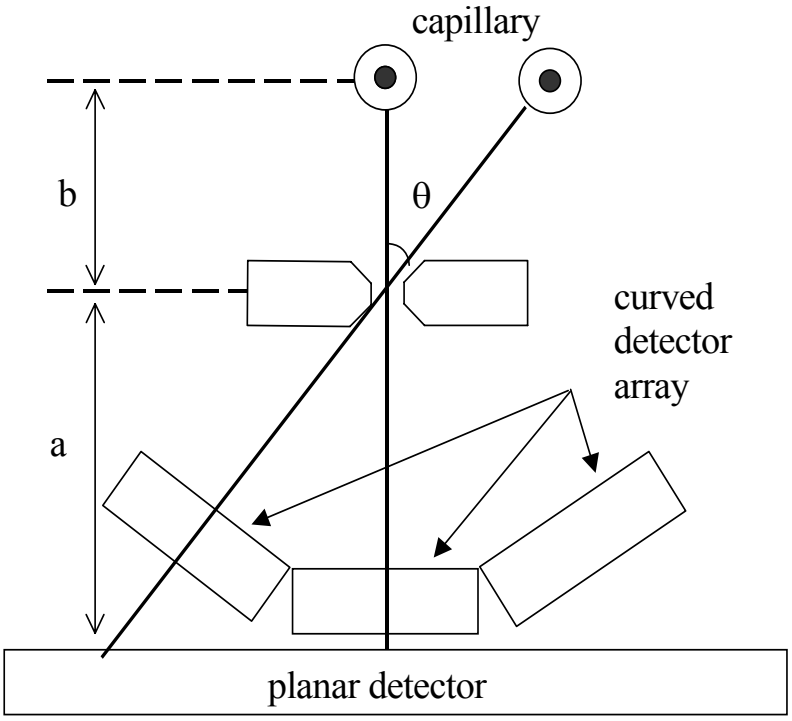

Fig. 3.4.*Schematic of the experimental setup used to compare spatial resolution using the planar and curved detectors. For simplicity, both the planar and curved detectors are shown, although their spatial resolution was measured separately. Two capillary positions are shown; one on the pinhole axis and one at an angle θ off the axis*

All intrinsic detector resolutions were measured using a 3 mm thick tungsten slit placed in direct contact with the detector surface. A point source of Tc-99m placed directly above the slit at a distance of ~ 1 m was used to produce nearly normally incident gamma rays.

For the study comparing the angular dependence of the system spatial resolution of cameras using planar and curved detectors, the pinhole collimator was a tungsten alloy channel-type, with d = 1 mm and $\alpha = 90°$. The pinhole channel length was 1 mm, and the linear attenuation coefficient of the tungsten/nickel/copper material was 38.5 cm^{-1} at 140

keV. Resolution and efficiency measurements were also made using pinhole collimators with a variety of smaller pinhole angles, α. These pinholes, manufactured by Mikro Systems, Inc., Charlottesville, VA, are made from a tungsten-polymer composite material, with a linear attenuation coefficient of 20.7 cm^{-1} at 140 keV. Knife edge pinholes with 40, 80, 100 and 120 degree pinhole angles and 1 and 1.5 mm pinhole sizes were tested. The lower linear attenuation coefficient of the tungsten-polymer composite material relative to that of the tungsten alloy is balanced by the fact that Mikro Systems can fabricate composite collimators with shapes and sizes either impossible or prohibitively expensive to machine.

For spatial resolution measurements, narrow bore capillaries (0.71 mm inner diameter) were filled with ^{99m}Tc solution to simulate line sources. For the comparison between the planar and curved detectors, on-axis magnification factors of 2.0 and 1.3 were used for the planar and curved detectors, respectively. Different magnification factors were used because the housing of the curved detectors placed an upper limit on the pinhole-to-detector distance and a lower limit on the source-to-pinhole distance. Also, the two detectors had different intrinsic spatial resolutions for normally incident gamma rays (2.0 mm FWHM for the planar detector and 2.2 mm FWHM for the curved detector). These two factors led to slightly different system spatial resolutions for the two detectors at $\theta = 0$.

To measure the off-axis system resolution, the capillaries were translated perpendicularly to the pinhole axis, and at each capillary position an image of the capillary was obtained. Under these conditions, the capillary-to-pinhole distance

increases with increasing θ. For the planar detector the magnification factor, M is constant, while for the curved detector it decreases with increasing θ.

Since the detectors in this study use pixelated arrays of crystals, the measured line spread function (LSF) is not strictly speaking stationary, but varies slightly depending on whether it is measured at the center of a crystal (best resolution) or in between crystals (worst resolution). For this reason, we have used an approach that results in an averaged line spread function. Capillaries were slightly slanted (e.g. ~1 column per nine rows of crystals) relative to the gamma camera crystal matrix. This has the effect of projecting the line source input at different locations with respect to the crystal centers. By making the reasonable assumption that rows in crystal array are identical, line spread functions obtained from different rows can be averaged, to obtain the spatially averaged LSF. Images were analyzed using a routine written in IDL (Interactive Data Language, Research Systems, Inc., Boulder CO). For the relatively small magnification factors tested here, the LSF is somewhat coarsely sampled by the detector pixels. Therefore, to obtain a more precise estimation of the FWHM of the LSF, a Gaussian function was fitted to each row of the image, and the FWHM of the Gaussian fit was recorded. Averaging over all rows and dividing by the magnification factor yields the average FWHM resolution at the capillary.

Although the shape of the measured system LSF is a function of both the magnification factor (M) and the source location (θ), for the range of M and θ considered here, the system LSF was well fitted by a Gaussian function. Figs. 3.5 and 3.6 are plots of the measured system LSF for the smallest (M=1.5) and largest (M=3.0) magnification

factors used. In each plot, a Gaussian function is shown fitted to the measured data. The plots show that Gaussian functions are a reasonable fit to the coarsely sampled LSF.

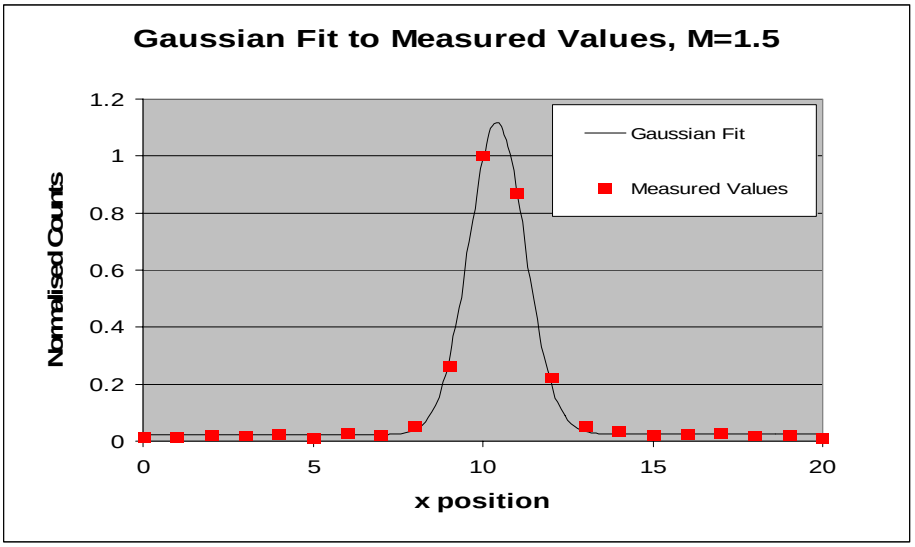

Fig.3.5.*Gaussian fit to the measured system LSF for $\theta = 0$. The magnification factor is 1.5*

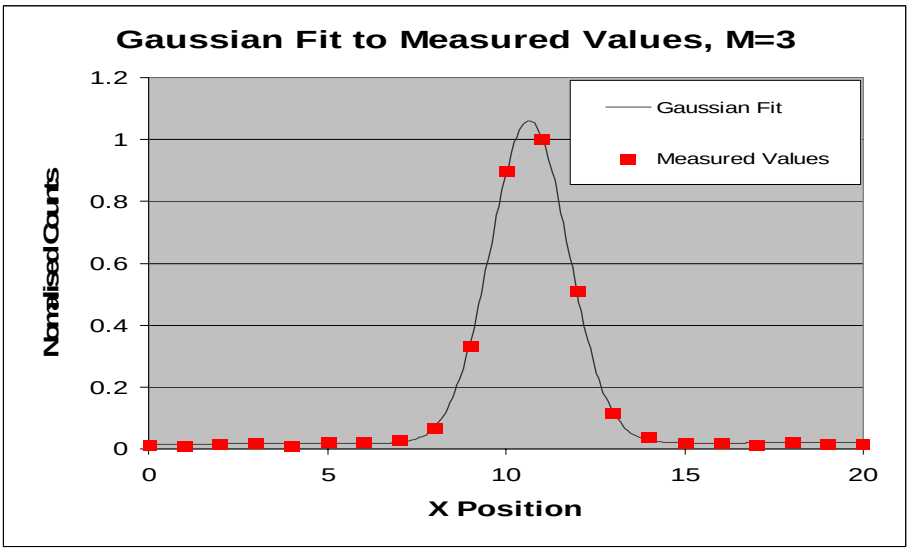

Fig. 3.6.*Gaussian fit to the measured system LSF for $\theta = 0$. The magnification factor is 3.0.*

Fig. 3.7 compares the θ-dependence of the efficiencies of two knife edge W-polymer pinholes; one with $\alpha = 40°$, d = 1.5 mm, and one with $\alpha = 100°$, d = 1.0 mm.

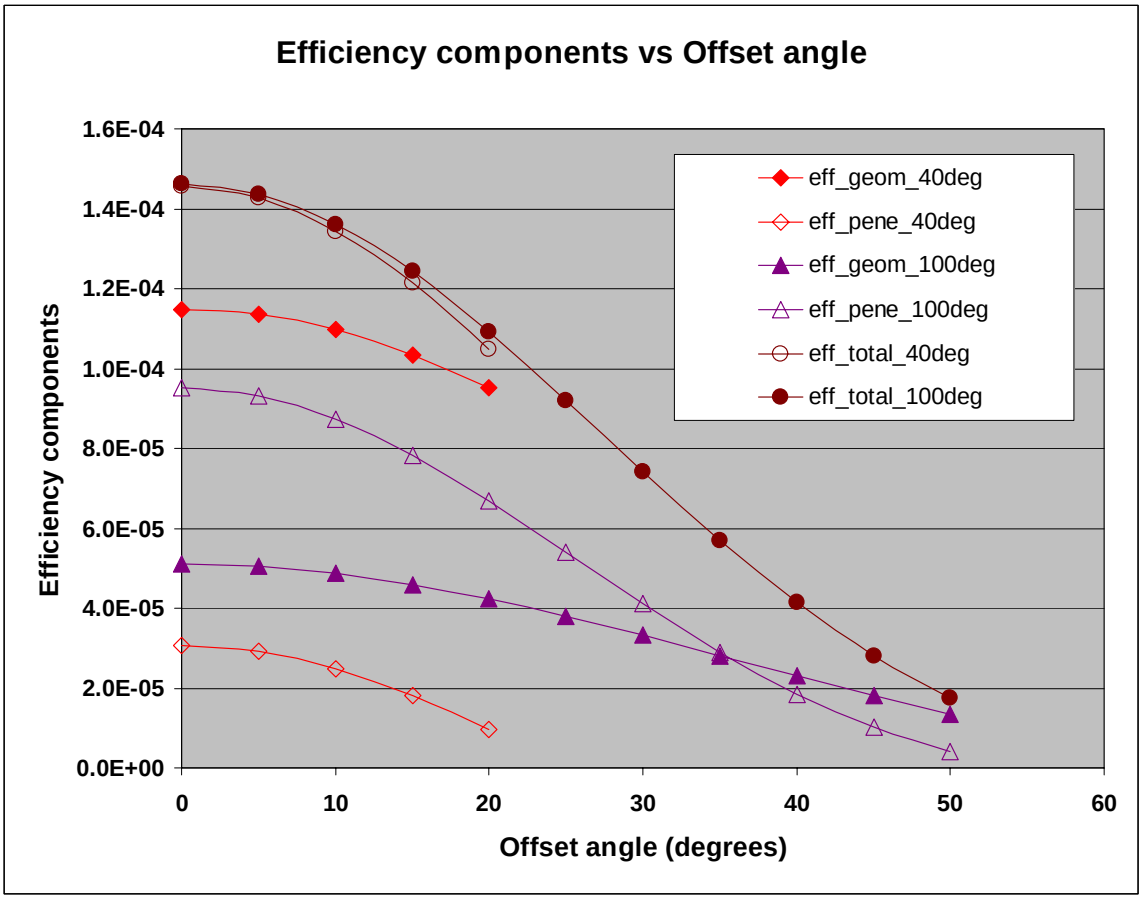

Fig.3.7. *Calculated geometric and penetration components of the total efficiency for W-polymer pinholes with pinhole angles of 40 and 100 degrees.*

The diameters of the two pinholes were chosen so that their effective diameters, d_e were nearly identical (d_e = 1.7 mm) at θ = 0°, and thus their on-axis efficiencies could be expected to be approximately equal. In addition, the two pinholes had similar on-axis spatial resolution (the measured FWHM system spatial resolution at θ = 0° was 1.9 mm and 2.1 mm for the 40° and 100° pinholes, respectively). For the efficiencies plotted in

Fig. 3.7, the value of b used was 35 mm. The theoretical geometric, penetration, and total efficiencies, calculated using (3.1) – (3.3), are also shown.

The plot demonstrates that for the small angle pinhole ($\alpha = 40°$), the geometric component dominates the penetration component over the entire FOV of the pinhole, whereas for the large angle pinhole ($\alpha = 100°$), the penetration component dominates the geometric component for $\theta \leq 30°$. In spite of this very different behavior of the two components, the total efficiency of the two pinholes is quite similar over their common FOV. Fig. 3.8 shows the measured total efficiency for these two types of pinholes using

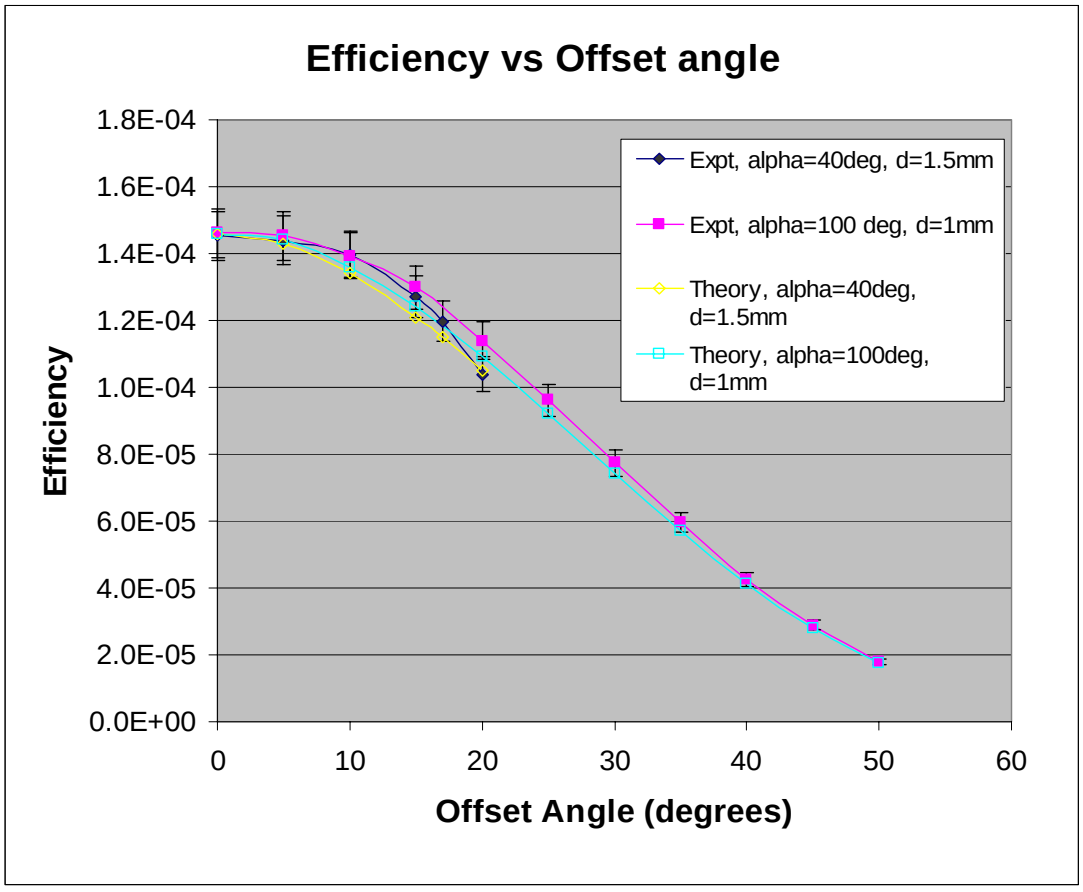

Fig.3.8. *Measured and theoretical angular dependence of the pinhole efficiency for 40 and 100 degree knife edge W-polymer pinholes*

b value of 35 mm, along with the theoretical total efficiency shown in Fig. 3.7. Good overall agreement between theory and measurement is demonstrated.

To better understand the effect of differing pinhole angles, α, on the overall efficiency, we computed the average efficiency of pinholes with α = 40, 60, 80, 100 and 120 degrees. In order to compare pinholes yielding similar spatial resolution, the pinhole diameter d was chosen so that the calculated on-axis value of d_e was the same for all values of α. Table I lists the values of d chosen for each α to give a common value of d_e = 1.6 mm. The d_e values were calculated using (3.7), with $\theta = 0°$.

α	**d**
40	1.41
60	1.29
80	1.14
100	.91
120	0.5

Table 3.1. *Values of d that result in a common value of de = 1.6 mm, for pinholes with different pinhole angle, α.*

Fig. 3.9 shows the theoretical average efficiency as a function of the pinhole angle α, for b = 35 mm. Average efficiency is shown both in the angular interval from $\theta = 0$ to $+\alpha/2$ (i.e. the entire pinhole FOV), and for the interval from $\theta = 0°$ to $+20°$ (the common FOV of all pinholes). Although the efficiency averaged over the entire pinhole FOV is substantially less for large α, averaged over the common FOV from $\theta = 0°$ to $+20°$ the efficiency is essentially independent of α.

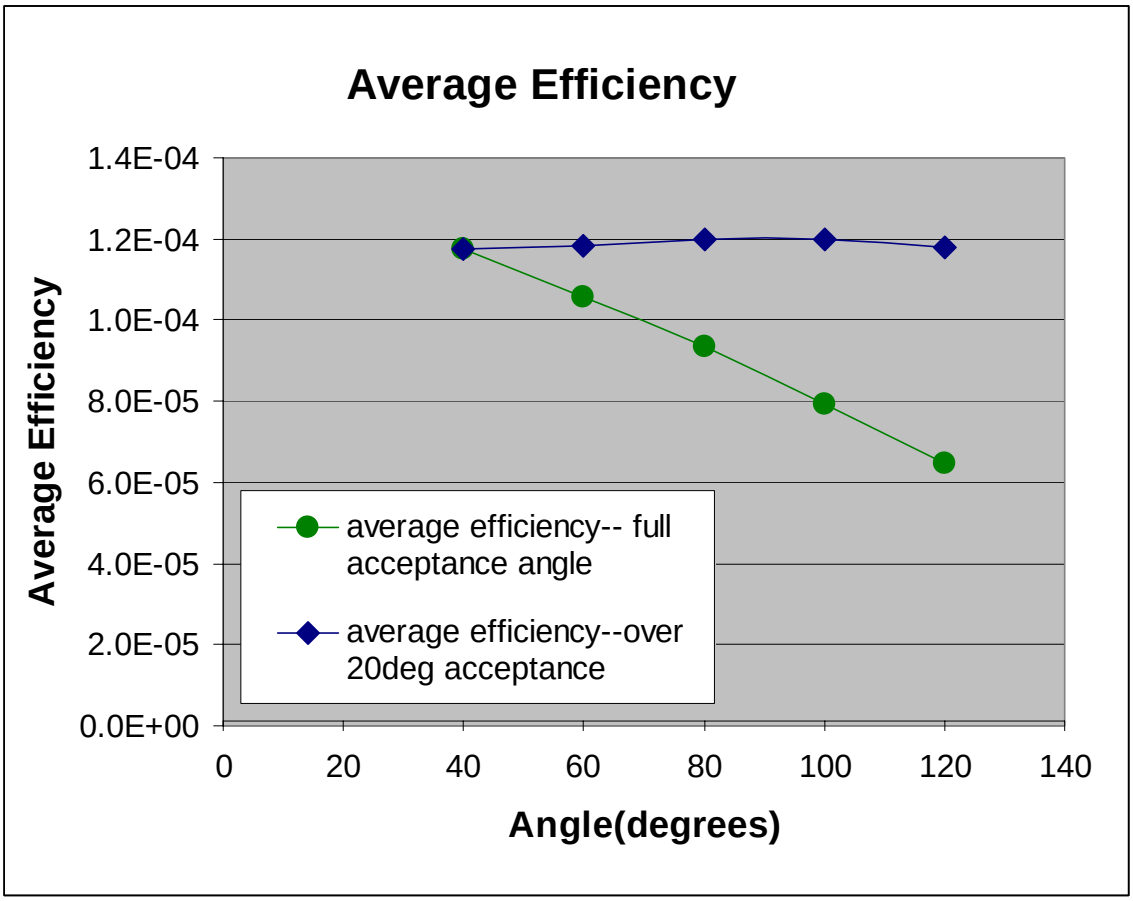

Fig.3.9.*Theoretical average efficiency plotted as a function of the pinhole opening angle*

3.1.3 System Spatial Resolution

Fig. 3.10 compares the measured θ-dependence of the system resolution using the planar detector with that using the curved detector with the same collimator. Because of constraints imposed by the housing of the curved detector, the maximum θ value that could be tested was 40°. As can be seen from the graph, the spatial resolution using the curved array exhibits a monotonic decrease with increasing θ. On the other hand, the

resolution using the planar detector increases with increasing θ starting at θ ~ 25°. The difference in the resolutions of the two cameras exceeds experimental error for θ ≥ 30°.

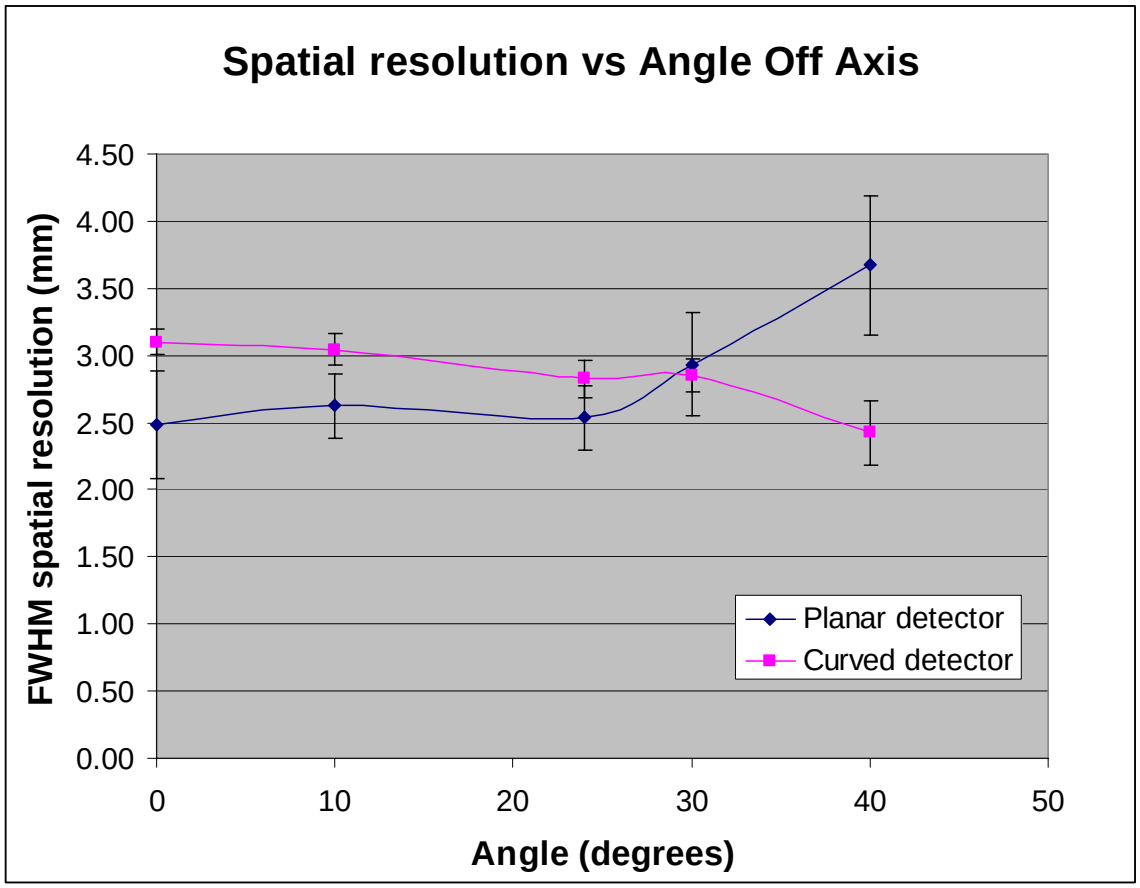

Fig.3.10.*Angular dependence of the FWHM system resolution of the planar and curved detectors*.

In both cases a 1 mm diameter 90° tungsten alloy channel collimator was used. Fig. 3.11 shows the angular dependence of the system spatial resolution using a planar detector and a 1 mm 40° W-polymer knife edge collimator.

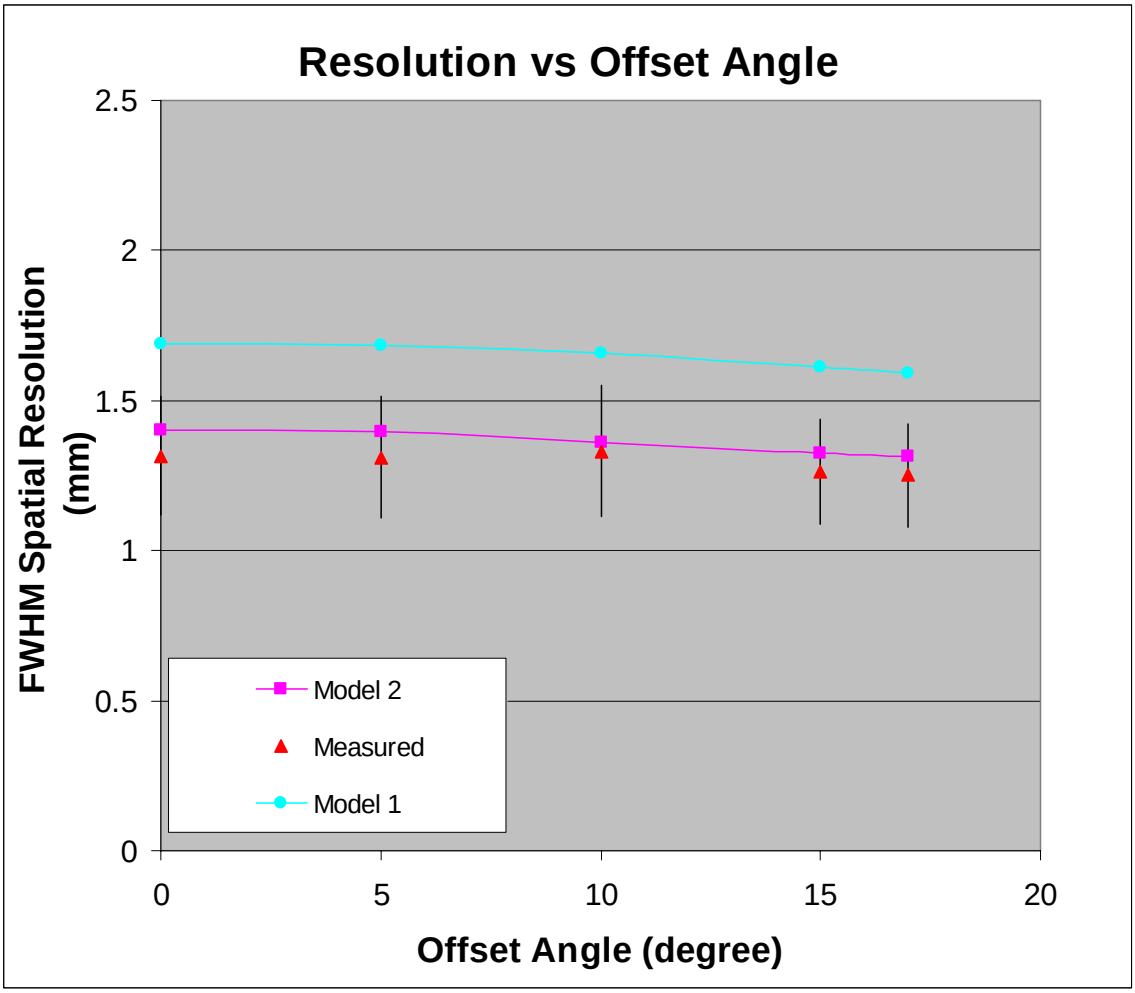

Fig.3.11.*Angular dependence of the FWHM system spatial resolution using the 1mm 40 degree W-polymer knife edge pinhole*

The measured intrinsic resolution of the planar detector, averaged over the detector surface, is 1.8 ± 0.2 mm FWHM. Also shown is the theoretical spatial resolution calculated using Model 1 and Model 2. Fig. 3.12 shows the measured system resolution versus the magnification factor, M, for the same tungsten-polymer knife-edge collimator.

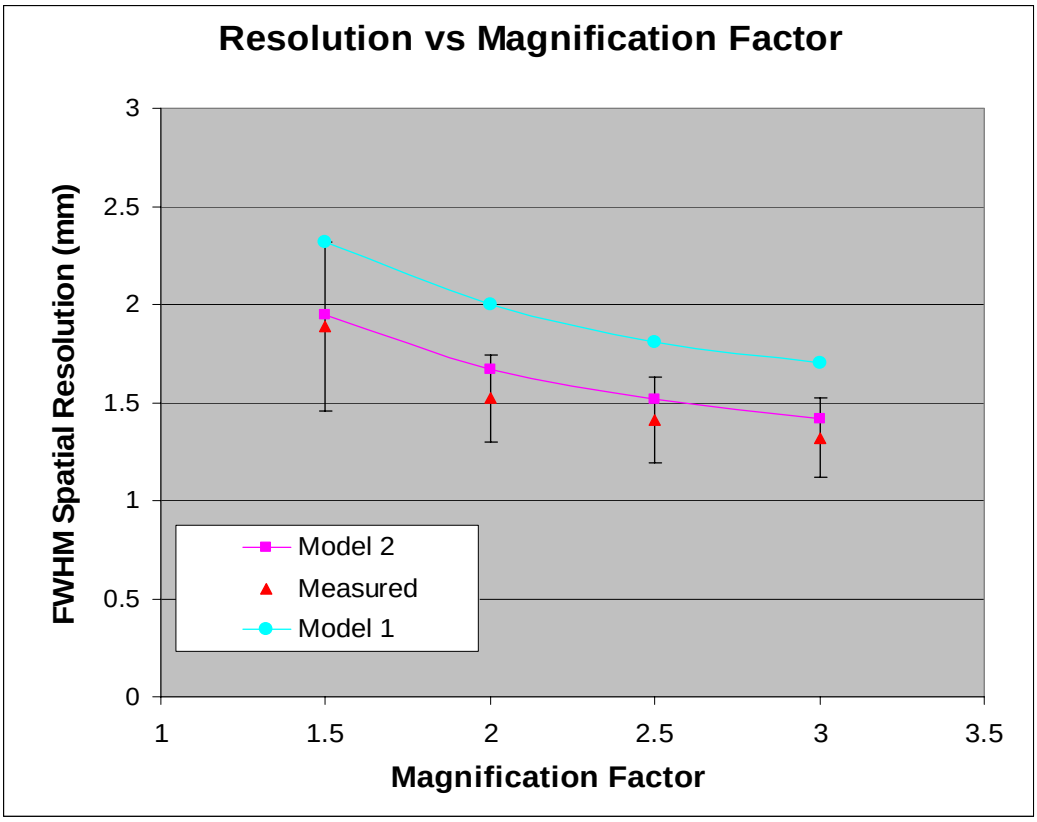

Fig.3.12.*Measured and theoretical variation with magnification factor of the FWHM system spatial resolution for W-polymer knife-edge pinholes*

The measurements in Fig. 3.12 were made with the source on the pinhole axis ($\theta = 0°$). The theoretical resolution calculated using Models 1 and 2 are also shown for comparison.

3.1.4 Conclusions of pinhole characterization study

Primary goals of the experiments were a) to examine the angular dependence of the sensitivity of pinhole collimators fabricated using a tungsten-polymer composite with a variety of pinhole angles, and b) to determine the effect of depth-of-interaction blur on the spatial resolution of pinhole gamma cameras using planar detectors.

The measured θ-dependence of the overall pinhole efficiency agrees well with the theory of Metzler et al. for pinhole collimators of both large and small pinhole angle. However, as suggested in Fig. 3.7, the physical phenomena dominating the functional form of $S_{total}(\theta)$ are quite different in the two cases. For the pinhole material and gamma ray energy considered here, the efficiency of small angle pinholes is determined primarily by the geometric component, and that of large angle pinholes is determined largely by penetration. In spite of this difference, the angular dependence of the overall efficiency of large and small angle pinholes is remarkably similar for pinholes yielding similar spatial resolution.

Results show that for ^{99m}Tc detected by 6 mm NaI(Tl), the DOI effect noticeably broadens the LSF of the planar gamma camera for sources located more than approximately 30° away from the pinhole axis, in spite of the improved pinhole PSF (Fig. 3.10). Not surprisingly, the same experiment utilizing a curved array of detectors yielded reduction in the overall LSF with increasing θ, which can be attributed to the improvement of the pinhole PSF in the absence of the DOI effect as the source was moved off axis. This suggests that one possible approach to maintaining high spatial resolution over the entire FOV of large angle pinholes is to use curved detectors. For all detector formats, the price of the improvement in the pinhole PSF with increasing θ is a decrease in efficiency. The use of a curved detector would at least compensate this lowered efficiency at large θ with improved spatial resolution.

As shown in Figs. 3.11 and 3.12, over the range of θ (0° to 18°) and range of M (1.5 to 3.0) tested, the FWHM system resolution obtained by convoluting the PRF of (3.8) with a Gaussian function representing the intrinsic detector LSF (Model 2) shows good

agreement with the measured values. However, the FWHM spatial resolution predicted by summing the effective pinhole diameter in quadrature with the intrinsic detector resolution (Model 1) is consistently higher than measured values. Fig. 3.11 suggests that the measured resolution exhibits slightly less decrease with increasing θ than do the theoretical resolutions. However, this may be because DOI effects are not included in either Model 1 or Model 2.

A pinhole SPECT system useful for small animal imaging must exhibit both high spatial resolution and adequate detection efficiency. Since gamma ray obliquity increases and pinhole efficiency decreases with increasing distance between the source and the pinhole axis, portions of the animal positioned away from the pinhole axis may not be well imaged. A logical choice to optimize both average spatial resolution and average efficiency within the pinhole FOV is to utilize small angle pinholes.

3.2 Compact gamma imaging detectors

Gamma detector is a centerpiece of any emission tomography system. Flaws in the detector may rarely be overcome even by optimal design of other scanner components. Small-animal imaging imposes additional requirements due to the scale involved. As was already mentioned high spatial resolution is a must for a dedicated small-animal imager. Since all the reconstruction algorithms rely on assumption that detected particles travel in straight paths, scattered radiation may introduce additional uncertainties in gamma event localization. Small animals can not be injected with high volume of liquids due to their low blood volume, so the amount of administered radioisotope can be limited. Although

most of the efficiency loss takes place at the image formation stage, additional signal losses need to be avoided by utilizing high efficiency detectors. Detector response uniformity also plays an important role. Non-uniform detector responses can sometimes be corrected by post-processing algorithms, but that excessive data manipulation often results in image quality degradation. To avoid all those obstacles a thorough characterization of gamma cameras should be carried out prior to system integration. Our close collaboration with scientists from Jefferson Lab gave us an opportunity to integrate very high quality gamma cameras in our scanner. This chapter provides detailed insights of the detectors' operation and reports on methods and results of gamma camera characterization.

3.2.1 Internal detector structure

Dedicated small animal gamma cameras were implemented by Rayvisions, Inc (Yorktown, VA). The technology was developed at Thomas Jefferson National Accelerator Facility (Newport News, VA) by the TJNAF Detector Group. The detectors are based on Hamamatsu Photonics KK (Hamamatsu City, Japan) H 8500-series position sensitive flat panel square photomultiplier tubes (PMT). Photo tubes have 1.5 mm thick borosilicate entrance glass window with bialkali photocathode. Each PMT encloses 12 amplification stages with 64 anode pads, arranged in an 8 by 8 square array. PMT operating voltages are typically 700 to 1100 Volts with the typical gain of $5x10^5$ to 10^7. PMT measures to be 52 mm x 52 mm x 28 mm with an active imaging area of 49 mm x 49 mm. Due to square shape of PMTs, tubes can be tiled together to achieve larger area

detector. Our detectors employ a 2 by 2 tiled array for a total imaging area of approximately 100 mm x 100 mm.

Cross section of a detector head is shown in Fig. 3.13. Four PMTs, arranged in a 2 by 2 matrix, are coupled to a pixelated NaI (Tl) scintillating crystal array (Saint Gobain Crystals, Newbury, OH) using Visilox-V-788 optical grease compound. The crystal array is comprised of 1.3 mm x 1.3 mm x 6 mm individual crystals separated by a 0.2 mm layer of light-opaque epoxy mixed with aluminum powder which effectively yields an imaging matrix of approximately 100 mm × 100 mm with a detector element size of 1.5 mm. Because NaI is a very hygroscopic material, each array is hermetically sealed to avoid crystal's deterioration.

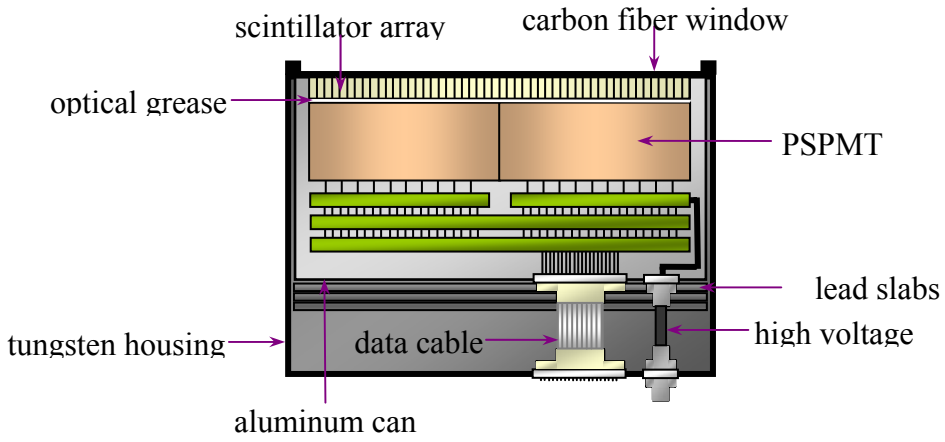

Fig.3.13. *Schematic of a gamma detector head*

All PMTs are connected to the common electronic circuitry, which will be discussed later. Fig. 3.14 exhibits photograph of a PMT array and a crystal matrix.

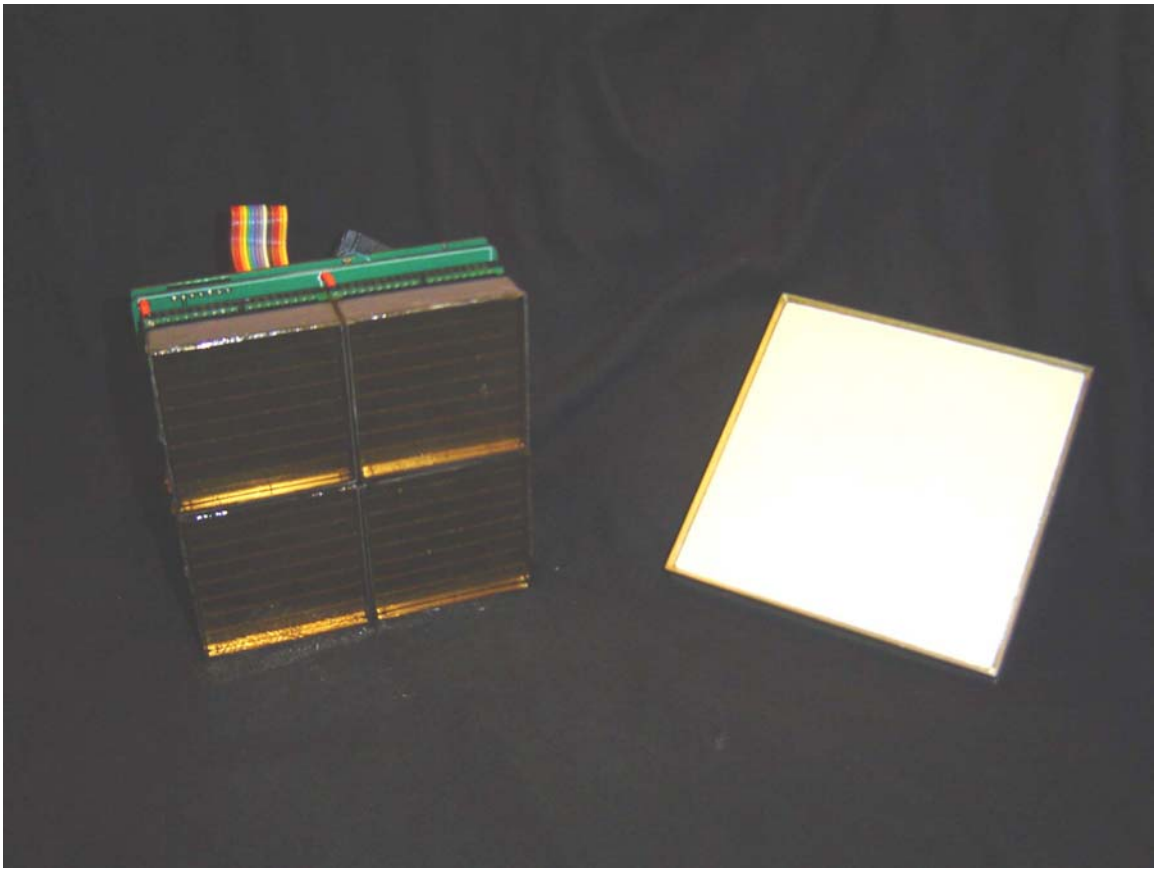

Fig.3.14.*PMT assembly and NaI crystal array*

PMTs-crystal array assembly is packed into an aluminum can to prevent any light leaks. Gamma ray entrance surface of the can is made out of carbon-fiber to reduce the attenuation of the incoming radiation. The aluminum box resides in a radiation shielding container made out of tungsten alloy. The tungsten box incorporates steps on two opposing side surfaces to permit mounting of the detector on the gantry. Approximately 2 mm wide ridges along the width of the box on the opposite sides near the top surface act as guiding rails for the collimators to slide on. High voltage and 15-pin electronic connectors are rigidly attached to the bottom surface of the shielding box.

3.2.2 Detector internal electronics

Detector internal electronics consists of three major components: high voltage divider, signal preamplifiers with gain correction resistor matrix, and charge division readout circuitry. High voltage divider board is supplied by the tube manufacturer. It is a standard resistive divider circuit with 1:1 voltage ratio between adjacent dynodes and filtering capacitors installed at the dynode stages 10 through 12. Manufacturer also supplies a gain map of each PMT, a relative measurement of the charge output as a function of the location of the incoming light on the photocathode. On a typical PMT a gain variation can be as large as a factor of 5 and that includes non-uniformity of the quantum efficiency of the photocathode as well as variations in dynode structure amplification. TJNAF developed a novel technique to equalize charge output from different anodes [7]. This technique utilizes a matrix of adjustable resistors. The signal from each anode pad is attenuated by a resistor with appropriately chosen value. Equalized signals could potentially be digitized individually, but that would require 64 readout channels per PMT and 256 channels per detector head. In order to decrease the amount of readout channels, equalized charge outputs are resistively interconnected in X and Y directions, resulting in 16 output lines in each direction. Output signals are then amplified and fed into subtractive resistive readout [8]. Diagram of the subtractive resistive readout is shown in Fig. 3.15.

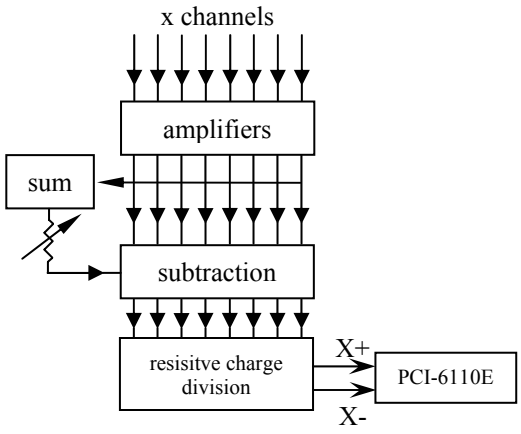

Fig.3.15. *Schematic of subtractive-resistive read-out*

Incoming signals are split. Half of each signal goes to an inverting summing circuit. A portion of the inverted sum, set by a potentiometer, is then sent to individual summing amplifiers, which add it to the other half of original signals. Any resulting signal below ground is clipped. The signals are then combined by a charge division resistive chain to produce two output signals in each direction, reducing total number of readout channels to 4. A summed signal from one coordinate is employed as an additional output to be used later as a trigger signal. All the output signals are combined into a single 15-pin data cable.

3.2.3 External electronics and controls

Outputs of each detector head are connected to a common control box. The control box supplies common high voltage to all four detector heads, low voltage for the amplifying circuits and contains multiplexing signal processing electronics as well as a timer ramp to allow time-stamping of the incoming events. The signal outputs from each

detector are connected to analog switches, which are held normally open. Summed signal from one coordinate of each detector is fed into a constant-fraction discriminator to determine which camera detected a photon. Then the switches responsible for the other three cameras are turned off, allowing only the data signals from the triggered detector to be transmitted for digitization. After digitization is complete all the switches are turned on again. This method allows avoiding additional noise in the data lines associated with opening of analog switches. Signals are digitized to 11 bits by a National Instruments (Austin, TX) model PCI-6110 4-channel analog-to-digital converter. Another ADC card is installed on the data acquisition computer. Two of its channels are used for the detector number signal and event time stamping. The remaining two channels are reserved for future system expansion. The data processing routine and image displaying interface are written in the KMAX language (Sparrow Corp, Port Orange, FL). Data acquisition software is able to collect data in list mode, when all the parameters of every detected event are written to a hard drive and processed off-line, and in online mode, which allows for the images to be viewed as they are being acquired. Data processing and detectors calibration are discussed in the next subchapter.

3.2.4 Data processing and detector calibration

Outputs of six ADC channels are processed according to the following algorithm. Sum of all the signals is histogrammed into a 2048 channels long histogram called Raw Energy. A cut is placed on this histogram to separate true events from the noise. Anger-type arithmetic is then performed on each coordinate value inside the cut:

$$X(Y) = \frac{X(Y)^{+} - X(Y)^{-}}{X(Y)^{+} + X(Y)^{-}} \qquad (3.1)$$

Resulting X and Y values are histogrammed into an 1100 x 1100 two-dimensional histogram called Image Raw. From X and Y values the crystal location is identified according to the crystal look-up table. After crystal number identification, the program retrieves an energy correction factor from the energy look-up table and histograms the corrected energy value into 10-bit histogram called Normalized Energy. An acceptance window is applied to this histogram in order to select only the events with certain energy. One may apply more than one energy cut, which can be useful in multi-isotope experiments. If an event falls within the acceptance window, a corresponding pixel count in the histogram called Image Full is incremented by one. Image Full is a two dimensional histogram with the number of bins corresponding to the number of identified crystals. Finally, a flat field correction, or a flood, is applied to Image Full to create a Corrected Image. Corrected Image is then saved for image reconstruction.

Calibration procedures are implemented to create look-up tables mentioned above. Calibration starts with the detector being illuminated by a uniform flux of mono-energetic radiation. We usually employ a radioactive point source placed about 1.5 m above the detector surface. Image Raw histogram is acquired at this stage. This histogram represents spatial distribution of the detected radiation without any reference to the

physical detector element. A sample Image Raw is presented in Fig. 3.16.

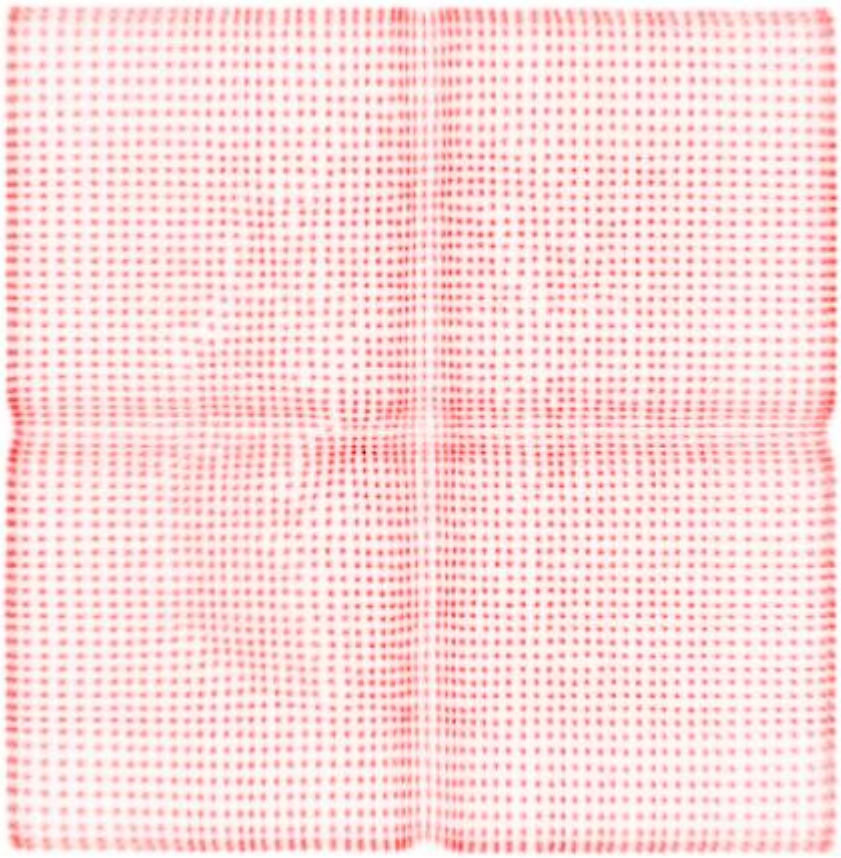

Fig. 3.16.*Uncorrected distribution of detected photons, "Image Raw"*

As one can observe, detected events are highly clustered, allowing for the reference to be established. Next calibration step is to create a map of the crystals, a two dimensional look-up table that identifies the crystal responsible for photon absorption. Crystal mapping is a three stage process. In the first stage, vertical and horizontal lines are drawn through the centers of every cluster on the Image Raw. Then a program finds valleys, low counts regions, in between the clusters. In the last stage, the crystal map is created, a look-up table containing a crystal number for every point inside the region

confined by the valley lines. Points along the lines are assigned higher numbers and the crystal association of the event located on the line is decided randomly between two adjacent crystals. A crystal look-up table is saved on a hard drive. Next step of the calibration is an energy correction to compensate for individual crystal light output non-uniformity and remaining PMT non-uniformities. Since all the crystals were identified, energy spectra of each of them can be obtained. KMAX software has a maximum histogram length limitation of 32768 channels, so 16 histograms were created in order to accommodate the spectra of 4096 (64 x 64) detector elements. Each spectrum is confined to 128 histogram channels by applying appropriate compression factor to the original 11 bit value. After individual spectra were acquired, the peak value of each is identified and scaled such that the distribution peak would appear channel 512 of a 10-bit long histogram. The scaling values are stored in one-dimensional array called energy look-up table. Energy calibration is obviously an isotope dependent procedure and is performed for every new isotope to be used. Finally, after both position and energy calibrations were performed, the detector is again illuminated with a uniform flux and high statistics (approximately 10,000 counts per pixel) Image Full is obtained and saved. This image is used for flat fielding correction as defined by equation (2.1).

3.2.5 Detectors imaging characteristics

Intrinsic spatial resolution, energy resolution, intrinsic sensitivity, and detector response uniformity for each detector were measured in order to evaluate imaging characteristics. Methods reported here were successfully applied to gamma detectors performance evaluations before [9]. The intrinsic spatial resolution of a detector was

measured using a Tc-99m point source and an ~ 0.1mm wide slit made of two 6mm thick tungsten plates. In order to obtain a spatially averaged line spread function (LSF), the slit was oriented at a small angle with respect to the crystal matrix. The slanted orientation of the slit has the effect of projecting the line source input onto different locations with respect to the crystal centers for different crystal rows. A Gaussian function was fitted to each row in the image, and the full width at half maximum (FWHM) was computed. The FWHM of the spatially averaged LSF was obtained by averaging the resulting FWHMs. The resulting FWHM was multiplied by the pixel size of the detector and reported as detector intrinsic spatial resolution. The experiment was repeated three times for different locations of the slit on the detector imaging area. Results of the evaluation of all four detectors' spatial resolution are given in Table 3.2.

	Spatial resolution left side (mm)	Spatial resolution center (mm)	Spatial resolution right side (mm)
Detector 1	1.72	1.62	1.64
Detector 2	1.65	1.73	1.68
Detector 3	1.72	1.69	1.68
Detector 4	1.81	2.36	1.97

Table 3.2.*Spatial resolutions detectors 1, 2 and 3.*

(Detector 4 yielded the worst intrinsic spatial resolution of the bunch. Upon close inspection of the detector 4 crystal array, a significant yellowing of the crystals was noticed, most probably due to poor air sealing. A new array was ordered and we are expecting it to arrive at UVa around mid-March. Further along, detector 4 will be omitted

from the general discussion.). Energy spectra were obtained by placing a Tc-99m point source above the detector surface. The FWHM of the Gaussian function fit of the photopeak, normalized by the peak position, is reported as an average energy resolution. Sample energy spectrum is shown in Fig.3.17.

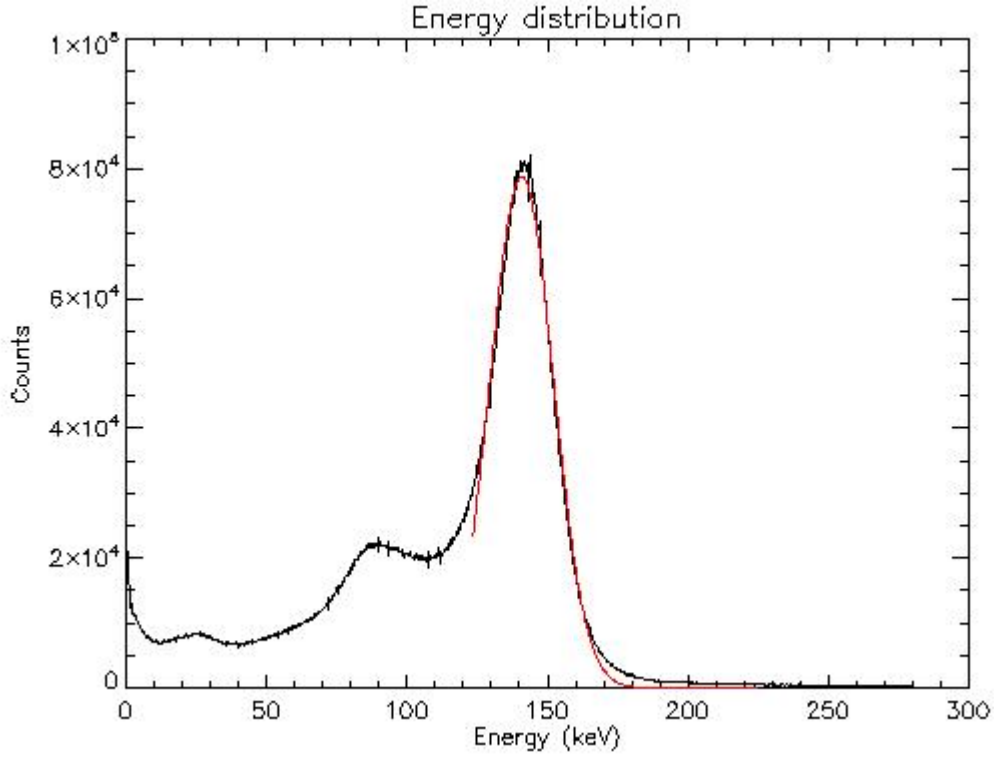

Fig. 3.17.*Energy spectrum of detector 3 is shown. Gauss fit to the distribution is shown in red.*

Intrinsic detection efficiency was measured by taking timed images of a point source of Tc-99m of known activity located known distance from a detector surface. Energy acceptance window was set at -7%/+27% of the photopeak location, which is a typical value for imaging with Tc-99m. Predicted number of photons to be incident on a detector surface was calculated. In order to do this, a fraction of solid angle subtended by a detector was calculated and multiplied by the source activity. A total number of

predicted gamma events was obtained by multiplying the result by the data acquisition time. Percent ratio between the detected and predicted counts is reported as detection efficiency. The uniformity of the detectors was evaluated by evenly illuminating the surface with 140 keV gammas from a point source located about 1.5m above the detector surface. The mean value and standard deviation of the pixel counts over the entire detector and in the central 75% of the image was calculated. The ratio between the standard deviation and the mean pixel count is reported as the detector response non-uniformity. Table 3.3 summarizes results of gamma detectors evaluations.

	Energy resolution at 140 keV (%)	Detection efficiency (%)	Overall response non-uniformity (%)	Central 75 % non-uniformity (%)
Detector 1	19.4	47.7	32.1	8.4
Detector 2	21.2	47.7	34.8	9.3
Detector 3	18.5	47.8	27.1	7.5

Table 3.3.*Results of characterization detectors 1, 2 and 3*

No significant variations from the expected parameters were observed during the testing. Detectors pixel pitch of 1.5 mm is the main resolution limiting feature. Slight widening of the line spread is inevitable for the detectors, which utilize optical grease coupling between PMTs and scintillators. This widening is attributed to lateral spread of visible photons between the exit window of a scintillator array and a photocathode of PSPMT. Energy resolution of about 20% was expected from testing similar detectors [9]. Several factors contribute to detection efficiency. Aluminum entrance window of the crystal array allows for transmission of about 98 % of incoming photons. Crystal array

has active elements packing ratio of 77%, while NaI scintillator itself absorbs approximately 80 % of 140 keV photons. These factors combined account for ~ 60 % of detection efficiency. The rest of the lost gamma events are rejected by the energy acceptance window. Approximately 9 % of non-uniformity of detector response in the central 75 % of the imaging area was shown to be corrected by flat-fielding process [9]. Overall, three out of four detectors were found to be well performing. Detector 4 will become operational in the very near future.

3.3 Half-cone data acquisition geometry

Investigation of imaging properties of pinhole collimators concluded that the most straightforward solution to spatial resolution degradation due to DOI and a pinhole sensitivity fall-off is to reduce pinhole's acceptance angle. This simple approach has to address its own problem, which is more serious than DOI and sensitivity reduction. The problem is that for a fixed field of view (FOV) of the scanner, or in other words for a fixed size of the animal to be imaged, the distance between the pinhole and the animal is inversely proportional to sine of half of the pinhole acceptance angle. So to maintain the same field of view, camera has to be moved back, which will cause reduction in both sensitivity and resolution. Moreover, this reduction will affect every point inside the field of view, not only off-axis points. In general it is a good idea to keep pinhole as close to the animal as filed of view permits. That would have been a strong argument for use of large angle pinhole, but as was showed the larger the angle the more pronounced the DOI effect is and sensitivity drops off more rapidly. We propose to use a novel approach to minimizing source to pinhole distance, keeping the acceptance angle small. Fig. 3.18

shows a schematic of proposed geometry. In what we call “half-cone” acquisition geometry gamma camera equipped with small angle pinhole collimator is overlooking only half of the field of view at any given angular position. Gamma camera is tilted with respect to the axis or rotation (AOR) of the scanner in such a way that the AOR is tangential to the pinhole acceptance cone. Such reduction in the field of view allows decreasing source to pinhole distance thus maximizing spatial resolution. Of course system sensitivity will be much lower, but it can be recovered by positioning one more camera exactly 180 degrees opposite to the first one. Now the whole field of view is sampled by a pair of cameras, with each camera located as close to the object as pinhole angle permits.

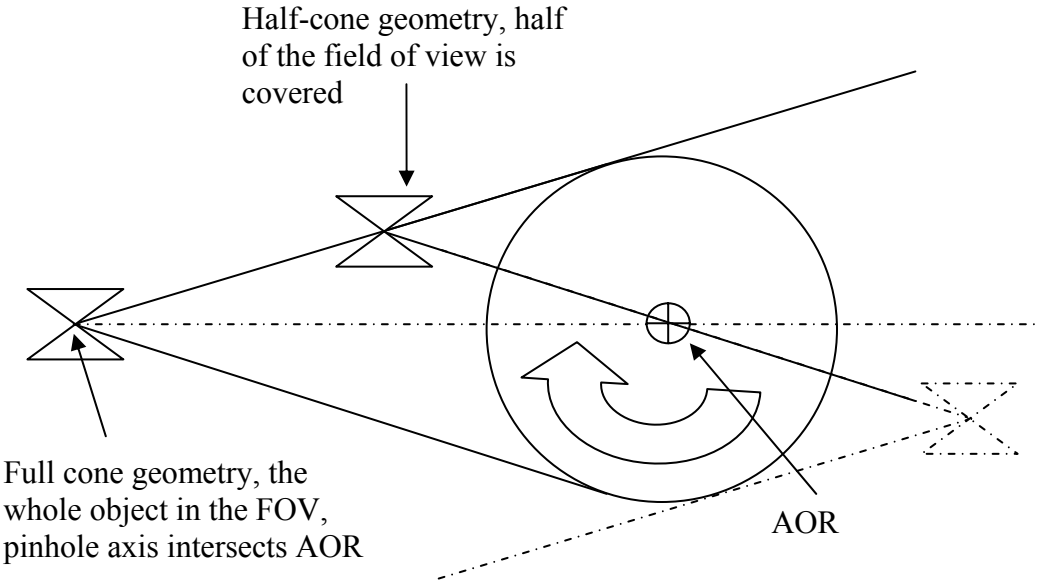

Fig.3.18.*Schematic of half-cone acquisition geometry. Solid lines represent pinhole acceptance angles. AOR is perpendicular to the drawing plane .Second camera can be positioned at the location of dash-dotted pinhole symbol*

Reduction in source to pinhole distance can be quite large depending on the acceptance angle and radius of FOV. For example in our design, FOV is 4 cm in diameter and we plan on using 45 degree angle pinholes. In full cone geometry source to pinhole distance is usually defined as the distance from the pinhole to the AOR and is commonly referred to as radius of rotation (ROR). So ROR for 4 cm FOV and 45 degree pinhole would be about 5 cm :

$$ROR = \frac{FOV}{2 \times \sin(\alpha / 2)} = \frac{4}{2 * \sin(22.5^{o})} = 5.23$$

In half-cone arrangement ROR is not measured along the pinhole axis, but instead along the side surface of the cone of acceptance. Nevertheless, a comparison can be made:

$$ROR = \frac{FOV}{2 \times \sin(\alpha)} = \frac{4}{2 \times \sin(45^{0})} = 1.41$$

So adding one more gamma camera can provide the decrease in source to pinhole distance of almost a factor of 4. Assuming that efficiency scales as an inverse square of the ROR, a 16-fold gain in efficiency of two-camera assembly can be expected. To make a fair comparison, this number should be divided by two, since second camera can be added to a full cone arrangement as well. Upon careful inspection of the calculated ROR value, one can notice that calculated ROR is smaller than the radius of FOV, meaning that if an object occupies the whole field of view optimal placement of detectors is impossible due to mechanical collision. This is not a design flaw, but rather an illustration on the limits of the approach.

There is a more fundamental problem in half-cone geometry. Fig.3.19 displays a top view of an ellipsoidal mouse being scanned using half-cone arrangement of cameras. The long half-axis of a mouse coincides with the AOR. Colored circles represent slices

through the pinhole acceptance cones. In half-cone geometry one cone points into the page, another one points out. It is crucial in half-cone geometry that cones of acceptance intersect.

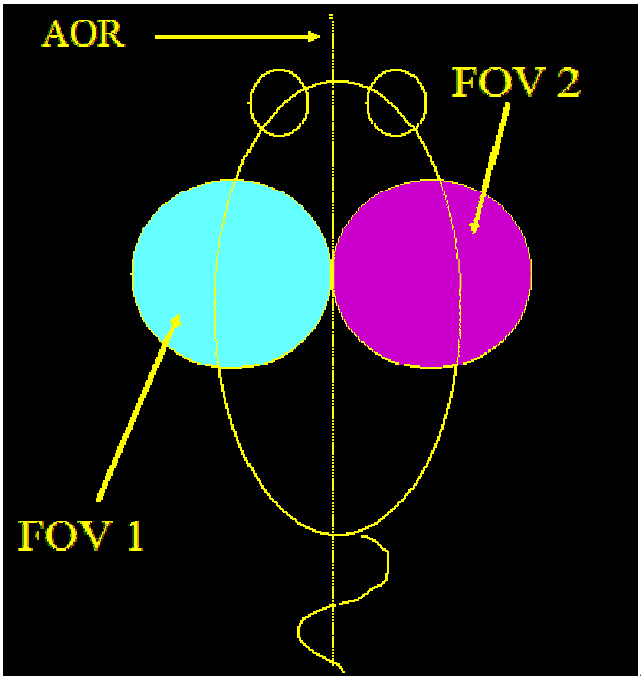

Fig.3.19.*Visualization of intersection of opposing FOVs, p.1*

In Fig.3.19 fields of view of two cameras intersect in a single point. Only point on the line perpendicular to the AOR and passing through the point of intersection will be completely sampled during the scan. For example, all points but one along the AOR will never be imaged by either of the two cameras. Ultimately it means that only one trans-axial slice, the one that contains point of intersection of the cones, can be successfully reconstructed. Fig.3.20 shows slightly better arrangement of the cameras. FOVs intersection is an area rather than a point. Complete set of data can be obtained for every trans-axial slice passing through the area of intersection. However there is still fair amount of areas that a scanner can potentially sample completely, but failed to do so.

Trans-axial slices that intersect top and bottom of acceptance cones encounter some black areas on their way. No data exists for the black areas, so successful image reconstruction is not possible.

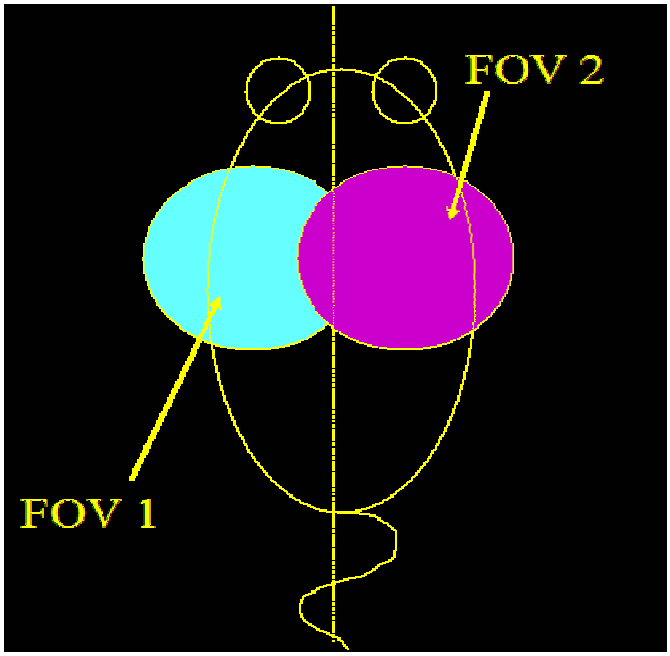

Fig.3.20.*Visualization of intersection of opposing FOVs, p.2*

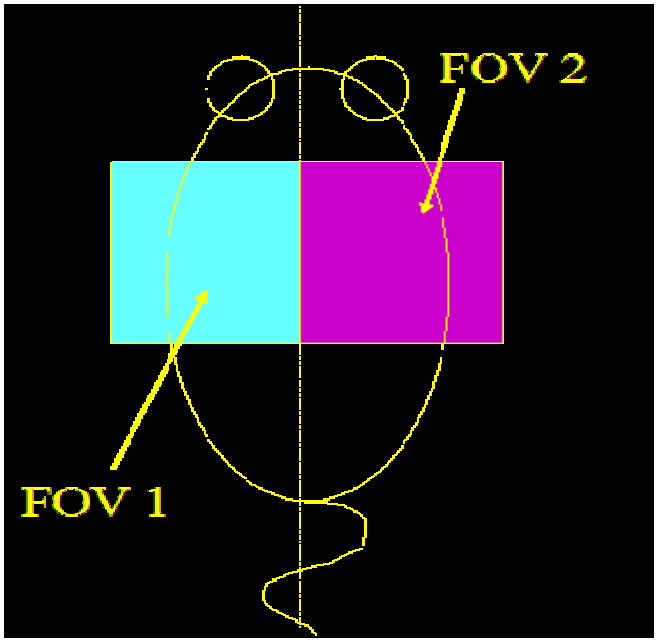

Fig.3.21.*Visualization of intersection of opposing FOVs, p.3*

Fig.3.21 exhibits data acquisition geometry that delivers completely sampled set of data. Every trans-axial slice can potentially be reconstructed without undersampling artifacts. This data acquisition scenario can take place if one can somehow transform a pinhole's cone of acceptance into a pyramid of acceptance, so that FOVs can intersect along a plane. This challenge can be answered by employing new variety of pinhole collimators - square shape pinhole collimators.

3.4 Square shape pinhole collimators

Square shape pinhole collimators were manufactured for us by Mikro Systems (Charlottesville, VA). Collimators were made out of tungsten polymer, basically tungsten powder held together by epoxy glue. Tungsten content in the first batch of pinholes was about 70%. Material had density slightly less than that of lead. Linear attenuation coefficient for 140 keV gamma rays was measured to be ~ 19 cm^{-1}. Fig.3.22 shows a photograph of one of the first apertures produced.

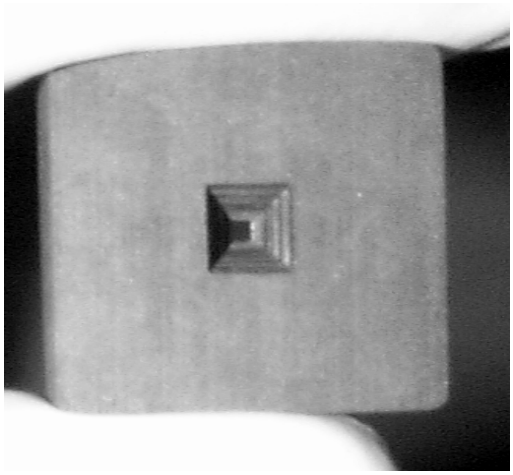

Fig.3.22.*Photograph of square shape pinhole collimator*

Characterization of imaging properties of square pinholes was carried out as a comparative study between conventional round apertures and square ones. Standard imaging characteristics like efficiency and spatial resolution were of interest. It was of interest to determine how square shape affects pinhole point response function (PRF). Initial attempt on theoretical description of pinhole characteristics have failed. Square shape breaks azimuthal symmetry around pinhole axis, so direct integration of (3.7) is not possible. One attempt of characterizing a square pinhole as a superposition of two orthogonal 1-D pinholes yielded no satisfactory results. Instead of trying to analytically derive a closed form expression for square pinhole spatial resolution and efficiency, we opted for a simulation approach. A simple ray-tracing program was implemented in IDL. Program models propagation of gamma radiation through the material with a user selectable attenuation coefficient. Simulated gamma radiation was emitted in random direction from a point source. Gamma rays were distributed uniformly over a surface of unit sphere. Origin of the coordinate system used was located at the center of pinhole aperture. Source coordinates are inputted by user. Two versions of the program were written, one with a simulated square, another with a simulated conventional round pinhole. Pinholes were modeled as zero attenuation openings in otherwise attenuating material. Opening shapes were squares and circles for square and round pinholes respectively. Attenuation coefficient of the material was chosen to match that of tungsten polymer at 140 keV. Propagation of gamma radiation through the material was governed by Beer's law with user predefined step size. Compton scatter was not included in the simulation. Gamma radiation detector was modeled as an array of tightly packed NaI

crystals. Intra-crystal gaps were not simulated. Effects of depth-of-interaction were included by means of including simple process of gamma absorption by NaI. Effects of detector intrinsic spatial resolution were included by means of Gauss smearing of detected particles with FWHM matching the value of a real detector. Programs output included image array, total number of detected events and efficiency of the system. Different shapes of sources can be programmed by appropriately locating closely spaced point sources. For our studies, point and line sources were used the most.

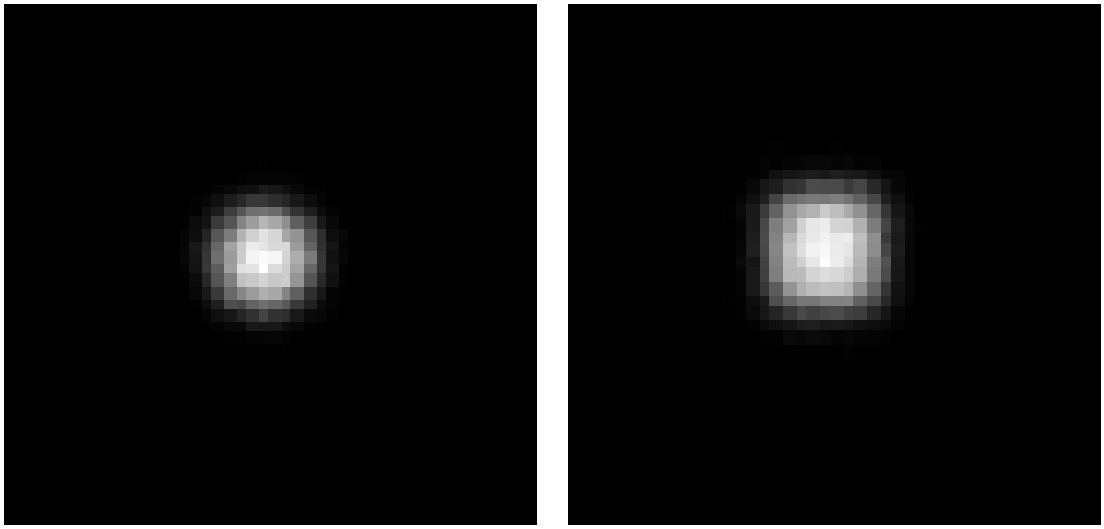

Fig.3.23.*Pinhole's point response functions (PRFs). Left – round pinhole, right – square shape aperture*

Fig.3.23 exhibits point response functions of square and round pinholes. Pinhole openings were 1 mm diameter for a round hole and 1 mm side length for a square hole. Both pinholes had full opening angles of 40 degrees. Square modulation of square pinhole response is easily noticeable. Fig. 2.24 displays a surface plot of the difference between square and round PRFs.

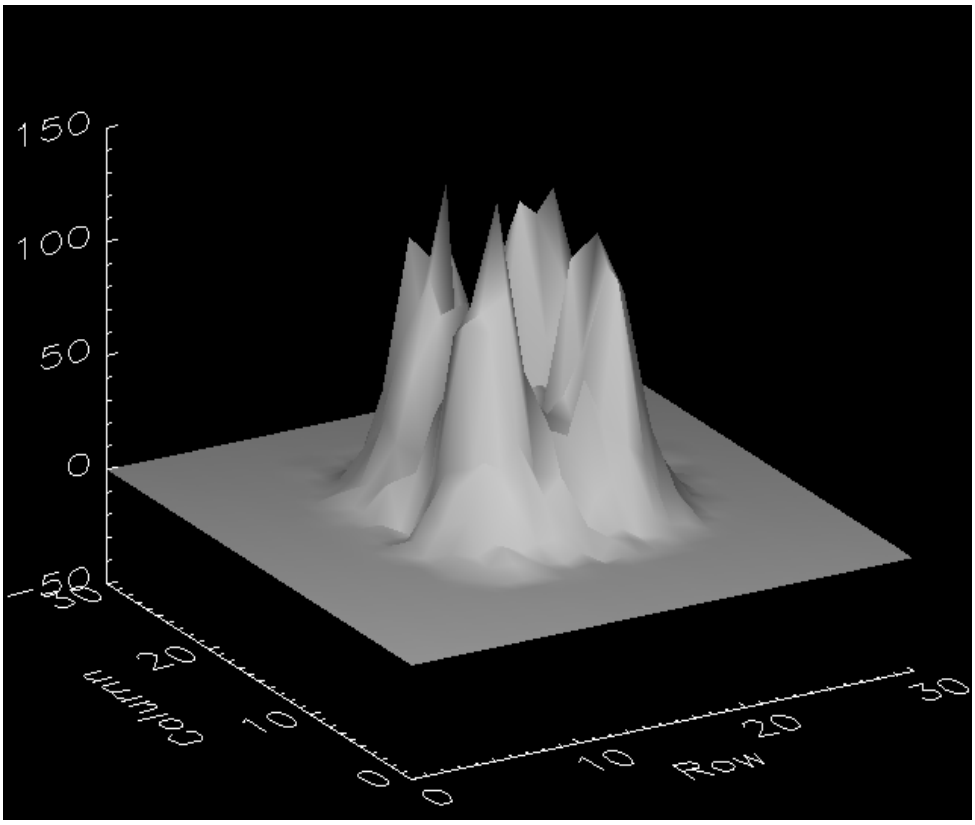

Fig.3.24.*Surface plot of the difference between PRFs*

Observing surface plot of the difference of PRFs it can be qualitatively predicted that square opening hole will possess better efficiency, but poorer spatial resolution. Quantitatively, efficiency of 1 mm square pinhole was 23 % higher than of 1 mm round one. To estimate spatial resolution we modeled a line source of radioactivity by positioning point sources in a straight line, with each source spaced 100 microns from each neighbor. Four different pinholes were tested, three of them being square 40 degrees opening angle pinholes of various opening size. Sizes of 0.5, 0.75 and 1.0 mm were tested. Fourth aperture to be simulated was round pinhole of 1 mm opening diameter and 40 degrees acceptance angle. At the same time four real pinholes with the same parameters as simulated ones were tested using procedure described in section 3.2.1.

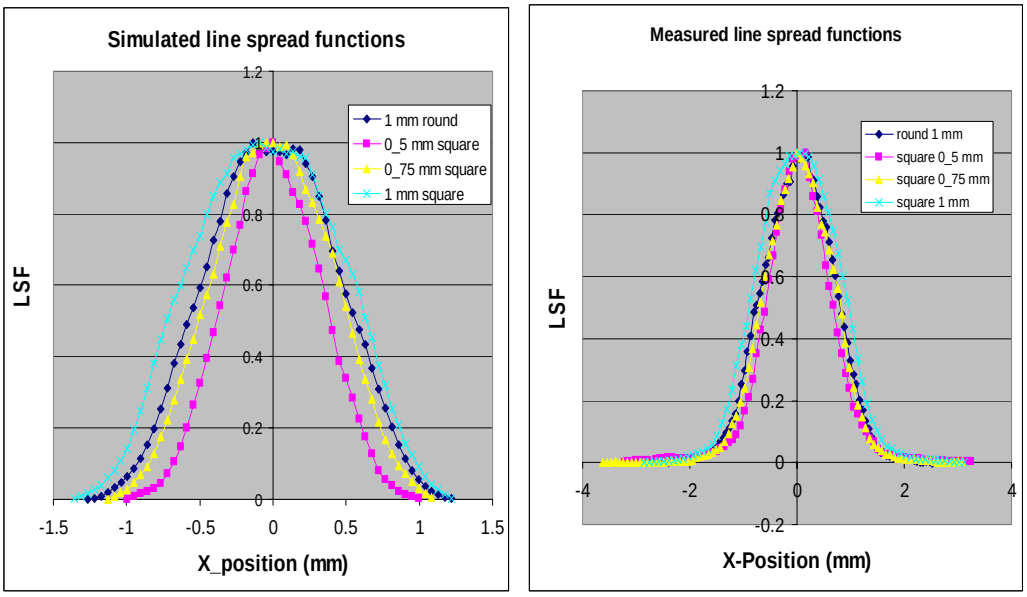

(a) (b)

Fig. 3.25.*Line spread functions (a) simulated and (b) measured of 4 different pinhole apertures*

Fig.3.25 shows line spread functions obtained from the simulation code and the one measured directly. Figures show good qualitative agreement, but measured values are higher than predicted. Finite size of the capillary used in the experiment may introduce additional broadening of the LSF.

Another simulation test was performed by placing 16 point sources in an equiangular manner 31 mm above the square pinhole opening at 15 degrees angle with respect to pinhole axis. 0.5 mm side square pinhole with opening angle of 45 degrees was modeled. Pinhole to detector distance was set to 103.92 mm and magnification factor of 3.32 was realized. Fig.3.26 exhibits surface plot of 16 point response functions. The purpose of the study was to investigate possible angular dependence of pinhole efficiency and spatial resolution. Efficiency was directly calculated by taking a ratio between the

number of counts in particular PRF and total number of emitted photons. Spatial resolution was estimated by fitting 2-D Gauss functions to individual PRFs and obtaining FWHM of each PRF. Dividing each FWHM by magnification factor yielded FWHM spatial resolution.

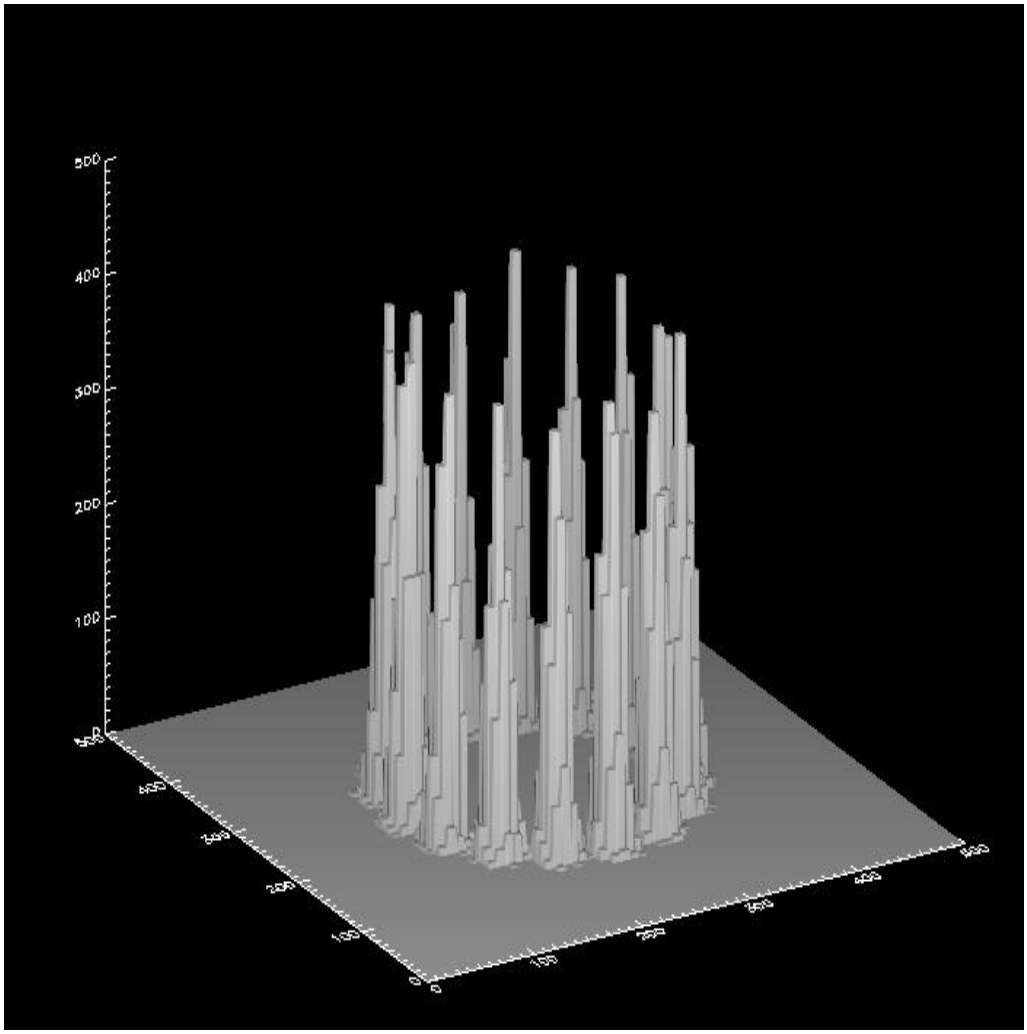

Fig.2.26.*Surface plot of 16 point response functions*

Fig.3.27 and Fig.3.28 display efficiency and spatial resolution of tested pinhole.

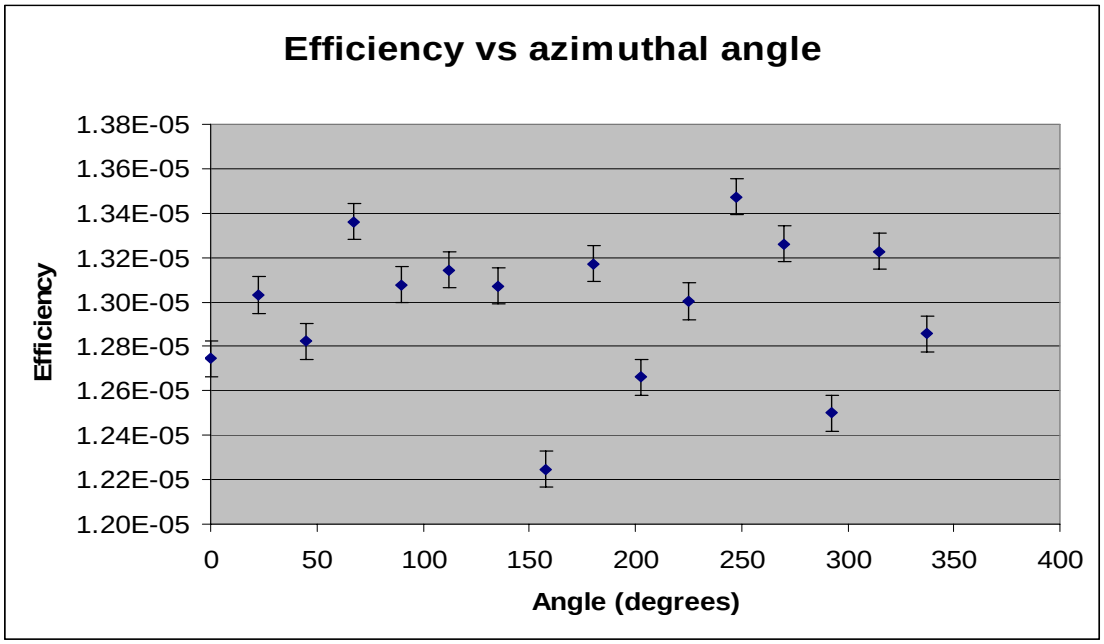

Fig.3.27.*Efficiency of a 0.5 mm 45 degrees angle square pinhole collimator*

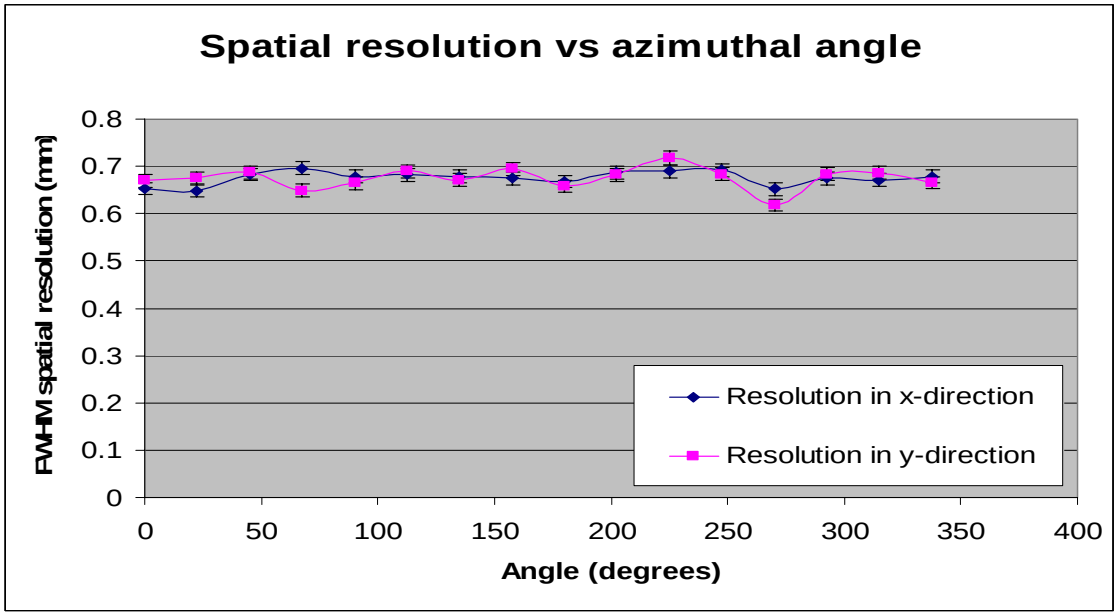

Fig.3.28.*Spatial resolution of 0.5mm 45 degree angle square pinhole collimator*

No visible trend in either efficiency or spatial resolution behavior can be observed.

Imaging of a simple capillary phantom was performed, see Fig.3.29. Phantom consisted of 5 narrow bore capillaries with outer diameter of 1.3 mm and inner diameter of 0.9 mm. Capillaries were filled with Tc-99m solution. Center-to-center spacing of the adjacent capillaries were 1.7 mm, 1.3 mm, 1.9 mm and 2.2 mm.

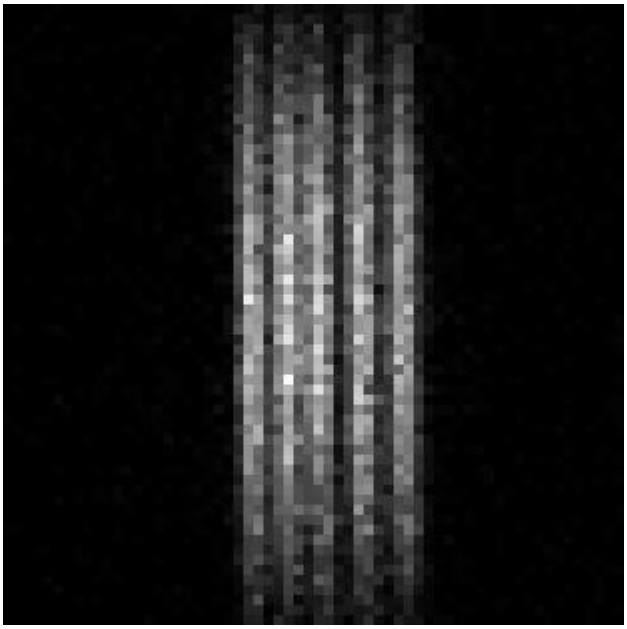

Fig.3.29.*Projection of a capillary phantom*

All the capillary pairs look to be resolved. Center-to-center separation of 1.3 mm corresponds to 0.4 mm separation of active areas of the capillaries. Three horizontal slices through the top, center and the bottom of the image were taken to estimate modulation between capillaries with 1.3 mm separation. Modulation turned out to be 87%, 78% and 92% for top, center and bottom profiles respectively. Using oversimplified method of source width de-convolution, spatial resolution of 0.92 mm was estimated.

References

[1] A. Hwang, K. Iwata, and B. Hasegawa, "*Simulation of depth of interaction effects for pinhole SPECT*" IEEE NSS/MIC Conf. Record, vol. 3, pp 1293-1297, 2001

[2] S. Metzler, J. Bowsher, M. Smith, and R .Jaszczak, "*Analytic determination of pinhole collimator sensitivity with penetration*", IEEE Trans. Med. Imaging, vol. 20, pp. 730-741, August 2001

[3] M.B. Williams, G. Zhang, M.J. More, A.R. Goode, S. Majewski, R. Wojcik, B. Kross, V. Popov, A. Weisenberger, M. Stanton, W. Phillips, A. Stewart, T. McCauley, T. Wu, and E. DiBella, "*Integrated CT-SPECT system for small animal imaging"* Proc.SPIE, vol. 4142, pp. 265-274, 2000

[4] H.Anger. "*Radioisotope Cameras, Volume 1. In: Instrumentation in Nuclear Medicine*", ed. G. Hine. New York: Academic, 1967.pp. 516-517

[5] M. Smith and R. Jaszczak, "*The effect of gamma ray penetration on angle-dependent sensitivity for pinhole collimation in nuclear medicine",* Medical Physics, vol. 24, pp. 1701-1709, 1997

[6] S. Metzler, J.Bowsher, K.Greer, R. Jaszczak, "*Analytic determination of the pinhole collimator's point-spread function and the RMS resolution with penetration*", IEEE Transactions on Medical Imaging, vol. 21, pp.878-887, August 2002

[7] Popov V., Majewski S., Weisenberger A.G., Wojcik R., *"Analog readout system with charge division type output"*, 2001 IEEE Nucl. Sci. Symp. Conf. Rec., vol. 4, pp. 1937 – 1940, 4-10 Nov. 2001

[8] Wojcik R., Majewski S., Kross B., Popov V., Weisenberger A.G., "Optimized readout of small gamma cameras for high resolution single gamma and positron emission imaging", 2001 IEEE Nucl. Sci. Symp. Conf. Rec., vol. 3, pp. 1821 – 1825, 4-10 Nov. 2001

[9] Stolin A.V., Williams M.B., Kundu B.K., Majewski S., Popov V., Weisenberger A.G., "Characterization of imaging gamma detectors for use in small animal SPECT", 2003 IEEE Nucl. Sci. Symp. Conf. Rec., vol. 3, pp. 2085 – 2089, 19-25 Oct. 2003

CHAPTER 4
Mechanics and calibration of the scanner

The scanner's mechanical structure plays a role in the process of data acquisition that is as important as that of the imaging subsystems. Unknown geometrical misalignments or seemingly negligible errors in angular positioning have a big impact on the quality of the reconstruction data. It is impossible to construct a perfectly rigid mechanical device that is capable of rotating significant weights (for example, the total weight of the detectors of our scanner is about 150 kg). Therefore, after the best effort was made to ensure the stability of the components, their mechanical alignment was performed using a laser beam technique. Furthermore, in order to quantify any possible remaining mechanical imperfections, special calibration phantoms were designed, built and imaged. After processing the results of the phantom scans, final calibration parameters were obtained and used as inputs for the reconstruction programs. This chapter will describe the above mentioned designs and experiments.

4.1 Rotating gantry and mounting hardware

A rotating gantry is the foundation of every CT/SPECT scanner intended to image stationery object. Flaws in gantry design can plague even a system with perfect imaging detectors. Mechanical robustness, accurate angular positioning and, preferably, ease of

use are the objectives to be met when designing and implementing a gantry. This subchapter will describe our choice of rotating apparatus.

Both imaging subsystems are mounted on a barrel-type gantry with an open structure (Fig. 4.1 and 4.2). Such a gantry type was chosen for its relatively low cost and, more importantly, for the flexibility it provides for the component's rearrangements. The gantry is comprised of two 43-inch diameter steel wheels (HepcoMotion, Devon, UK) connected to eight 60-inch long aluminum profiles (80/20, Inc, Columbia City, IN). The wheels are confined within sets of three rollers permanently attached to an outside support frame. One of the wheels has gear teeth cut along its circumference and is coupled to the output shaft of a 47:1 ratio gear box FA C45 R (Gudel US, Ann Arbor, MI). The gearing ratio between the large driving wheel and an output shaft is 14.4. A Smart Motor 17-series (Animatics Corp, Santa Clara, CA) brushless DC servo motor is connected to the input of the gear box. The motor is rated at 2000 encoder counts per revolution, thus the maximum possible resolution of the gantry motion is 2.66E-4 degrees. In reality, the gear box exhibits a backlash of 15 arc minutes, which reduces the motion accuracy to 3.89E-4 degrees. Most of the CT scans do not include more than 1440 frames over 360 degrees (a step size of 0.25 degrees). Since CT is more sensitive to angular position imperfections than SPECT, the estimated gantry motion accuracy is sufficient. The motor is controlled by a PC via RS-232 communication. A custom-designed interface, written in LabView (National Instruments, Austin, TX), was implemented as a stand-alone program and parts of it were later used in the CT-controlling software. The interface provides the user with the ability to start and stop the gantry motion as well to receive internal encoder feedback for angular position tracking.

A small wood surface table was attached to the front side of the gantry to support the alignment laser and animal anesthesia setup. Two interchangeable animal bed supports, one for mice and one for rats, are rigidly fixed to the outer frame, and span the entire length of scanner along its axis of rotation. The supports are made out of carbon fiber tubes for low radiation attenuation. The central section of each tube was cut along its axis to create open half-cylinders into which the animal beds are placed. The tube diameters of 1 and 1.5 inches were chosen to accommodate beds suitable for average sized mice and rats respectively. Several aluminum profiles were mounted to the 60-inch long aluminum profiles perpendicularly to the axis of rotation for the imaging equipment to be mounted on. Mounting hardware for each subsystem was designed to permit adjustment of component position. The process of subsystem alignment will be discussed later in this chapter.

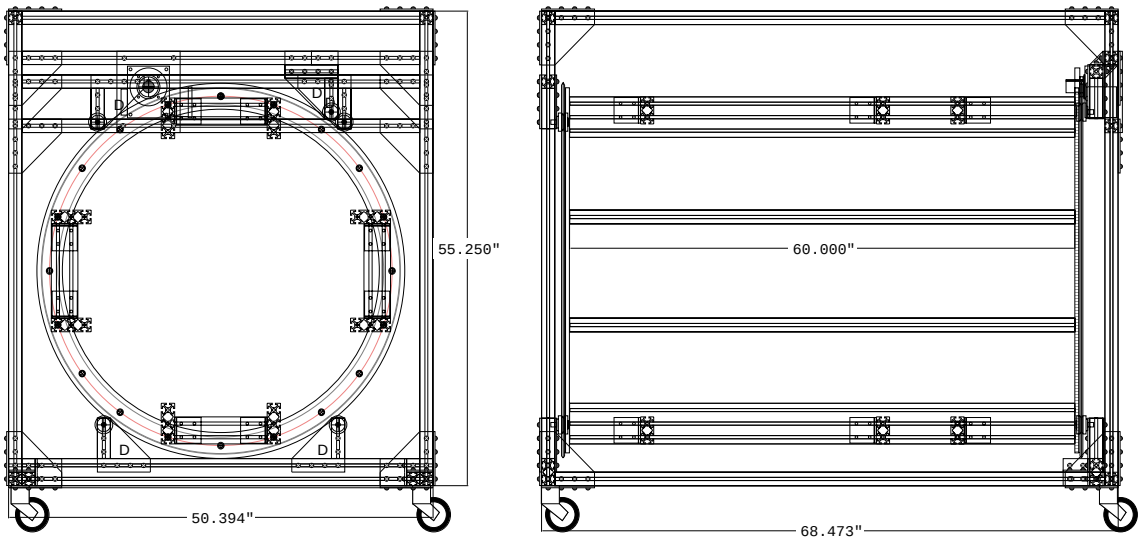

Fig. 4.1.*Schematic of the rotating gantry*

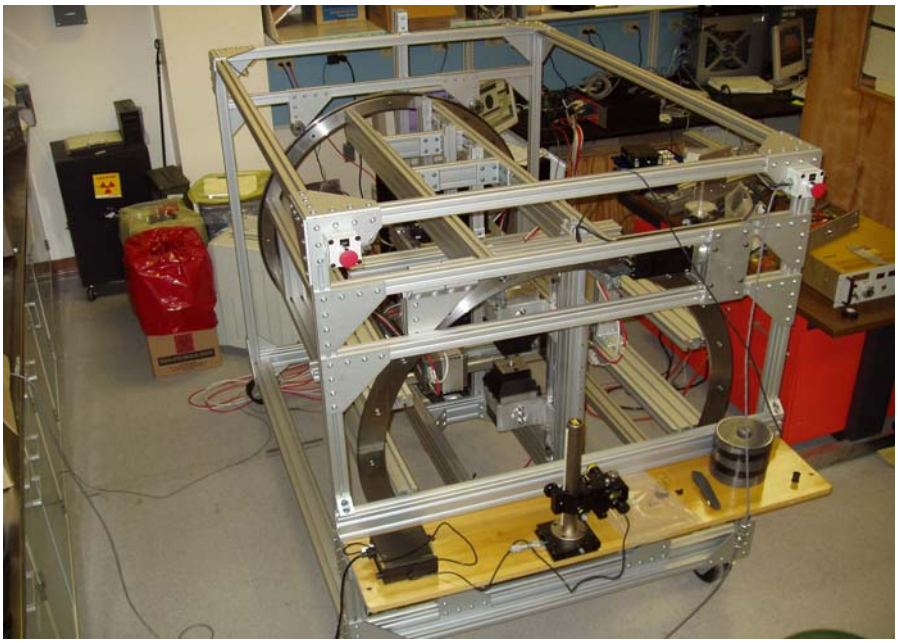

Fig. 4.2.*Photograph of the scanner*

4.2 System alignment and calibration

Every reconstruction algorithm relies on an accurate description of image acquisition geometry. Lack thereof produces various artifacts and, consequently, loss of spatial resolution. Similar to building a perfectly rigid gantry, it is impossible to implement an imaging system with ideally aligned components. Both commercial scanners and laboratory systems include some kind of geometrical calibration procedures in addition to careful detector alignment.

To illustrate a problem in question a general setup of an ideal CT and non-ideal pinhole SPECT acquisition geometries are shown in Fig.4.3 and Fig.4.4.

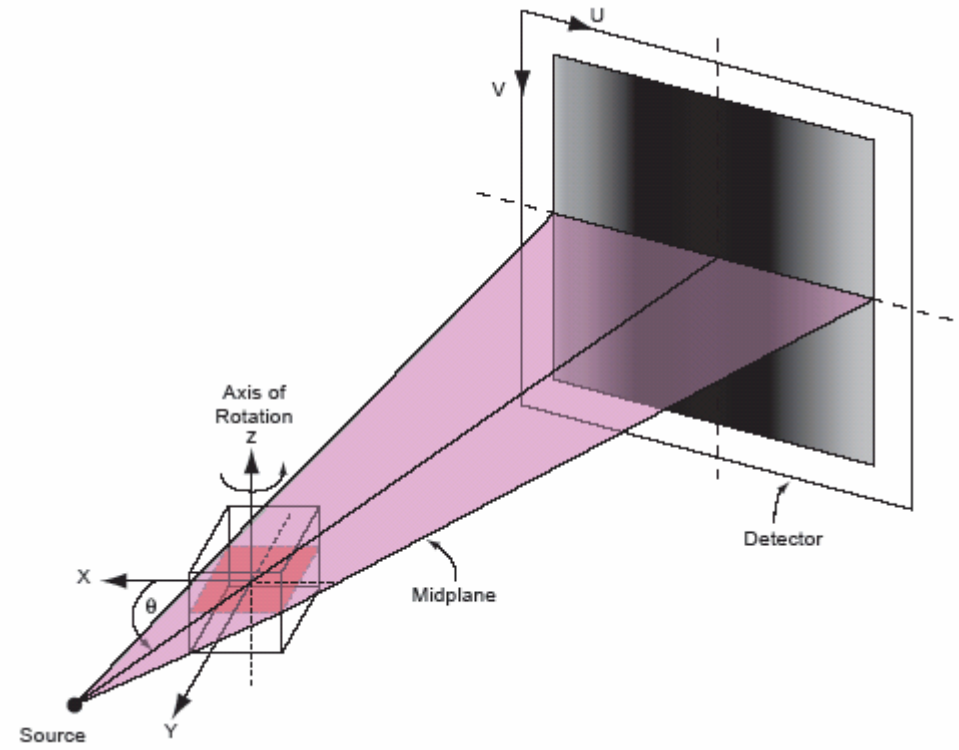

Fig.4.3.*Ideally aligned x-ray CT system*

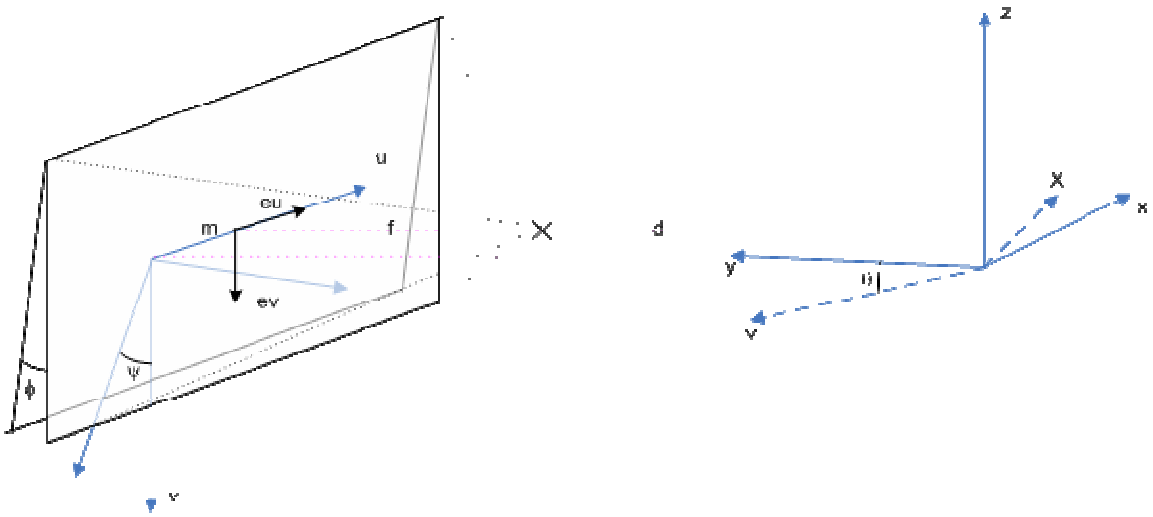

Fig.4.4.*"Real world" pinhole SPECT acquisition geometry*

In both setups scanner axis of rotation coincides with the Z axis of the lab coordinate system. Parameters of acquisition geometries are similar for both CT and SPECT, so without a loss of generality pinhole SPECT system will be discussed.

For a camera rotating in circular orbit around rotation axis, seven parameters are necessary and sufficient to fully describe acquisition geometry [1],[2]. Some of those parameters were already discussed in chapter 3, but will be repeated here for completeness. Collimator focal length f – distance between the pinhole and the detector surface, electrical shifts e_u and e_v – collective translations of projection images, caused by a drift in detector hardware, constitute parameters intrinsic to a camera. The extrinsic parameters d, m, Φ, and Ψ depend on the position of the detector with respect to the AOR. They are conveniently described using a central ray – pinhole projection perpendicular to the detector surface (in case of CT – a projection of the of x-ray source focal spot). Parameter m, referred to as mechanical offset, is the offset of the central ray from the AOR. Parameter d is the distance measured along the central ray between the collimator focal spot and AOR in the absence of the mechanical offset. Angular parameter Φ describes the tilt between the detector surface and the AOR. Finally, twist angle Ψ describes the orientation of the pixel matrix with respect to the AOR. Ideal geometrical alignment assumes that parameters m, Φ, Ψ, e_u and e_v are zeroes. In order to evaluate geometrical parameters of the system the location of the AOR must be identified.

4.2.1 Laser alignment system

Precise localization of the axis of rotation (AOR) of the scanner is of utmost importance for successful data acquisition and reconstruction. Errors in the assumed projection of the AOR onto the detectors will result in severe image artifacts. We implemented an AOR calibration setup following the guidelines of [3]. The overall approach is to align a laser beam with the AOR with the best possible precision. After that is achieved, animal bed supports are positioned such that their axes are close to the AOR. Then, detector alignment is facilitated by the use of a beam splitter, which creates laser beams perpendicular to the AOR. These steps are described in more detail below.

The setup utilizes a position stabilized laser source (Melles-Griot 05 LLR 811 247, Carlsbad, CA), lateral effect laser beam detector (Melles-Griot 13 PSL 005, Carlsbad, CA) and motorized translation stage (A40-series, Velmex, Bloomfield, NY). The laser is mounted on a precision two-axis positioning device. The device allows for angular adjustments in the polar and azimuthal directions. Schematic of the laser holder is shown in Fig.4.5.

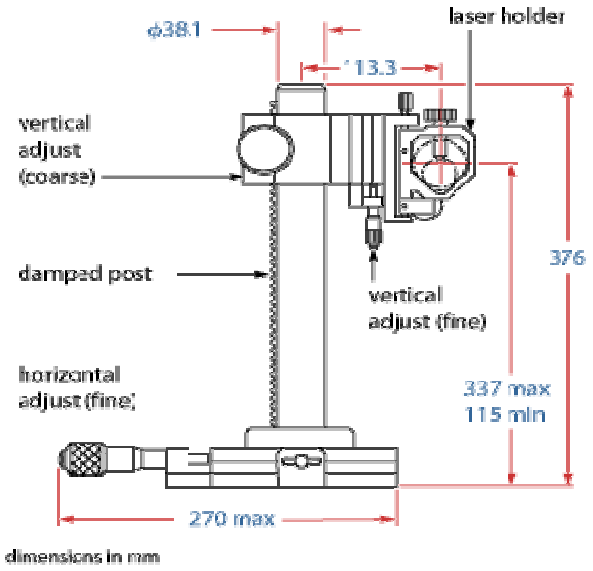

Fig.4.5.*Technical drawing of laser positioning assembly*

4.2.1.1 Geometry of the setup

In coordinate system we used, the $\hat{x}$, $\hat{y}$ and $\hat{z}$ directions are fixed in the laboratory frame of reference. The scanner may rotate by an angle γ about the AOR. Fig. 4.6 is a schematic with a single detector mounted on the gantry for clarity. By definition, the AOR corresponds to the z axis. The $\hat{z}$ direction is anti-parallel to the laser direction, when the laser is properly aligned. The $\hat{y}$ direction is determined by the orientation of the normal to the plane of mounting support structure when γ = 0. The choice of origin for angle γ is arbitrary and for certainty is chosen such that the $\hat{y}$ direction is close to being anti-parallel to gravity. The $\hat{x}$ direction is selected to form a right-handed system. The normal to the plane of the mounting profile depends on γ:

$$\hat{N}_D = \begin{bmatrix} \sin\gamma \\ \cos\gamma \\ 0 \end{bmatrix} \tag{4.1}$$

When using the laser alignment system, we assume that the translation stage with the affixed laser beam detector is rigidly attached to its mounting profile and thus rotates in a perfect circle about the AOR. We allow for the mounting profile to have a fixed tilt measured by the angle α (Fig. 4.7) with respect to the AOR.

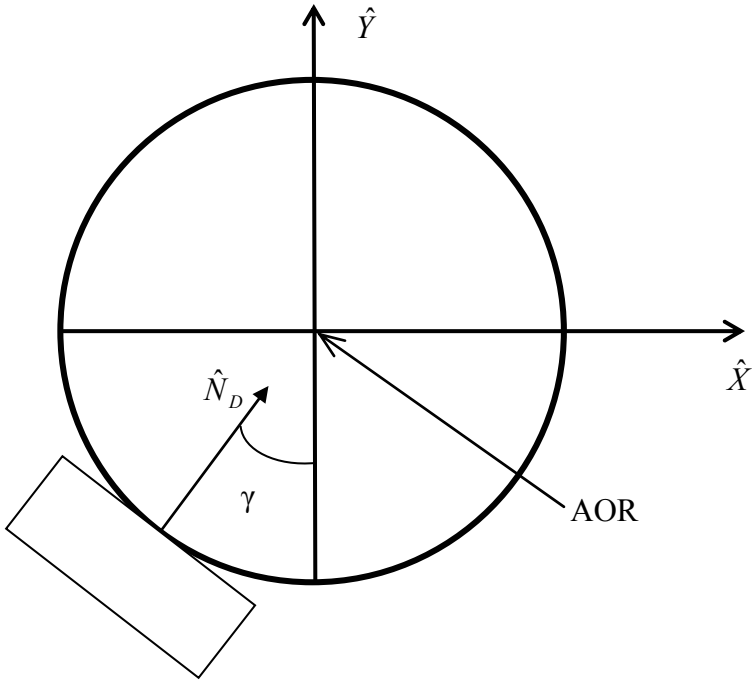

Fig.4.6.*View of the coordinate system. The direction of the AOR is out of the page*

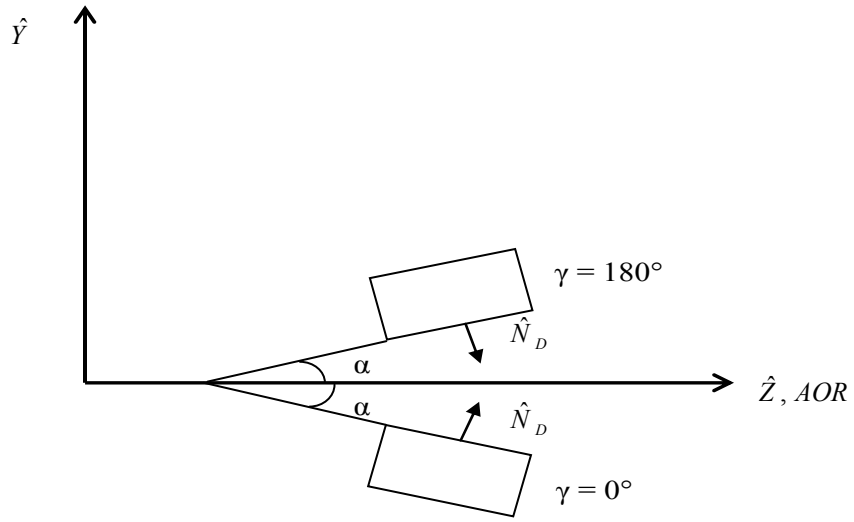

Fig.4.7.View of the coordinate system along the x axis. Angle α measures a fixed tilt of the support structure with respect to the AOR

When allowing for $\alpha \neq 0$:

$$\hat{N}_D = \begin{bmatrix} \sin\gamma\cos\alpha \\ \cos\gamma\cos\alpha \\ \sin\alpha \end{bmatrix} \tag{4.2}$$

To align the laser, the direction of the beam must be parameterized. That direction is then used to iteratively adjust the laser until it is aligned. The direction of the laser is given by:

$$\vec{v}_L = \begin{bmatrix} -\cos\theta\sin\varphi \\ -\sin\theta \\ -\cos\theta\cos\varphi \end{bmatrix} \tag{4.3}$$

where θ measures the y component of the laser relative to the AOR and φ measures the x component (Fig. 4.8). The laser is anti-parallel to the AOR when θ = φ = 0. In general the two-dimensional (2-D) position of the laser beam as a function of z is:

$$\vec{P}_L(z) = \begin{bmatrix} x_L \\ y_L \end{bmatrix} + z\begin{bmatrix} \tan\varphi \\ \tan\theta\sec\varphi \end{bmatrix} \tag{4.4}$$

where x_L and y_L are the x and y positions at z = 0 of the laser beam relative to the AOR.

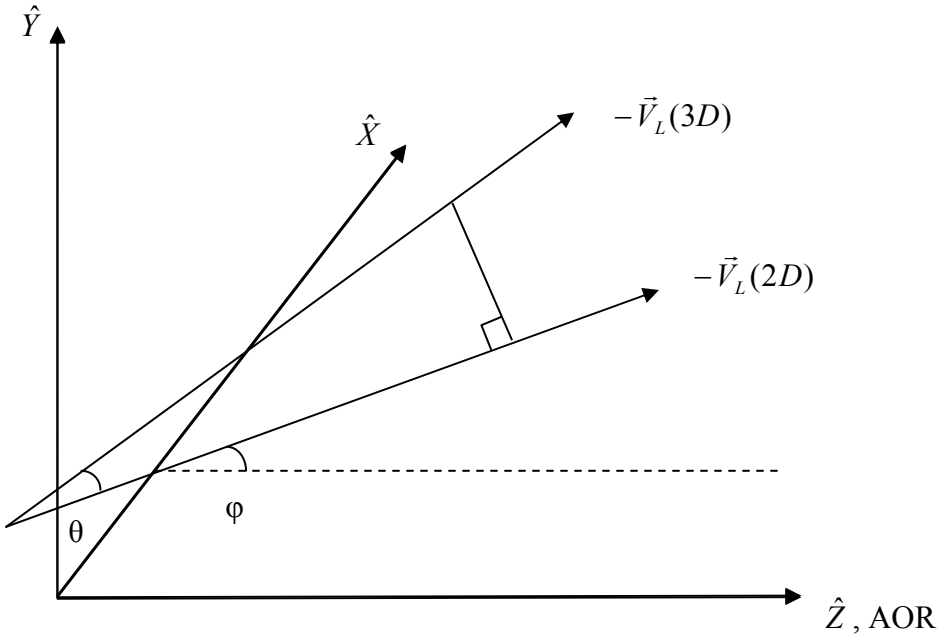

Fig.4.8.Orientation of the laser beam with respect to AOR. The vector $-\vec{V}_L(3D)$ is the direction of the laser beam, and the vector $-\vec{V}_L(2D)$ is the projection of $-\vec{V}_L(3D)$ onto the X-Z plane

4.2.1.2 Accuracy of Laser Position Determination

The laser detector is used to measure the 2-D position of the beam at several axial positions to determine the relative slopes of the beam and the AOR. The typical starting distance between the laser and the detector is about 200 cm.

To measure the accuracy of the laser beam localization by the detector and the beam's temporal stability, the 2-D position of the stationary laser beam was read out once per second for 1800 seconds (30 minutes). To separate the effects of detector localization reproducibility and laser beam temporal stability, statistical analysis was performed on the readings in two ways: "set standard deviation" and "global standard deviation". The

set standard deviation was calculated by grouping data in 18 sets of 100 readings each. The variance was calculated for each set. The variance was then averaged across sets. The square root was taken to arrive at the average set standard deviation. The reason the data were separated and averaged was to remove the effects of any drift of the beam over time. The global standard deviation was calculated by considering the 1800 data points to come from a single set. In addition, the data were fit to a Gaussian distribution.

The results of the statistical analysis for a stationary detector are summarized in Table 4.1.

Coordinate	Set σ (μm)	Global σ (μm)	Gaussian fit σ (μm)
x	5.9	6.8	6.4
y	5.0	12.3	11.6

Table 4.1.Standard deviations of static laser beam position readout

The results of the set analysis suggest that uncertainty in the beam location due to detector measurement variability and any potential rapid laser beam position fluctuations is only approximately 5 – 6 microns in both the x and y directions. However, the results of global analysis suggest a slower beam position drift in the y direction. Gaussian fits to the distributions for the x and y coordinates obtained using global analysis are shown in Fig. 4.9. The fact that no significant beam position fluctuations were noticed during 100 seconds acquisitions is important for the next stage of the experiment, discussed in the next sub-chapter, in which 120 second long data collecting periods were used. Based on these results we assume that beam position fluctuations are not going to affect the results of those experiments significantly.

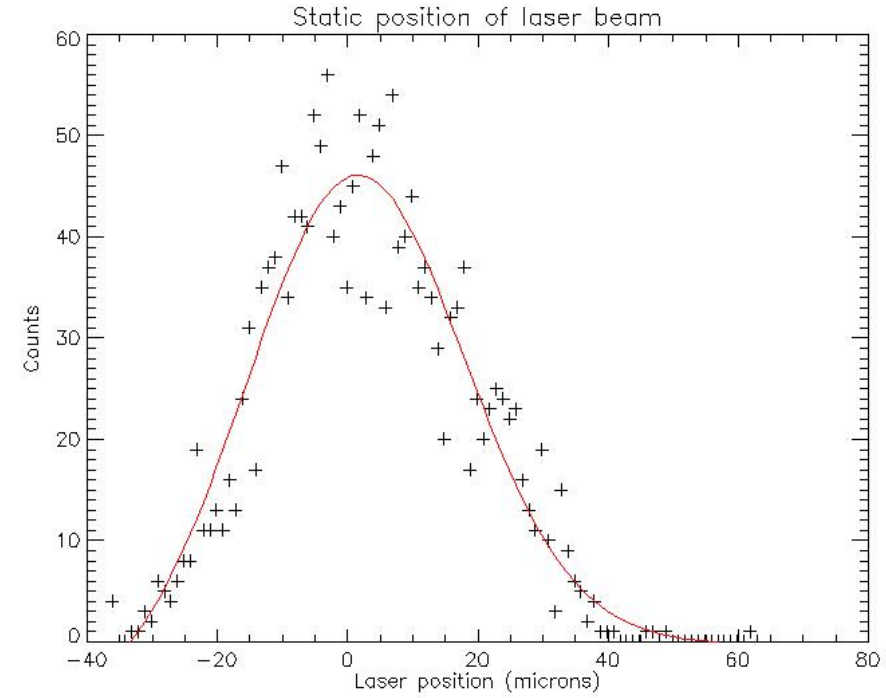

(b)

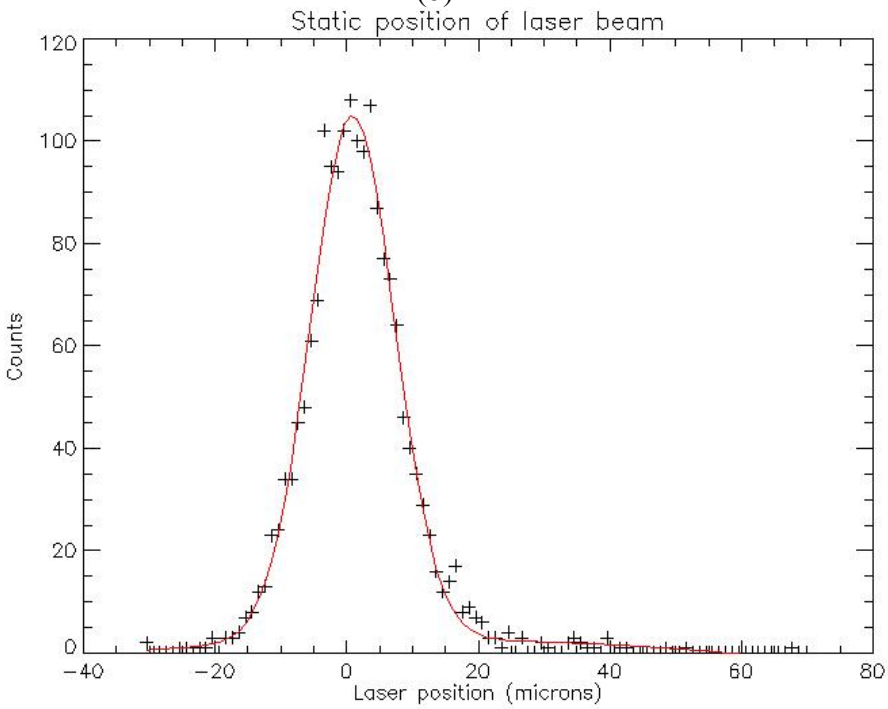

(a)

Fig.4.9.*(a) Position distribution of x and (b) y coordinates of the laser beam, using the entire 1800 point data set*

4.2.1.3 Aligning of the Laser with the AOR

In order to align the laser beam with the AOR, a linear translation stage upon which the laser detector was mounted was fastened to a mounting profile. Translation of the detector is then used to measure the slope of the laser beam with respect to the AOR. The schematic of the experiment is shown in Fig.4.10.

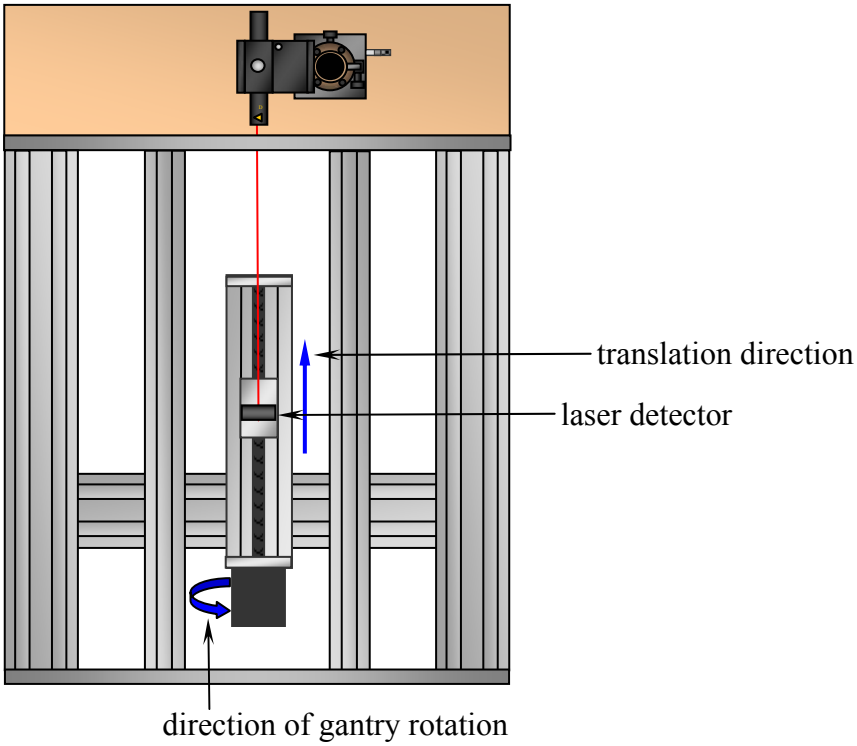

Fig.4.10.*Mounting of the translation with affixes laser detector on the gantry*

The direction of movement of the stage and target is given by:

$$\vec{v}_T = \begin{bmatrix} \cos\alpha \sin\beta \\ \sin\alpha \\ \cos\alpha \cos\beta \end{bmatrix} \tag{4.5}$$

where β is the angle between the direction of the stage and the AOR in the y = 0 plane, when measured at γ = 0° (Fig. 4.11). The linear stage was moved at a constant speed of 1.0 mm/s in the $\vec{v}_T$ direction over a distance of 120 mm. The target was read out every second to produce 120 data points. For convenience we introduced the variable z' which denotes the position of the linear stage along the $\vec{v}_T$ direction. It is equal zero when the z component of the stage's position is also zero. Thus

$$z = z' \cos\alpha \cos\beta \tag{4.6}$$

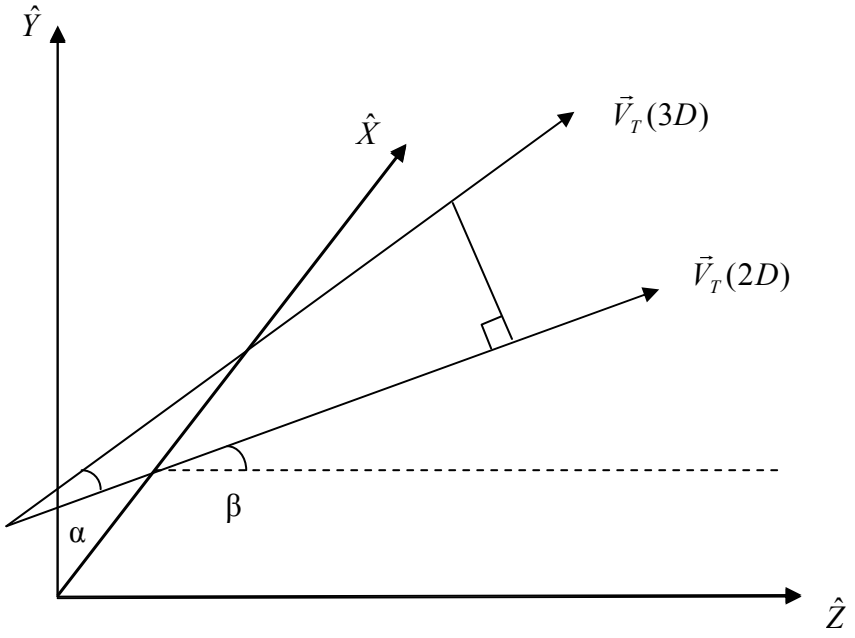

Fig.4.11.*Orientation of the translation stage relative to the AOR. Vector* $\vec{V}_T(3D)$ *is the direction of the linear stage's movement. The vector* $\vec{V}_T(2D)$ *is the projection of* $\vec{V}_T(3D)$ *onto the X-Z plane*

The 2-D position of the center of the detector as a function of z' is then

$$\vec{P}_T(z') = \begin{bmatrix} x_T \\ y_T \end{bmatrix} + z \begin{bmatrix} \tan\beta \\ \tan\alpha \sec\beta \end{bmatrix} = \begin{bmatrix} x_T \\ y_T \end{bmatrix} + z' \begin{bmatrix} \cos\alpha \sin\beta \\ \sin\alpha \end{bmatrix} \tag{4.7}$$

Similarly, substituting for z into (4.4), one finds

$$\vec{P}_L(z') = \begin{bmatrix} x_L \\ y_L \end{bmatrix} + z' \begin{bmatrix} \cos\alpha \cos\beta \tan\varphi \\ \cos\alpha \cos\beta \tan\theta \sec\varphi \end{bmatrix} \tag{4.8}$$

The position of the laser was read out at various values of γ. Typical values have been chosen to be 0°, 90°, 180° and 270°. The center of the laser $\vec{P}_T(z)$ was then subtracted from the rotated position of the laser beam to arrive at the final readout values. Those values were

$$\begin{bmatrix} R_x \\ R_y \end{bmatrix} = \Re(-\gamma)(\vec{P}_L) - \vec{P}_T = \begin{bmatrix} R_{x0} \\ R_{y0} \end{bmatrix} + z' \begin{bmatrix} m_x \\ m_y \end{bmatrix} \tag{4.9}$$

where R_{x0} and R_{y0} are the x and y readout values at z = 0 respectively, $\Re$ is the 2-D rotation operator for rotation through the angle gamma, and m_x and m_y are the slopes of the readout with respect to z' in the x and y directions. From (4.7) and (4.8)

$$\begin{aligned} R_{x0} &= x_L \cos\gamma - y_L \sin\gamma - x_T \\ R_{y0} &= y_L \cos\gamma + x_L \sin\gamma - y_T \\ m_x &= \cos\alpha \cos\beta(\tan\varphi \cos\gamma - \tan\theta \sec\varphi \sin\gamma - \tan\beta) \\ m_y &= \cos\alpha \cos\beta(\tan\theta \sec\varphi \cos\gamma + \tan\varphi \sin\gamma) - \sin\alpha \end{aligned} \tag{4.10}$$

The values of θ, φ, α, and β were determined from experimentally obtained slopes at γ = 0°, 90°, 180° and 270°. From (4.10)

$$
\begin{aligned}
m_x(\gamma = 0^o) &= \cos\alpha\cos\beta\tan\varphi - \cos\alpha\sin\beta \\
m_x(\gamma = 90^o) &= -\cos\alpha\cos\beta\tan\theta\sec\varphi - \cos\alpha\sin\beta \\
m_x(\gamma = 180^o) &= -\cos\alpha\cos\beta\tan\varphi - \cos\alpha\sin\beta \\
m_x(\gamma = 270^o) &= \cos\alpha\cos\beta\tan\theta\sec\varphi - \cos\alpha\sin\beta \\
m_y(\gamma = 0^o) &= \cos\alpha\cos\beta\tan\theta\sec\varphi - \sin\alpha \\
m_y(\gamma = 90^o) &= \cos\alpha\cos\beta\tan\varphi - \sin\alpha \\
m_y(\gamma = 180^o) &= -\cos\alpha\cos\beta\tan\theta\sec\varphi - \sin\alpha \\
m_y(\gamma = 270^o) &= -\cos\alpha\cos\beta\tan\varphi - \sin\alpha
\end{aligned}
\tag{4.11}
$$

This can be solved for the angles

$$
\begin{aligned}
\alpha &= -\arcsin\left(\frac{m_y(0) + m_y(90) + m_y(180) + m_y(270)}{4}\right) \\
\beta &= -\arcsin\left(\frac{m_x(0) + m_x(90) + m_x(180) + m_x(270)}{4\cos\alpha}\right) \\
\varphi &= -\arctan\left(\frac{m_x(0) - m_x(180) + m_y(90) - m_y(270)}{4\cos\alpha\cos\beta}\right) \\
\theta &= -\arctan\left(\frac{m_x(270) - m_x(90) + m_y(0) - m_y(180)}{4\cos\alpha\cos\beta\sec\varphi}\right)
\end{aligned}
\tag{4.12}
$$

The angles θ and φ from (4.12) were then used to correct for the laser orientation. After the corrections had been made, the angles were re-measured as described above. The whole process was repeated until no further improvement was observed.

The means and standard deviations of the measured slopes are presented in Table 4.2.

γ (degrees)	Average m_x	$\sigma(m_x)$	Average m_y	$\sigma(m_y)$
0	-2.43e-03	9.4e-06	-1.56e-03	1.1e-05
90	-0.68e-03	1.7e-05	1.04e-03	1.2e-05
180	1.77e-03	1.3e-05	-0.26e-03	9.4e-06
270	0.20e-03	9.7e-06	-2.91e-03	1.7e-05

Table 4.2.*Values and errors of linear slopes*

From (4.12) and the Table 4.2 we estimated the values and uncertainties of the angles:

$$\alpha = (0.923 \pm 0.003) \times 10^{-3} \text{ (radians)}$$

$$\beta = (0.287 \pm 0.004) \times 10^{-3} \text{ (radians)}$$

$$\varphi = (6.03 \pm 0.17) \times 10^{-5} \text{ (radians)}$$

$$\theta = (11.0 \pm 0.2) \times 10^{-5} \text{ (radians)}$$

4.2.1.4 Centering of the Laser on the AOR

At this point, the laser is aligned anti-parallel to the AOR, but might not have been coincident with it. In this case, sweeping the target a full revolution around the AOR would generate a circular trace of the laser beam. The radius of the circle is equal to the displacement of the beam from the AOR. The laser is translated in the transverse directions to reduce the radius of the traced circle. After several iterations the process produces no visible improvements as the shape of the traced curve starts to deviate from the circular shape. The deviation is attributable to the vibrations of the target and laser beam during the gantry motion. The achieved alignment accuracy, estimated as the radius of the smallest circular trace was 400 μm.

4.2.2 Alignment of the Imaging Components

Having obtained a physical reference line, the next step is to align the imaging hardware and animal beds. Precise alignment of the imaging hardware is crucial for high image quality. Positioning of the animal beds relative to the AOR is less stringent, and only requires that the midline of the animal is close enough to the AOR that portions of anatomy do not rotate out of the field of view during tomographic image acquisition.

The purpose of the following procedure is to align the gamma cameras pinhole's axes and x-ray system central ray to intersect or nearly intersect the AOR. A motor-driven rotation stage with attached glass plate is utilized. The rotation stage is mounted in such a way that the laser beam is incident on the glass plate.

The schematic of the setup is shown in Fig. 4.12.

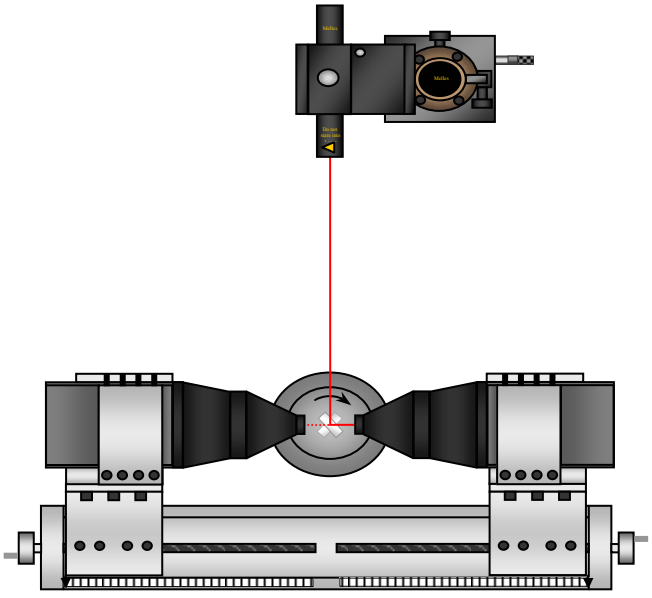

Fig.4.12.*Schematic of the gamma cameras alignment process*

4.2.2.1 Alignment of the Gamma Cameras

The SPECT subsystem hardware is shown in Fig. 4.13. The gamma cameras are mounted on an aluminum plate of the same width as the camera. Three shoulder bolts are press fitted in the plate to be flush with the surface the camera rests on. Two more

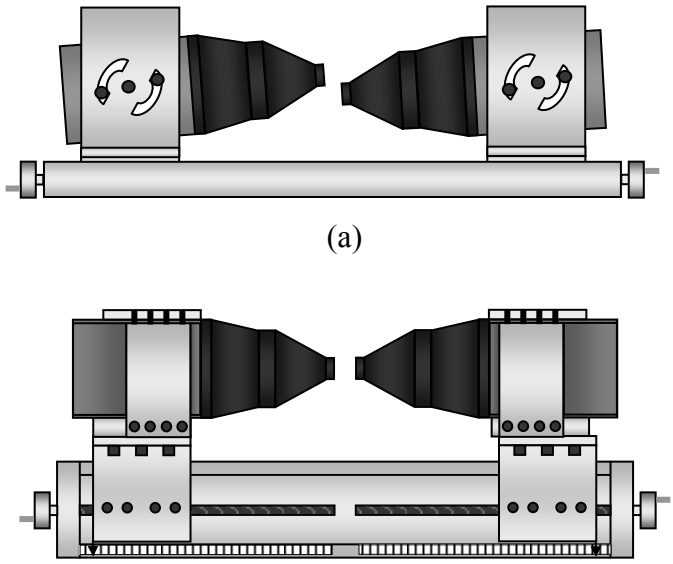

(a)

(b)

Fig. 4.13.*Side view of a tilted arrangement (a) and top view of the straight arrangement (b) of a gamma camera pair mounting hardware*

aluminum plates are screwed to the sides of the bolted plate to sandwich the camera in between them. Finally, a cover plate is fastened to the sides of sandwiching plates.

Shoulder bolts that were left sticking out of the bottom plate were inserted into the center hole and arc shaped cut-outs of the L-shape aluminum profile piece and tightened with nuts. L-shape profile was attached to a manual translation stage. Upon release and further

retightening of the securing nuts, this assembly allowed for the tilt of the camera necessary for half-cone acquisition geometry. The two gamma cameras of a half-cone pair are mounted on a common translation stage whose lead screw is threaded oppositely on either end (B-40 series, Velmex Inc, Bloomfield, NY) The stages are equipped with a side scale and a pointer for position readout. Assembled gamma pair was mounted onto a trans-axially mounted gantry profile to complete the installation. Horizontal leveling of the gantry profile and top surfaces of both detectors was checked with digital protractor (Mitutoyo, model Pro360). Leveling was verified to within accuracy of the protractor, 0.1°. Gamma cameras were then translated towards each other till the tips of the collimators came into contact. Point of contact was chosen such that the laser spot was illuminating surfaces of both cameras. Then the cameras were translated back the same distance from the center, as controlled by the scales on the stages. Laser beam was nearly normally incident on the glass plate. This was achieved by rotating the rotary stage in small increments, while observing the spot of the reflected beam on the laser's front surface. When the spot was coincident with the original beam, i.e. no visible mark of the reflected beam was perceived; the position of the rotary stage was noticed. This position was assumed to be the origin and served as a reference for further rotations. The rotary table was spun 45° to split the laser beam into two inter-perpendicular components, transmitted and reflected. Incidence spot of the reflected beam on the pinhole collimator was observed and the detector assembly was adjusted such that the spot coincided with the pinhole opening. The glass slab was rotated to - 45° position from the origin and the alignment process was repeated with the second camera in a pair. The gantry was then rotated 90° and the same procedure were reiterated with the second detector pair.

4.2.2.2 Alignment of the X-ray Source and Detectors

Big Chip detector was mounted on an aluminum plate, which in turn was attached to the supporting profile structure. Moving the plate along the profile grooves controlled the source-to-detector distance and was not a part of the alignment process. Support structure was designed to permit adjustment of the detector position along and perpendicular to the AOR. Hamamatsu detector was mounted in front of the Big Chip's entrance window with a slotted aluminum. The slots are perpendicular to the AOR and allow for position correction. The alignment of the x-ray system was carried out by first aligning the detectors with the AOR and then adjusting the focal spot projection with center of the detector. First step was very similar to aligning gamma cameras. It was further simplified by the fact that the axial location of the detector's centers could be chosen arbitrarily. To align detectors with the AOR we identified the central line on the detector's entrance windows that was parallel to the direction of the AOR. At this point no detector angular deflections were taken into account. The central line was used as a target location of the reflected laser beam. The reflected beam was obtained in the same manner as during the gamma system alignment. By moving the detectors, reflected beam was forced to intersect the central line. At this point the detectors' positions were rigidly fixed. In order to align the x-ray source, a parallel collimator was used. The collimator was fabricated out of tungsten polymer compound by Mikro Systems. The length of the collimator holes was 30 mm, hexagonal shape hole diagonal - 0.4 mm and thickness of the septa was 0.1 mm. The back surface of the collimator was machined to be flat within the regular accuracy of machining to ensure the normal incidence of incoming x-rays. The collimator was placed on the entrance window of the detector and an x-ray image

was taken. A sample image is shown in the Fig. 4.14. The image was then analyzed in order to calculate the amount of necessary adjustments. First, the image was binarized with the user-selected image count threshold. This was done to remove the effect of the residual image noise on the calculations. Then, two-dimensional center of gravity (COG) of the image was calculated using the image matrix as 2-D Cartesian coordinate system. The value of the COG was compared to the coordinates of the center of the detector and magnitudes and directions of shifts were derived. This method was tested to achieve the alignment precisions of about 0.5 mm, and was limited by the human accuracy of performing the shifts. The way of achieving greater accuracy would be to mount the x-ray source on the translation stages. But as will be shown in the following subchapter, there was no benefit in such complications.

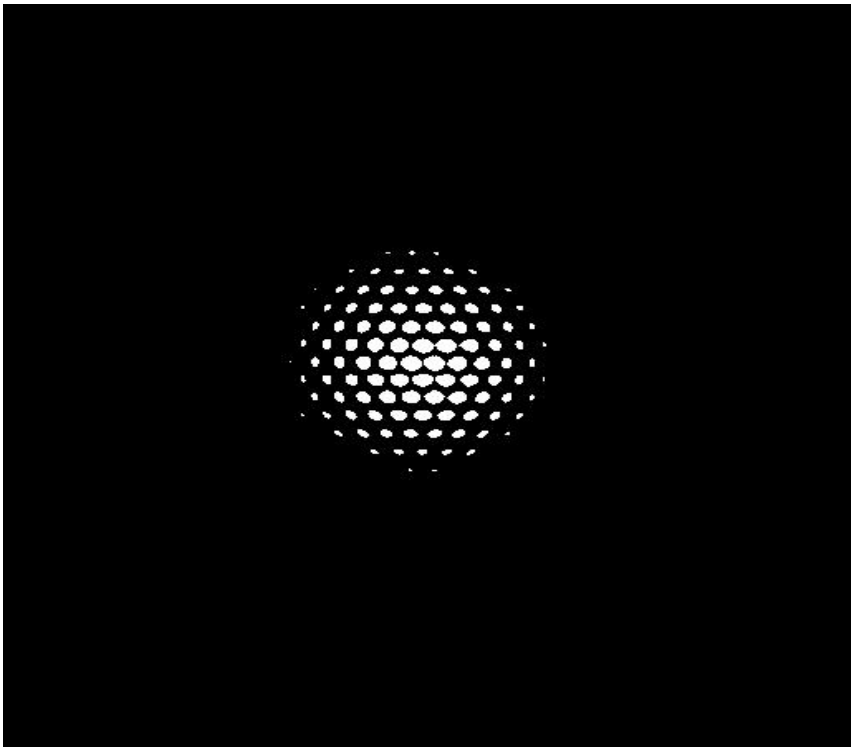

Fig. 4.14.*Image of the focal spot on the Big Chip detector through a parallel-hole collimator*

4.3 System Final Calibration

For alignment of the animal bed supports, two cylindrical holders for capillary tubes were manufactured. The diameters of the holders match exactly the inner diameters of the bed supports. Filling up a capillary with radioactive solution, inserting a filled capillary into the holders and placing the holders inside the bed supports allows a radioactive line source to be positioned along the AOR for imaging.

So far, it was proven that an imaged object stayed in the scanner field-of-view over a full revolution of the gantry due to the achieved sub-millimeter alignment accuracy. However, reconstructed images exhibited artifacts associated with small imperfections of the geometrical depiction. A common approach to this problem is to try to quantify the geometry of the system and then use the correct geometry in the reconstruction process. Several methods were developed over the years for CT and SPECT modalities [2],[4]-[7]. Although both modalities are utilizing cone-beam acquisition geometry, the difference between emission and transmission modes cannot be easily overcome. Therefore final calibrations of the subsystems were performed using different methods and will be described separately.

4.3.1 Calibration of the CT subsystem

Most calibration procedures assume perfectly rigid geometry of the imaging system. While it is a relatively safe assumption to make for gamma-ray imaging due to inherently lower spatial resolution, the performance of CT part will suffer from displacements of components as little as 50 μm. Therefore we opted for the approach

developed by the Exxim Computing Corp, the company that designed CT reconstruction code used in our scanner. Their approach takes into account possible gantry wobbles and components shifts due to gravity. The only assumption made is that those displacements are reproducible from scan to scan, so that the calibration parameters could be used in later studies provided that the geometric arrangement was not altered.

To make use of the calibration procedure several phantoms were designed. They are shown in Fig. 4.15. Each phantom consisted of a Plexiglas tube with steel balls embedded into its surface. The balls were arranged in three or four circles, each circle containing 8 equidistantly spaced balls. Distance between the circles was chosen such that all the balls would be within the field-of-view of the x-ray detectors at all times. Phantom diameters were 1.5, 1 and 0.55 inches. First two phantoms were intended to be used with rat and mouse size table supports respectively, while the last one finds its application with a rotation stage CT setup.

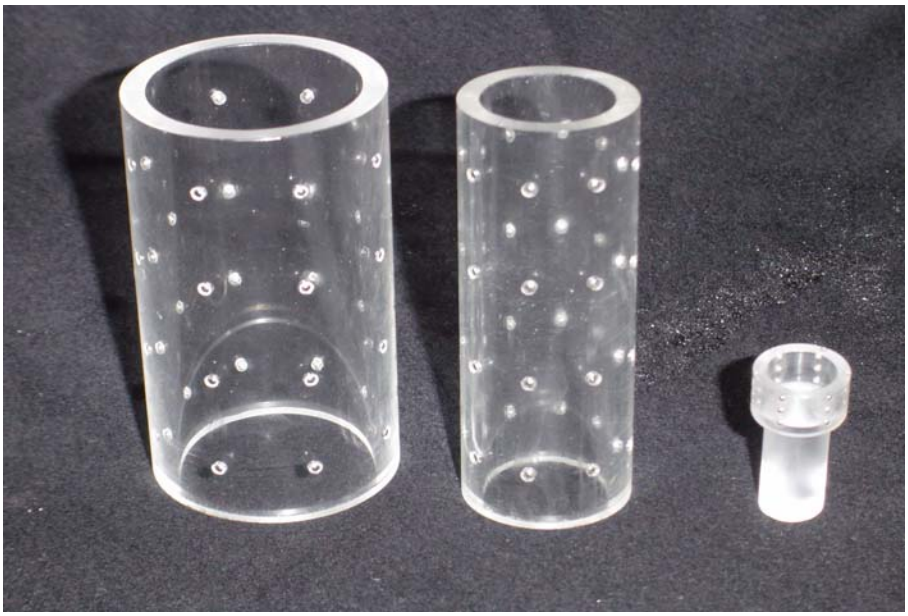

Fig.4.15.*CT calibration phantoms line-up*

Initial step of the calibration procedure included an acquisition of the CT data set of the calibration phantom. After an acquisition had been completed data was reconstructed using “best guess” parameters. Physical characteristics of the phantom such as diameter, ball rings spacing, and numbers of balls per ring were entered into the calibration software. Reconstructed image was then loaded into a slice viewing application and 3-D center of gravity of each ball’s image was calculated and stored. Knowing phantom geometry and centers of gravity the software algorithm made a prediction as to the position of the center of each ball in each projection image. The predicted position appears as a movable colored cross overlaid on top of grey scale projection image. The crosses were then moved to the actual position of the ball centers by either software means or manually. This approach allowed for every projection to be calibrated, but since CT data sets usually contain hundreds of frames, the process was repeated for every 15-th frame with interpolations made for the frames in between. After all the chosen projections were processed, program calculated the calibration parameters by minimizing the difference between predicted and actual locations of the ball’s centers as a function of detector tilt and twist angles, magnification factor, central ray offset from the center of the detector and absolute angular positions. Accuracy of minimization result was reported as an average minimized difference over the whole set of chosen projections. Typical value for the difference was found to be 2.5 pixels, which translated to about 12 to 50 μm depending on the choice of the detector and magnification factor. After the result was approved by a user, binary files containing calibration values were saved for subsequent use. Fig. 4.16 represents a slice of the reconstructed data set before and after the final calibration.

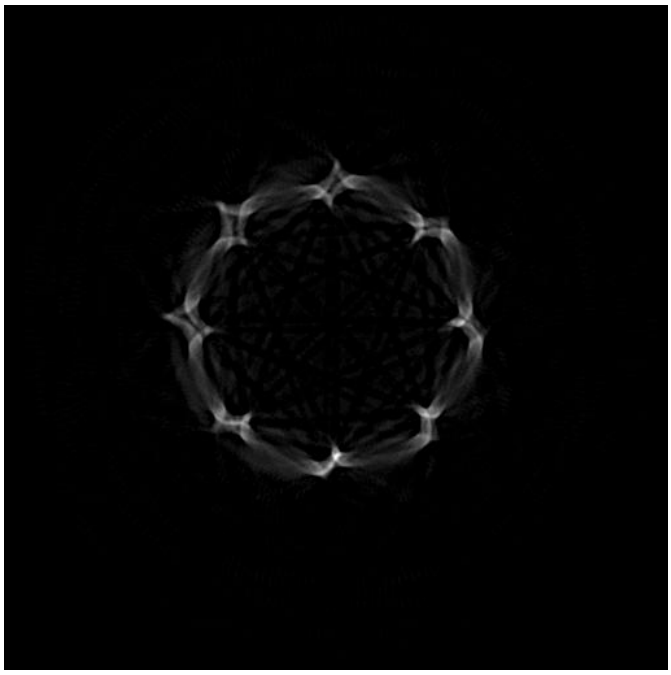

(a)

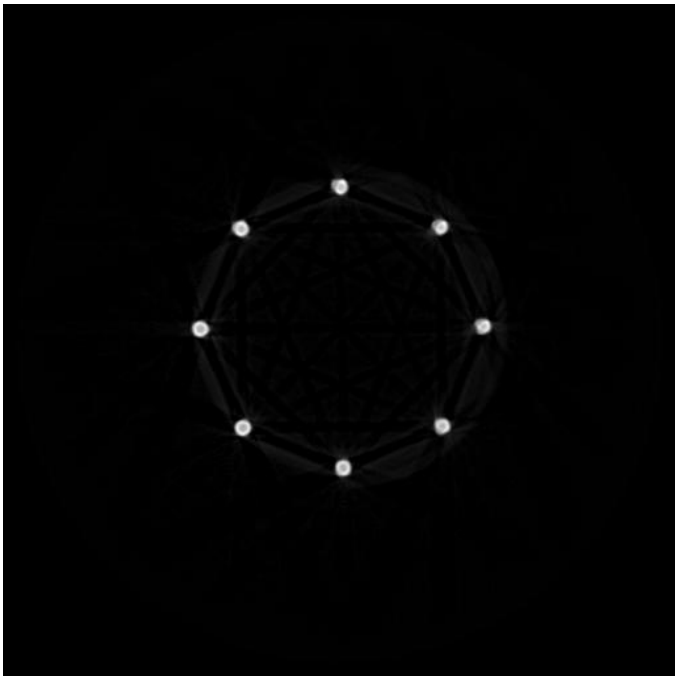

(b)

Fig.4.16.*Trans-axial slice through the reconstructed volume (a) before and (b) after the final calibration*

4.3.2 Calibration of the SPECT subsystem

An attempt of general characterization of pinhole SPECT acquisition geometry was undertaken using a method introduced in [8]. Method relies on obtaining projections of a collection of point sources located at known distances from each other. Location of a centroid of each point source's image at each angular position is recorded. When plotted on XY plot, centroid locations of each source trace an ellipse, as shown in Fig. 4.17.

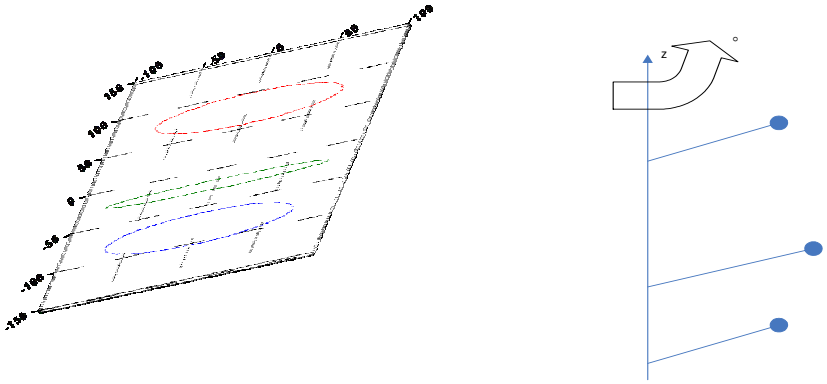

Fig.4.17.*Three point sources phantom and projection ellipses*

If the distance between point sources and an angular step of scanning are known, then locations of projections of point sources can be derived analytically using seven geometrical parameters described at the beginning of section 4.2. Comparing projection data with the analytical model seven geometrical parameters can be estimated. Estimation is performed as minimization of a following cost function

$$F = \sum_i \sum_j ((u_{ij}^{img} - u_{ij}^{est})^2 + (v_{ij}^{img} - v_{ij}^{est})^2) \qquad (4.13)$$

where u and v are coordinates measured on the detector surface, superscripts *img* and *est* denote measured and analytically calculated coordinates. The cost function was minimized by searching the 16-dimensional space (7 geometrical parameters and three-

dimensional coordinates of each of three point sources). Three point sources, located on a specially designed phantom, were scanned every 3 degrees over a full revolution of the gantry. Unfortunately we were not successful in parameter estimation. Algorithm converged on a solution that was physically unrealizable. Parameter e_v, electronic shift along a detector column, was estimated to be 94 mm, which is almost the size of the detector. Our suspicion was that the algorithm kept finding local minima of the estimate function because of high degree of parameter correlation. The process was repeated for three different data sets and did not yield satisfactory results.

We are currently looking for other ways of obtaining geometrical parameters, but at this point a failure has to be reported. We can reliably estimate one parameter out of seven, namely mechanical shift m, by a different method. Our results show that this parameter plays the most important role in successful data reconstruction, as will be shown in chapter 5. Search for a reliable method of parameter estimation is at the top of future improvements of the scanner.

References

[1] Rizo Ph., Grangeat P., Guillemaud R.,*"Geometric calibration method for multiple-head cone-beam SPECT system,"* IEEE Trans. Nucl. Sci., vol. 41, pp. 2748–2757, 1994

[2] Noo F., Clackdoyle R., Mennessier C., White T.A., Roney T.J., "Analytic method based on identification of ellipse parameters for scanner calibration in cone-beam tomography," Phys. Med. Biol., vol. 45, pp. 3489–3508, 2000

[3] Metzler S. D., Greer K. L., Bobkov K., Jaszczak R. J., "Laser alignment system for helical pinhole SPECT",I EEE Trans. Nucl. Sci., vol. 51, no. 3, June 2004

[4] Kyriakopoulos K.J., Yiannakos P., Kallipolites V., Domales K., *"A geometric calibration methodology for single-head cone-beam X-ray systems,"* J. Intelligent Robot. Syst., vol. 24, pp. 151–174, 1999

[5] Bronnikov A.V., "Virtual alignment of X-ray cone-beam tomography system using two calibration aperture measurements," Opt. Eng., vol.38, no. 2, pp. 381–386, 1999

[6] Gullberg G.T., Tsui B.M.W., Crawford C.R., Ballard J.G., Hagius J.T., "Estimation of geometrical parameters and collimator evaluation for cone beam tomography," Med. Phys., vol. 17(2), pp. 264–272, 1990

[7] Bequ´e D., Nuyts J., Bormans G., Suetens P., Dupont P., *"Characterization of pinhole SPECT acquisition geometry,"* IEEE Trans. Med. Imag., vol. 22, issue 5, pp. 599 – 612, May 2003

[8] Bequ´e D., Nuyts J., Bormans G., Suetens P., Dupont P., *"Optimization of pinhole SPECT calibration,"* 2003 IEEE Nucl. Sci. Symp. Conf. Rec., vol. 4, pp. 2343 – 2347, 19-25 Oct. 2003

CHAPTER 5
CT, SPECT and dual modality imaging

This chapter covers final steps of the scanner design and presents results of tomographic scans. At this point components have been tested, installed and aligned on the gantry, final calibrations performed, so next stage of the scanner construction is to acquire tomographic data and obtain volumetric reconstruction – the ultimate goal of tomographic imaging. Once the volumes are reconstructed, data from different modalities need to be presented simultaneously to reveal both functional and anatomical information.

5.1 X-ray CT

X-ray CT system can be operated in two modes depending on the object to be scanned. We usually utilize Hamamatsu detector for in vivo experiments with live animals and Big Chip detector for scanning of extracted samples. Big Chip is used in combination with Kevex source to preserve high spatial resolution. Choice of an x-ray tube for Hamamatsu detector is dictated by animal size. Larger animals like rats are usually scanned with Source-Ray source, while for much less attenuating mice Kevex source is employed.

5.1.1 Live animal imaging

Both detectors are mounted on the gantry, with CMOS flat panel array attached to the front of CCD detector. Distance between a source and a detector is limited by Big Chip's physical dimension. In order to avoid collision between detector cooling lines and gantry structure source-to-detector distance is fixed to 300 mm for Hamamatsu and 315 mm for Big Chip. Source-to-AOR distance is set 240 mm yielding magnification factor of 1.25 for flat panel setup. In order to test spatial resolution of the system at this particular magnification factor images of a bar pattern were taken with both detectors and Kevex source. Bar pattern consists of series of equally spaced low attenuation bars on a high attenuation material substrate. Each bar series contains 5 bars of equal width spaced by a region of substrate material. Bar series range in frequency from 5 to 20 line pairs per millimeter. Image of a bar pattern was inspected visually to find maximum frequency at which all five bars can be distinguished. Ten perpendicular profiles through the identified pattern were taken and contrast transfer value was calculated as:

$$CT(f) = \frac{T_{\max}(f) - T_{\min}(f)}{T_{\max}(f) + T_{\min}(f)} \tag{5.1}$$

where $T_{min}(f)$ and $T_{max}(f)$ are minimum and maximum transmission values in the analyzed pattern. In general one can measure constant transfer values for each frequency in the bar pattern and construct contrast transfer function (CTF). This function is used sometimes instead of MTF to describe system spatial resolution. Weakness of CTF description of spatial resolution resides in the fact that bar patterns are essentially series

of delta-functions in frequency space. Delta functions do not form a basis in frequency or any other space hence can not be used to represent arbitrary input continuous function. But knowing CTF value at a particular frequency it is possible to calculate an MTF value at that frequency using formula [1],[2]:

$$MTF(f) = \frac{\pi}{4}(CTF(f) + \frac{CTF(3f)}{3} - \frac{CTF(5f)}{5} + \frac{CTF(7f)}{7} - \frac{CTF(11f)}{11} \ldots \quad (5.2)$$

Each frequency argument should be cut-off not to exceed Nyquist frequency. Fig.5.1 and 5.2 show bar pattern images taken with Hamamatsu and Big Chip detectors respectively.

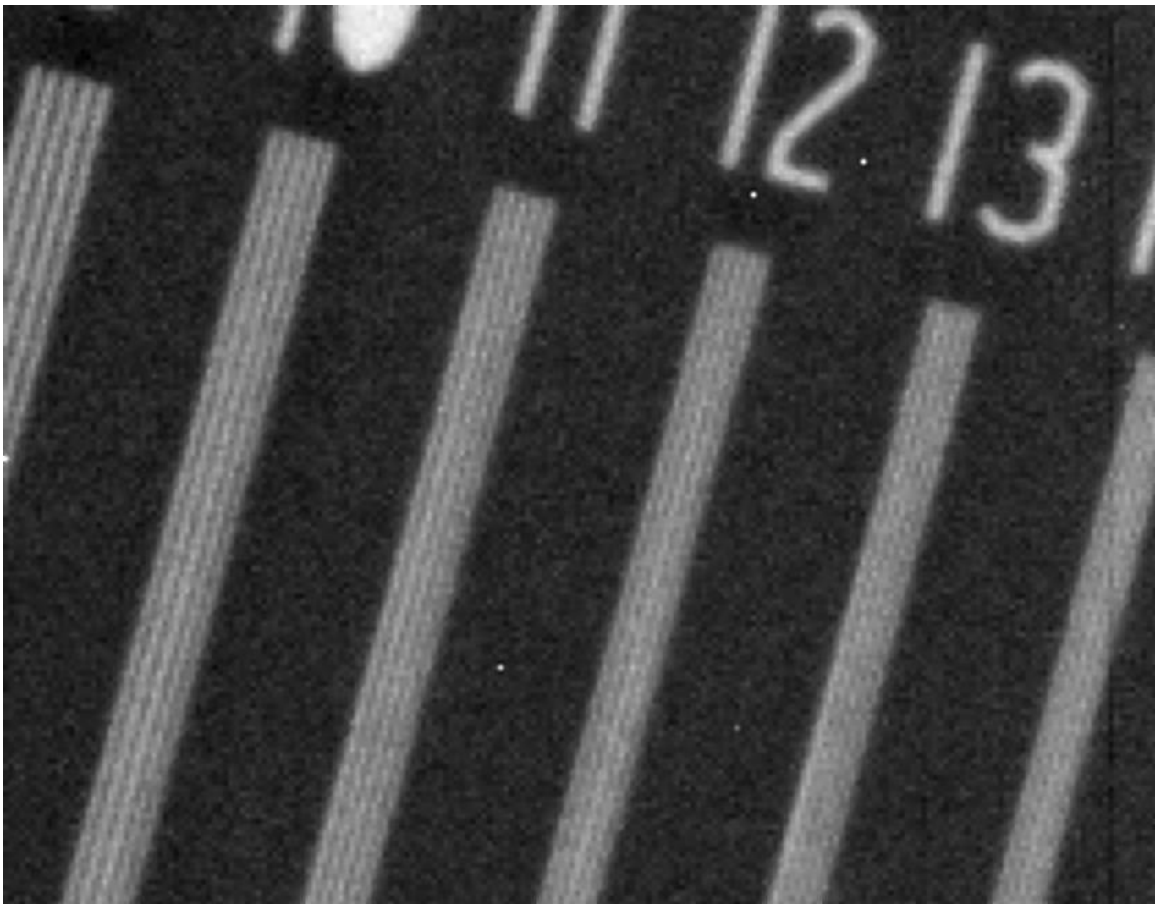

Fig.5.1.*Bar pattern image, Hamamatsu detector, magnification 1.25. Image was cropped to show detail. Window and level were optimized for viewing. No image processing was performed.*

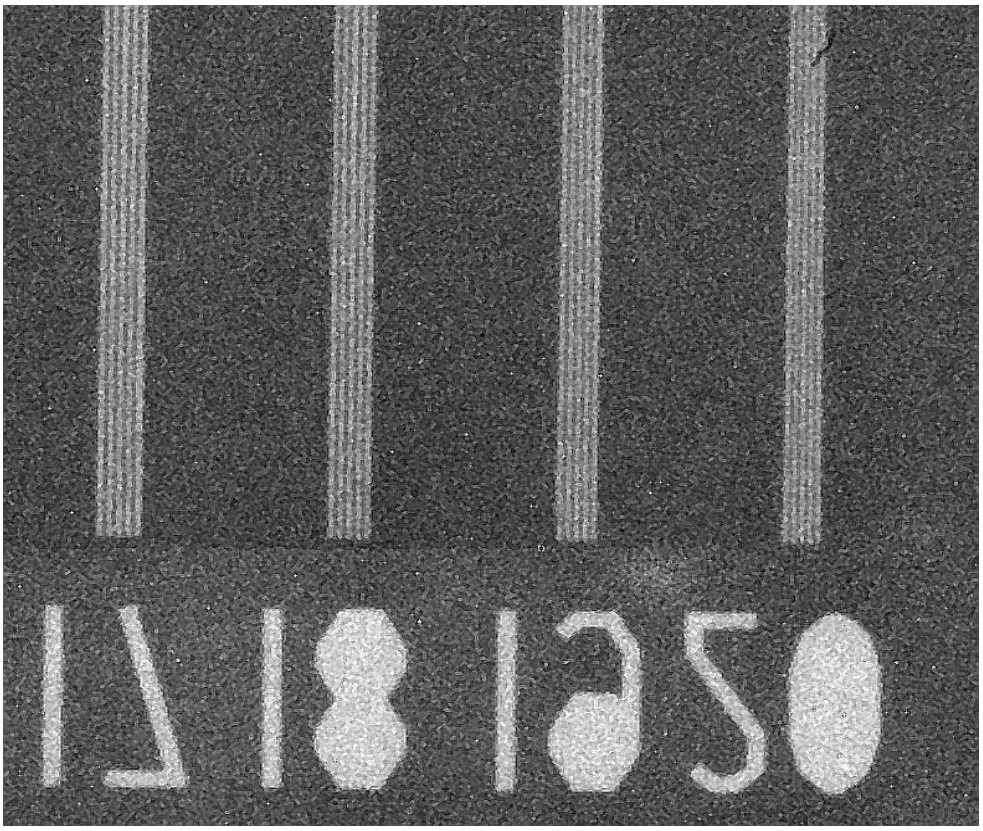

Fig.5.2.Bar pattern image, Big Chip detector, magnification 1.32. Image was cropped to show detail. Window and level were optimized for viewing. No image processing was performed

These images were taken with a bar pattern located at the axis of rotation of the gantry. A rectangular region of interest was selected in between bar patterns and average pixel value was calculated to estimate background level. Transmission values were calculated by subtracting background count from 5 peak and 4 valley counts in the bar pattern. CTF value was calculated using formula (5.1) for each profile and averaged across ten profiles taken. Fig.5.3 and 5.4 exhibit profiles taken through Hamamatsu and Big Chip images respectively.

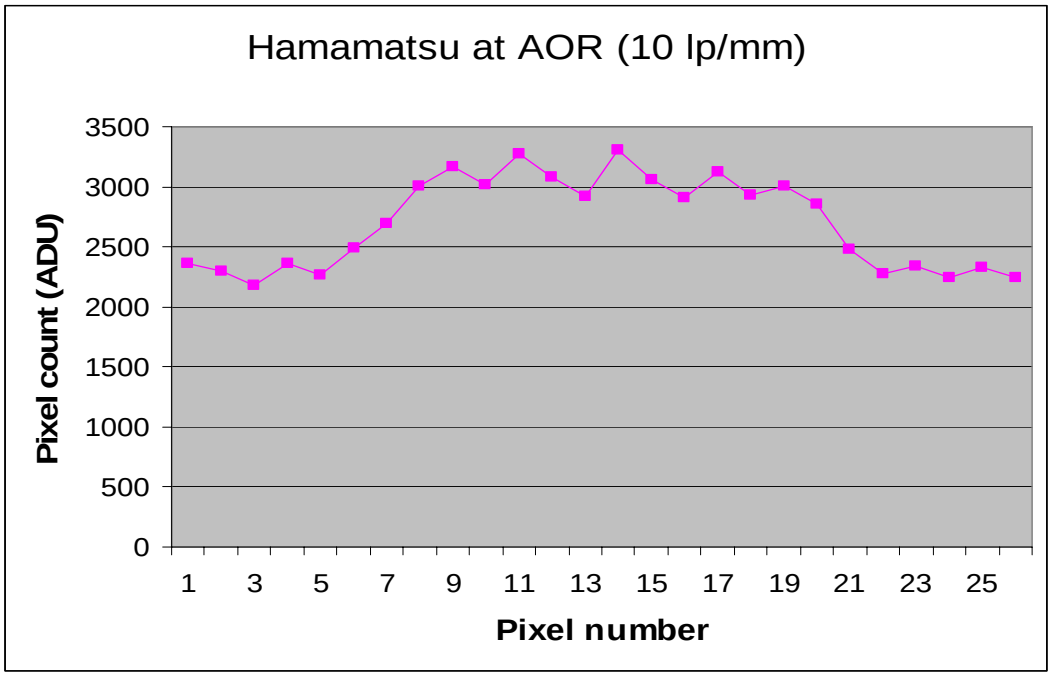

Fig. 5.3.*Profile through 10 lp/mm bar pattern, Hamamatsu detector*

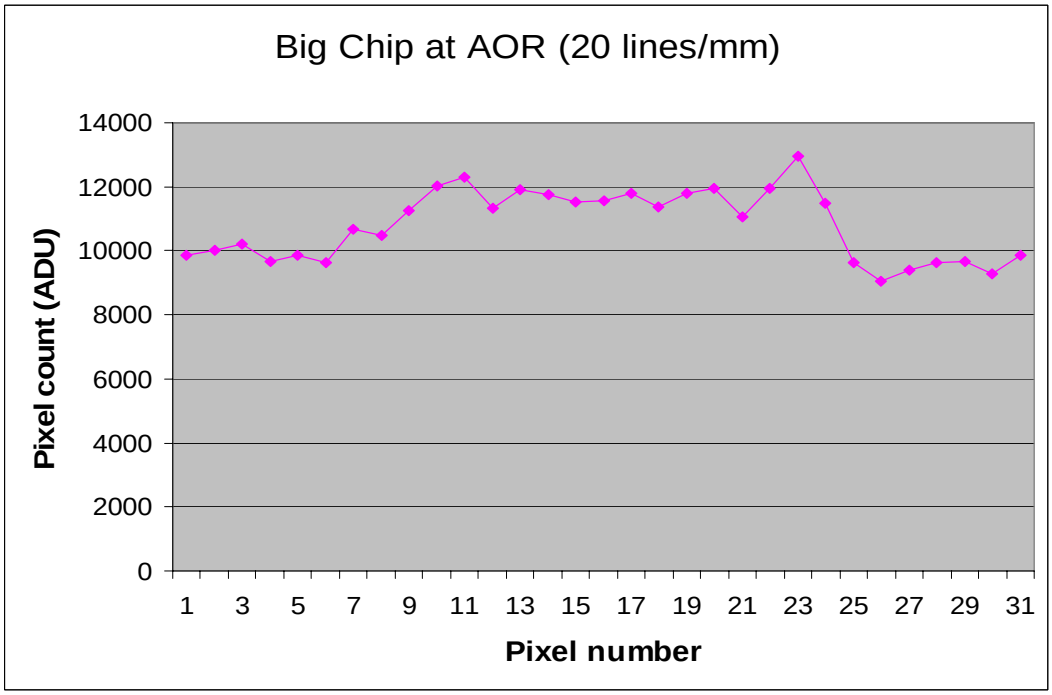

Fig. 5.4.*Profile through 20 lp/mm bar pattern, Big Chip detector*

CTF values for flat panel detector at 10 lp/mm and Big Chip at 20 lp/mm were calculated to be 0.062 and 0.21 respectively. Using (5.2) it was determined that MTF value at 10 lp/mm for Hamamatsu was 4.9 %, while a 20 lp/mm MTF value for Big Chip was 16.3 %.

A trial mouse scan was performed using Hamamatsu detector and Source-Ray x-ray source. A total of 360 frames were acquired equally spaced over 360 degrees. Detector was binned down by a factor of 2 to increase readout speed. Detector integration time was 0.75 seconds with 0.5 seconds of x-ray exposure at 40 kVp and 0.5 mA. Total scan time to obtain full set of projections took 4.5 minutes. Projection images were corrected for dark offset and flat-field non-uniformities using pre-acquired correction images. Corrected data was reconstructed using Feldkamp-type [3] reconstruction algorithm, implemented by Exxim Computing Corp (Pleasantville, CA). Reconstruction volume consisted of 512 x 512 x 512 array of 160 microns isotropic volume elements. Axial, coronal and saggital slices are shown in Fig.5.5. First “commercial” utilization of our scanner was made by Dr Haixiang Liang of UVa Orthopedic Surgery Research Center. Dr Liang studies methods of bone regeneration by implanting various substances into scooped out regions of rat spinal cord and tracking bone growth over time. Two 150 grams rats were scanned using CMOS detector and Source-Ray x-ray source. 220 views were acquired over 220 degrees of total scan angle. Detector integration time was 2 seconds with 1.5 seconds of x-ray exposure at 50 kVp and 0.6 mA in both cases. Data acquisition took 7.3 minutes per rat. Reconstruction volumes were cubes of 512 voxels in each dimension. 80 micron voxel size was the same for both scans. Slices through reconstructed volumes are presented in Fig. 5.6 and 5.7.

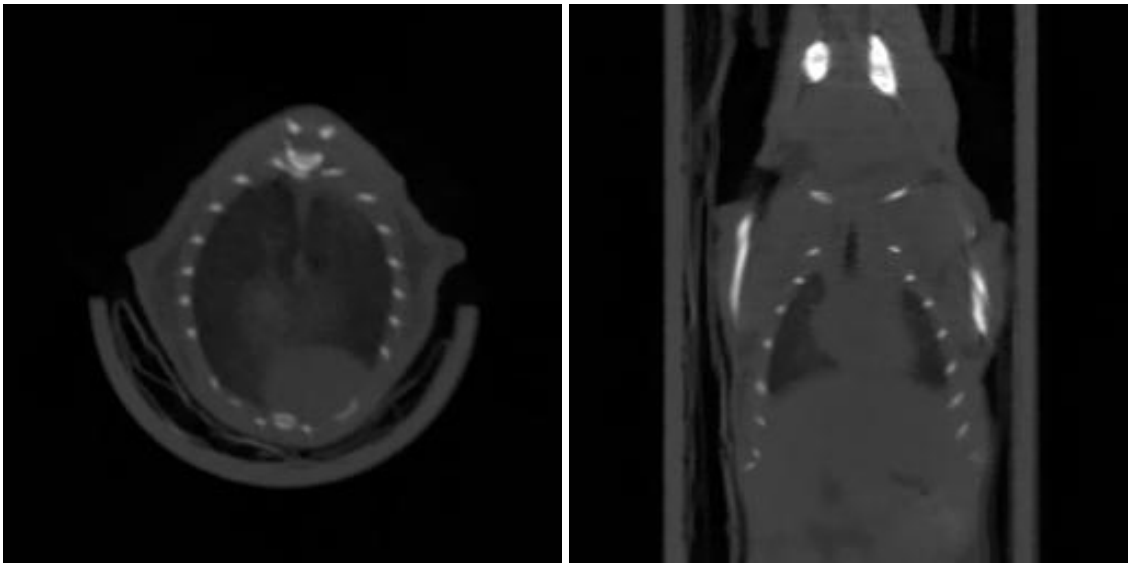

(a) (b)

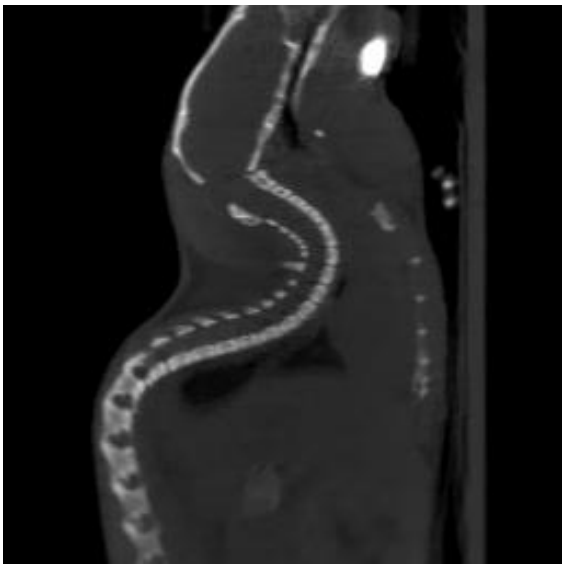

(c)

Fig. 5.5.*Axial (a), coronal (b) and saggital (c) slice through the mouse reconstructed volume*

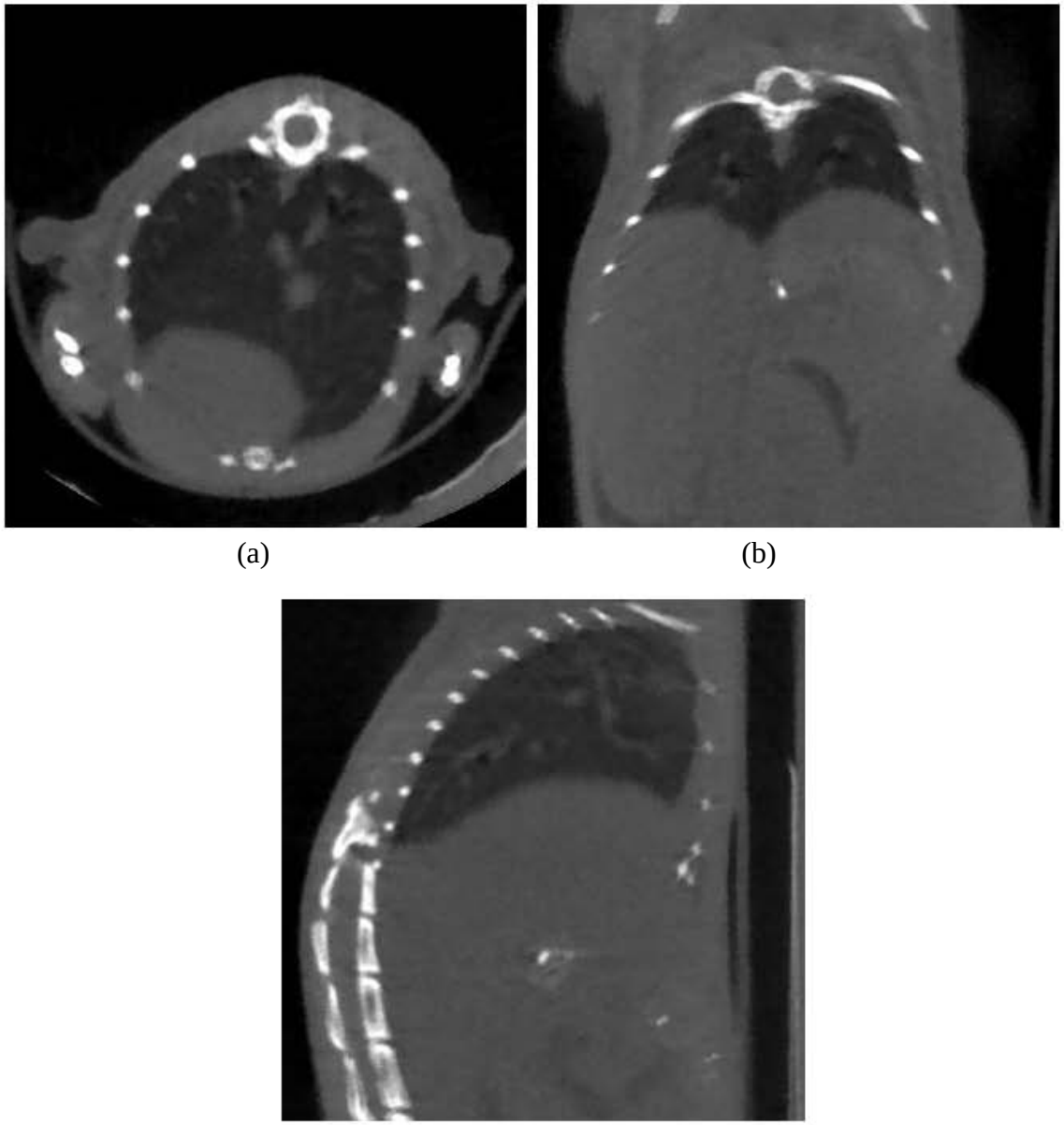

(a) (b)

(c)

Fig.5.6.*Axial (a), coronal (b) and saggital (c) slices of a healthy rat CT data*

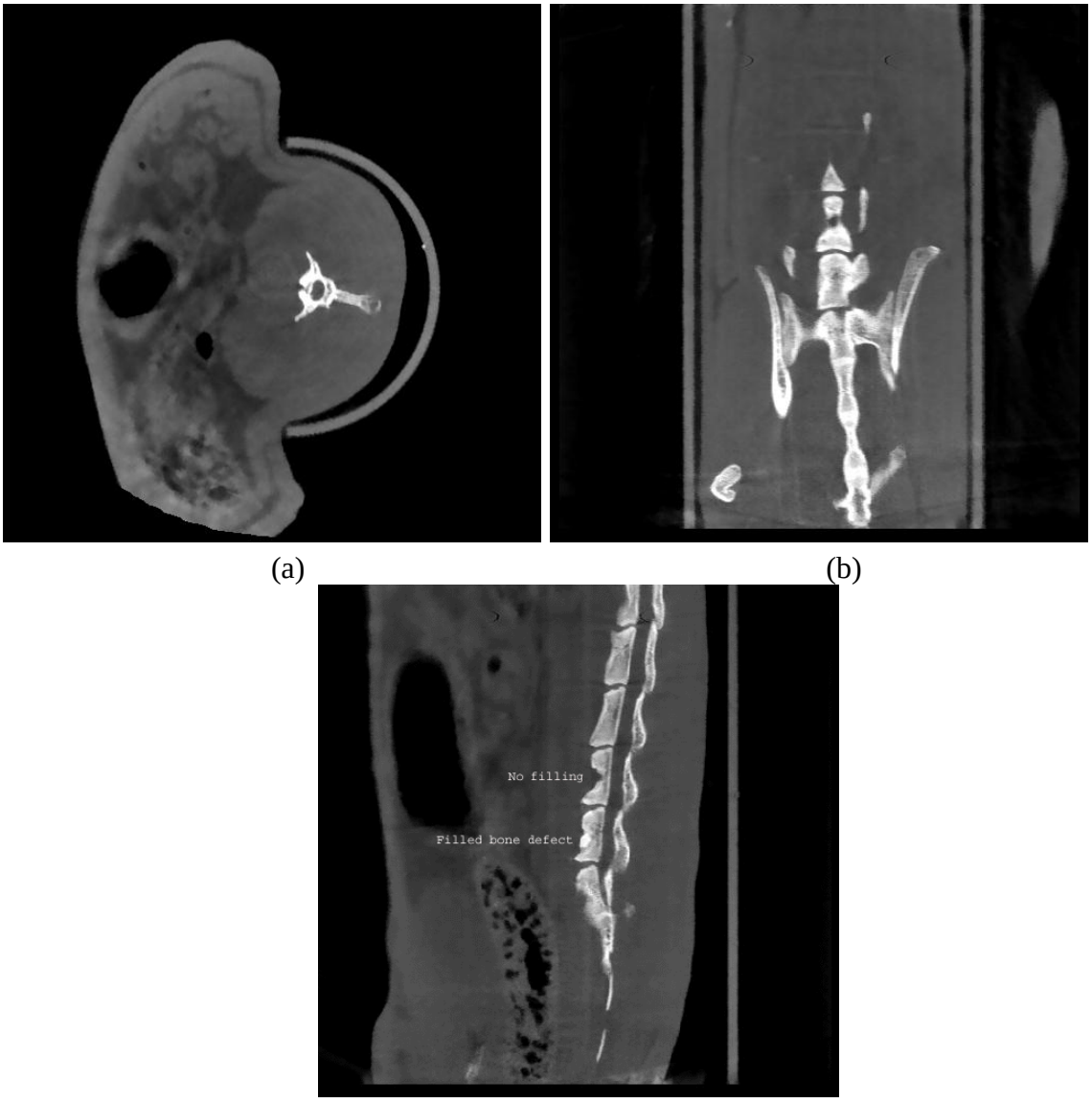

(a) (b)

(c)

Fig.5.7.*Axial (a), coronal (b) and saggital (c) slices through a rat with two bone defects. Saggital slice clearly shows two effected areas.*

5.1.2 Imaging of extracted samples

Imaging of extracted samples require high magnification factor to increase spatial resolution of the system. Gantry geometry and Big Chip detector size do not allow increasing source to detector distance significantly. But because of flexibility offered by gantry design, it is possible to mount a rotation stage between a source and a detector. We utilized motor-driven rotary table model A4818S from Velmex Inc (Bloomfield, NY). This rotary stage features a stepper motor with resolution of 400 steps/rev coupled to a rotating table through a gear with 18:1 gear ratio for a total resolution of 7200 steps/rev. An aluminum plate with a threaded hole in the center is mounted on the rotating surface of the table. An aluminum cylinder with threaded stud at one end and a drilled along cylinder's axis at the other end acts as a sample holder. Samples are usually provided in a plastic container with diameter matching that of a hole in sample holder.

To test resolution of the system at highest achievable magnification factor of ~ 7, images of bar pattern were taken and analyzed as described in section 5.1.1. Images of bar pattern for Hamamatsu and Big Chip detectors are shown in Fig. 5.8 and 5.9. Slices through maximum resolvable frequency pattern for both detectors are shown in Fig. 5.10 and 5.11. Both detectors were able to resolve 20 lp/mm bars. Values of modulation transfer function at 20 lp/mm were calculated to be 24.5 % for Hamamatsu detector and 57.9 % for Big Chip detector.

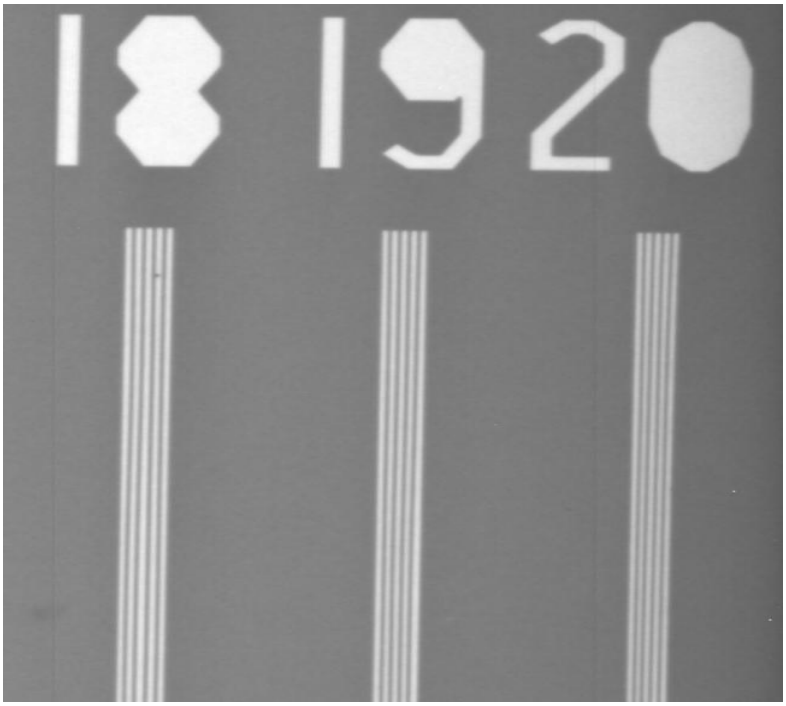

Fig. 5.8.*Bar pattern image Hamamatsu detector, magnification 7.2*

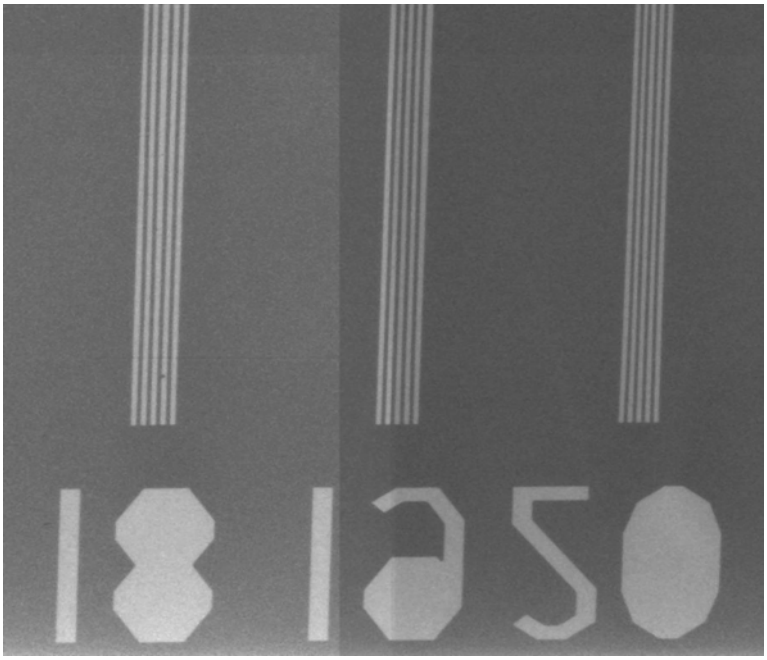

Fig. 5.9.*Bar pattern image Big Chip detector, magnification 7.3*

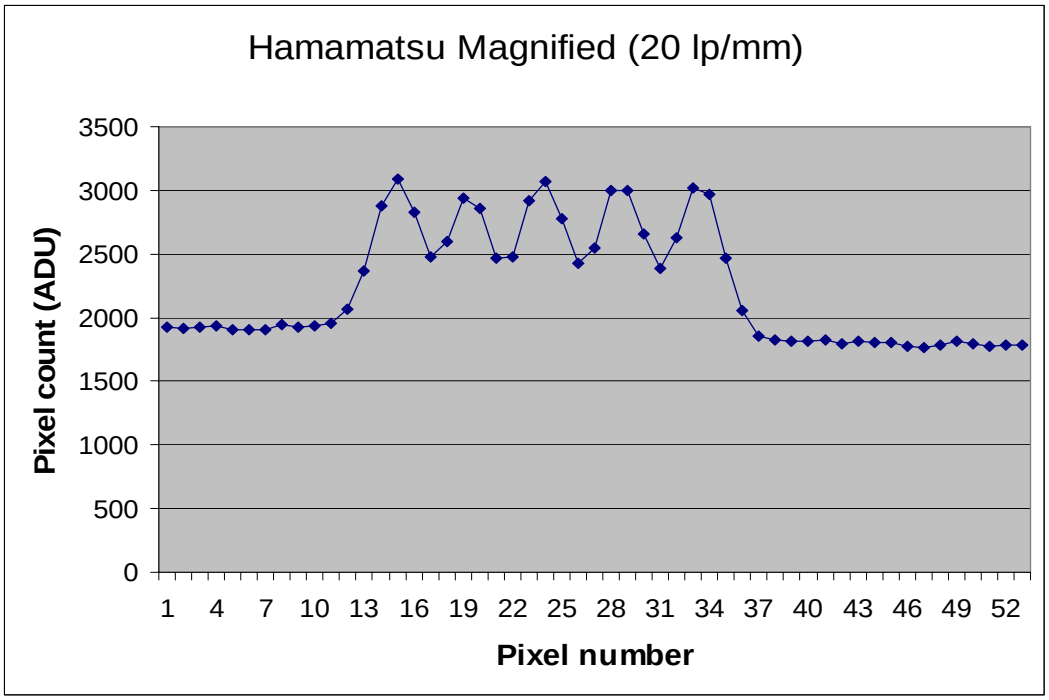

Fig.5.10.*Profile through 20 lp/mm bar pattern Hamamatsu detector, magnification 7.2*

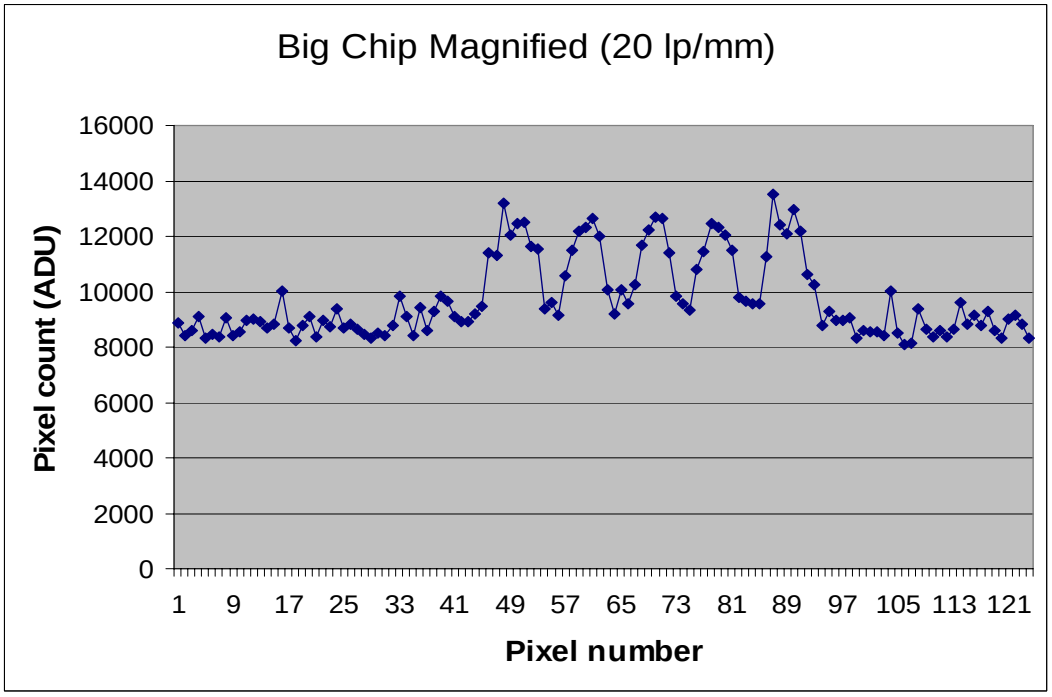

Fig.5.11.*Profile through 20 lp/mm bar pattern Big Chip detector, magnification 7.3*

An extracted mouse heart filled with radio-opaque polymer was scanned with Big Chip detector and Kevex source using magnification factor of 5. Data was reconstructed

as a cube of 512 x 512 x 512 voxels with voxel size of 19 microns. Slices are shown in Fig. 5.12.

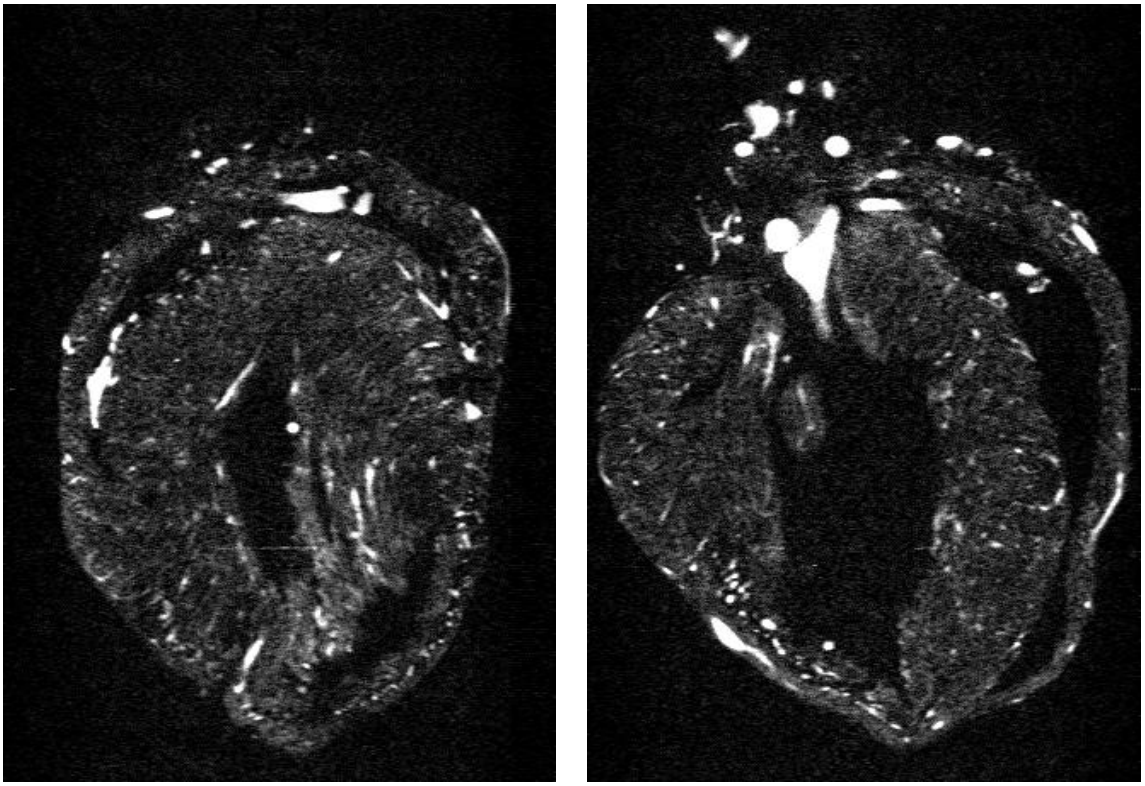

(a) (b)

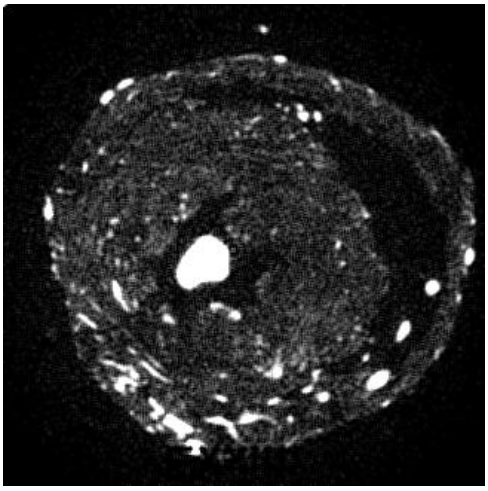

(c)

Fig.5.12.*Coronal (a), saggital (b) and axial (c) slices through heart reconstruction*

A single lobe of extracted mouse lungs perfused with CT contrast agent was imaged using Big Chip detector at magnification factor of 3. Reconstructed voxel size was 32 microns for a volume of 512 voxels cube. Slices are shown in Fig. 5.13.

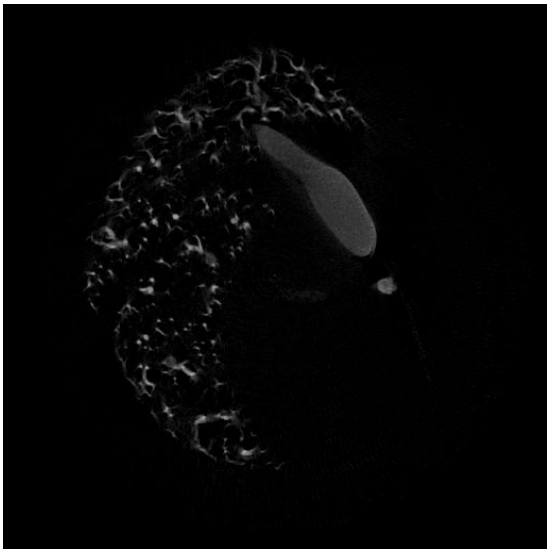

(a)

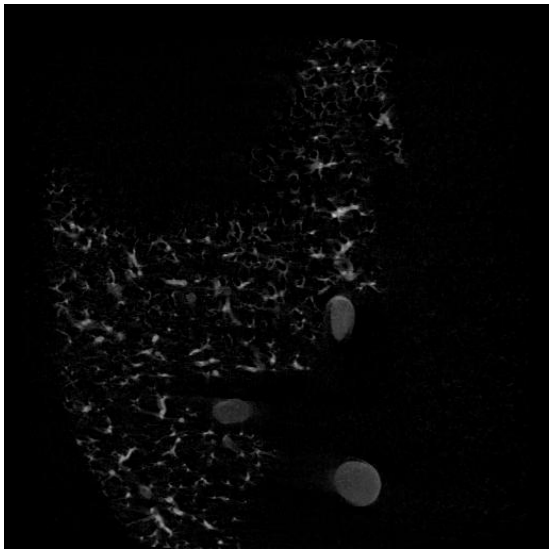

(b)

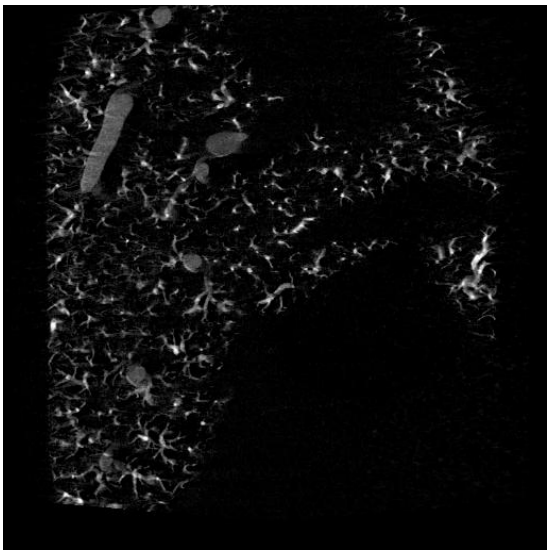

(c)

Fig. 5.13.*Axial (a), coronal (b) and saggital (c) slices through reconstructed lung volume*

Both reconstructions look to be free from significant artifacts. No analysis was performed on these images, since both scans were viewed as a feasibility study by investigators.

5.2 SPECT scanning

SPECT scanning can be realized using either full- or half-cone geometry. For half-cone geometry gamma detectors are equipped with pinhole collimators with a fixed focal length of 118 mm. The focal length was chosen so that output pyramid of square pinhole inserts with full opening angle of 45 degrees covers all the area of the detector. Tungsten polymer square pinholes of knife and channel types with side lengths of 0.5, 0.75 and 1 mm are inserted into a seating place on top of the collimator holder and secured with aluminum fixture. Pinhole in a seating place and fully assembled collimator are shown in Fig.5.14.

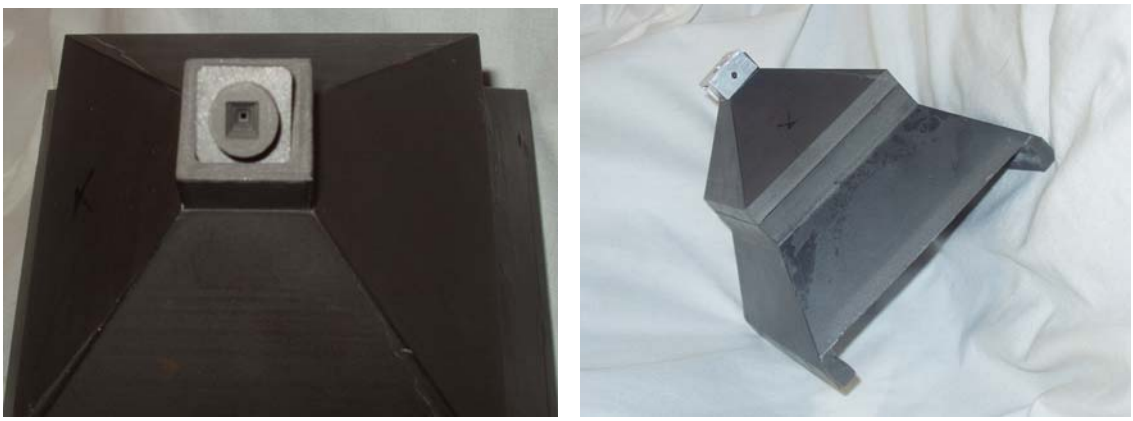

Fig.5.14.*Photograph of an unsecured pinhole insert and assembled collimator*

Pinhole collimators with a focal length of 84 mm are used for a full-cone geometry realization. They utilize conventional round pinholes with opening angle of 90 degrees

and diameters ranging from 0.5 to 3 mm. Both type of collimators slide along guiding rails of detector housing and secured with set screws.

Arrangement of detectors for half-cone geometry is shown in Fig.5.15.

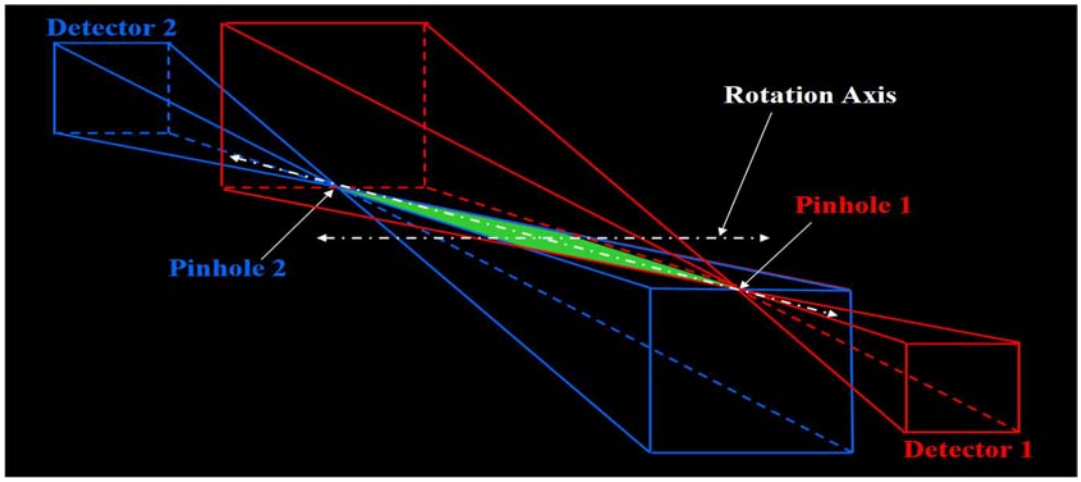

(a)

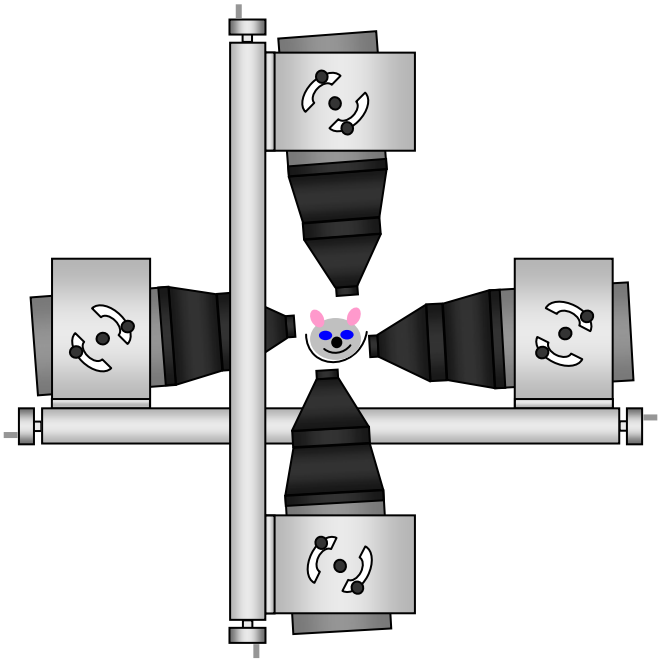

(b)

Fig.5.15.*Diagram of side view of mounting of one camera pair (a), showing combined field of view in green, and a view along the AOR of four-camera assembly (b).*

Pairs of cameras are offset axially to provide necessary coverage in the axial direction. Since detector 4 is not functional at the moment all results shown below were obtained with only one camera pair.

Half-cone acquisition geometry was realized in a following manner. A capillary filled with solution of Tc-99m was placed in a holder that fits snuggly into an animal bed support. Gamma cameras are translated toward AOR to a closest possible separation between tips of the collimators and animal bed support. Since animal bed support is aligned with the AOR and collimator field of view covers the whole detector area, it is sufficient to rotate cameras around the central bolt of their mountings to bring projection of the capillary to the last row of the detector matrix. Cameras in a pair are rotated in opposite directions as was designed in their mounting structures.

5.2.1 Phantom imaging

Imaging of a microSPECT phantom was performed in order to assess system performance. The phantom, shown in Fig. 5.16, is a hollow acrylic cylinder with an outer diameter of 30 mm and a cylindrical acrylic insert. A series of holes ranging in diameter from 1.2 to 1.7 mm were drilled along the symmetry axis. The holes form six sectors containing 6 to 10 holes of the same diameter and with a center-to-center spacing equal to twice the hole diameter. The combined volume of the holes is about 40% of the total open volume of the phantom, with the rest of the open volume contained in two disk-shaped regions at the ends of the phantom. There are two filling holes located at one end of the phantom. The phantom was filled with Tc-99m solution with activities of 5 mCi, so approximately 2 mCi was present in the holes.

Fig. 5.16.*Photographs of microSPECT phantom*

In full-cone acquisition geometry the phantom was positioned with its axis approximately aligned with the axis of rotation of the gantry and 31 mm away from the 1.0 mm tungsten pinhole collimator, resulting in a magnification factor of ~ 3 at the axis of rotation. Total of 120 frames equally spaced over 360 degrees were acquired. The acquisition time for the first frame was at 30 seconds, with the frame acquisition time of subsequent frames corrected for the decay of the radioisotope. This resulted in a total acquisition time of 67 minutes.

In half-cone geometry cameras were positioned 24 mm away from the AOR, measured before tilting the cameras into final position. Tilt angle of the cameras was controlled by observing location of the projection of a capillary positioned at the AOR. Tungsten polymer square pinhole insert 0.75 mm side length was used. Total of 60 views per camera over 180 degrees of per camera scan angle were collected. Frame acquisition time was set to 30 seconds with subsequent decay correction after first frame.

SPECT data were reconstructed using an OSEM algorithm [4], implemented by our collaborator Dr Yibin Zheng, assistant professor of Department of Electrical and Computer Engineering at UVa. Reconstruction program assumes perfect system geometry except for mechanical shift m, described in chapter 4. Mechanical shift can be

measured with good accuracy by inspecting data sinogram. Sinogram is constructed by extracting a column of the detector matrix from every projection and stacking columns together to form an image. An example sinogram, obtained from a 5 parallel capillaries phantom data set is shown in Fig.5.17. Five capillaries were located on a piece of card board parallel to each other. Phantom was placed inside the animal support table and scanned over 360 degrees. Slices perpendicular to the direction of capillaries projection were taken in every view and stacked together.

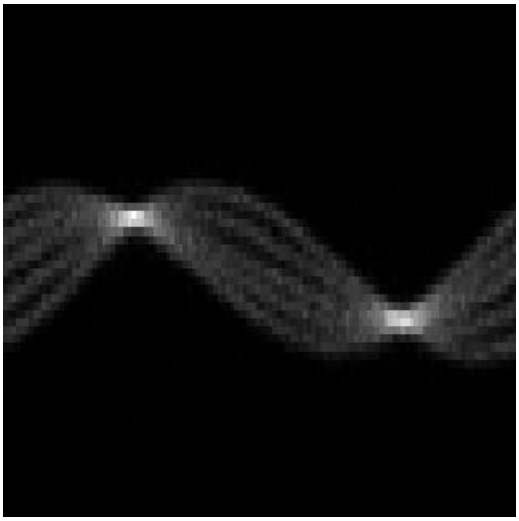

Fig.5.17.*Sinogram obtained from a scan of 5 parallel capillaries*

The amplitude of oscillation of a capillary image is equal to mechanical shift, multiplied by magnification factor. Such sinograms can be constructed for any object with discreet structure, but for continuous objects like animals a pre-scan of a capillary phantom is performed.

Slices through reconstruction volumes of a full- and half-cone scans are presented in Fig.5.18.

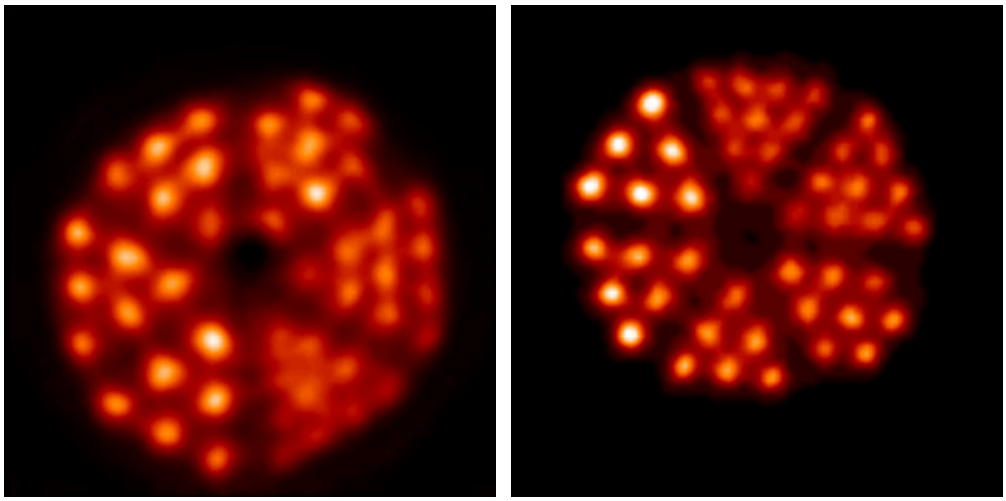

(a) (b)

Fig.5.18.*Axial slices through reconstructed volumes full-cone (a) and half-cone (b)*

All six groups of hot rods can be resolved in both images. Half-cone acquisition resulted in less noisier reconstructed image. To illustrate importance of precise knowledge of mechanical shift an intentional error of 1 mm was made in reconstruction program input. Resulting axial slice is shown in Fig.5.19. Rods can not be resolved in any group.

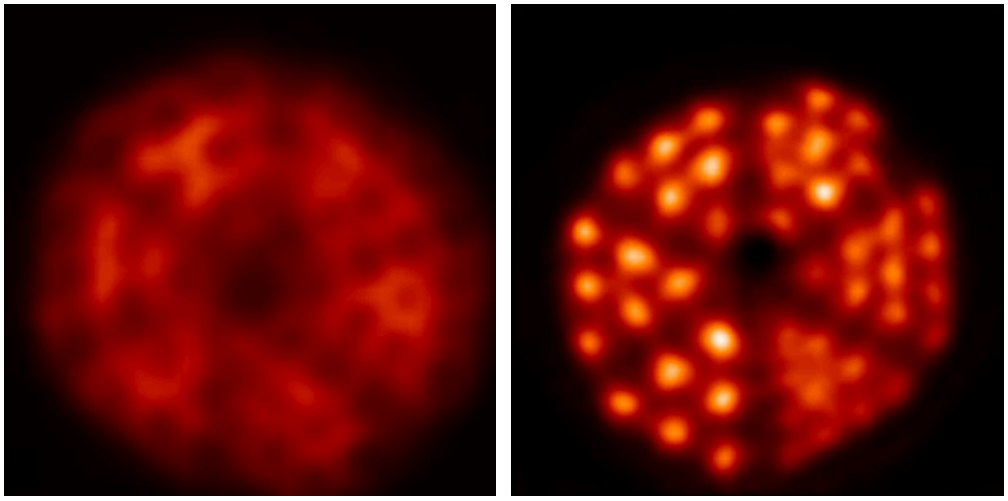

(a) (b)

Fig.5.19.*Full-cone geometry data set, (a) error of 1 mm in mechanical shift, (b) correct value of mechanical shift*

5.2.2 Live animal imaging

Imaging of a mouse, injected with ~ 2.5 mCi of Tc-99m-labeled MDP, was performed with both acquisition geometries. The same pinhole collimators were used as with imaging of microSPECT phantom. Imaging was done two hours following the injection of radioisotope. Geometric arrangement was the same as described above. Total acquisition times were 67 and 34 minutes for full-cone and half-cone geometries respectively. Fig.5.20 exhibits slice through the reconstructed volumes.

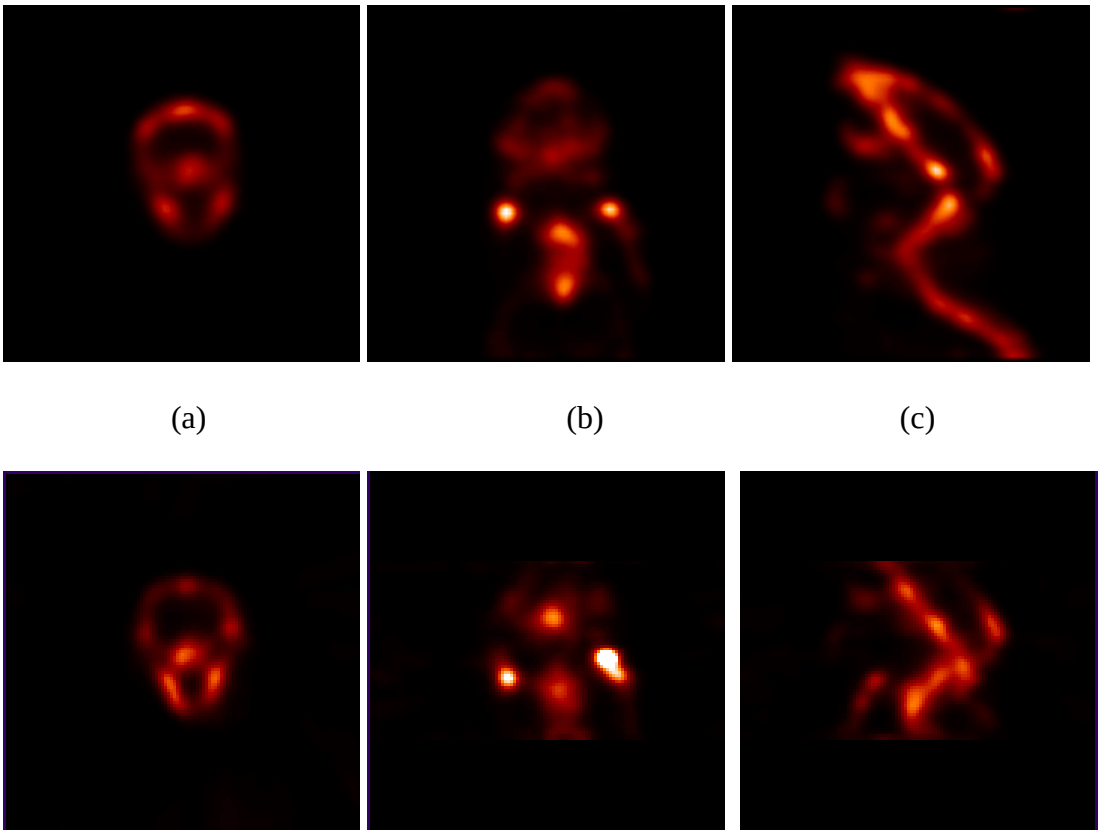

(a) (b) (c)

(d) (e) (f)

Fig.5.20.*Axial, coronal and saggital slices through reconstructed volumes of full-cone data set (a), (b) and (c); half-cone data set – (d), (e) and (f)*

Both geometries were able to capture details of mouse skeletal structure. Half-cone geometry showed reduced field-of-view, as expected from using only one camera pair.

5.3 Dual modality scanning

Having demonstrated that the scanner can successfully acquire data with both imaging modalities we can now progress to the final step of dual modality scanning – obtaining images of the same object from both modalities and merge reconstructed volumes.

An imaged object is placed on a table, which slides along a cut-out in the table support tube. So object motion between two modalities is minimal. Therefore we opted for a rigid geometry type of data merging [5], [6]. The method relies on imaging a phantom with some features, which can be recognized in both modalities. A technical drawing of such a phantom is shown in Fig.5.21. The phantom is a plastic tube with a pattern of holes drilled on tube's outer surface. The hole pattern consists of 5 equidistant holes arranged in a straight line, running parallel to tubes symmetry axis, and 8 angularly equidistant holes along the circumference of the tube. The central hole in a line arrangement coincides with a hole in a ring arrangement, so a total of 12 holes are drilled. Those twelve holes are used to define a Cartesian coordinate system in reconstruction volumes of both modalities with certain amount of redundancy to check merging alignment. Two such phantoms were manufactured to be used on animal tables of different sizes.

Before imaging, the phantom holes are filled with the mixture of barium sulfate powder and solution of Tc-99m. Barium sulfate powder is used routinely as CT contrast agent in human and animal scans, so it provides sufficient amount of attenuation of x-ray beam to

be visible in the reconstructed CT images. One of the linearly arranged holes is left empty to provide a reference in image orientation.

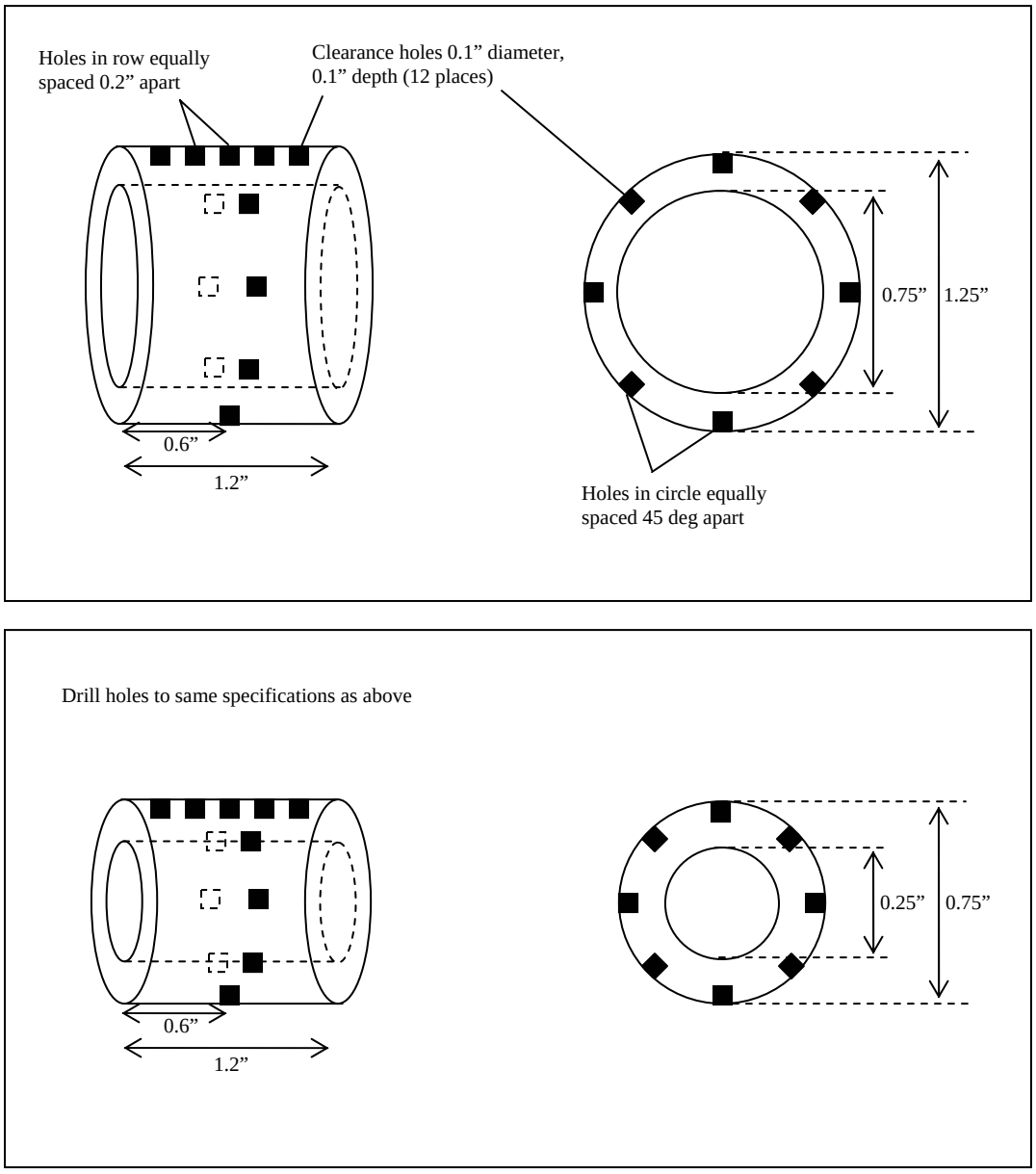

Fig.5.21.*Technical drawing of merging phantoms*

After imaging a phantom with both modalities, reconstructed volumes are processed using the software package ASI Pro. A snapshot of the program interface is shown in Fig. 5.22.

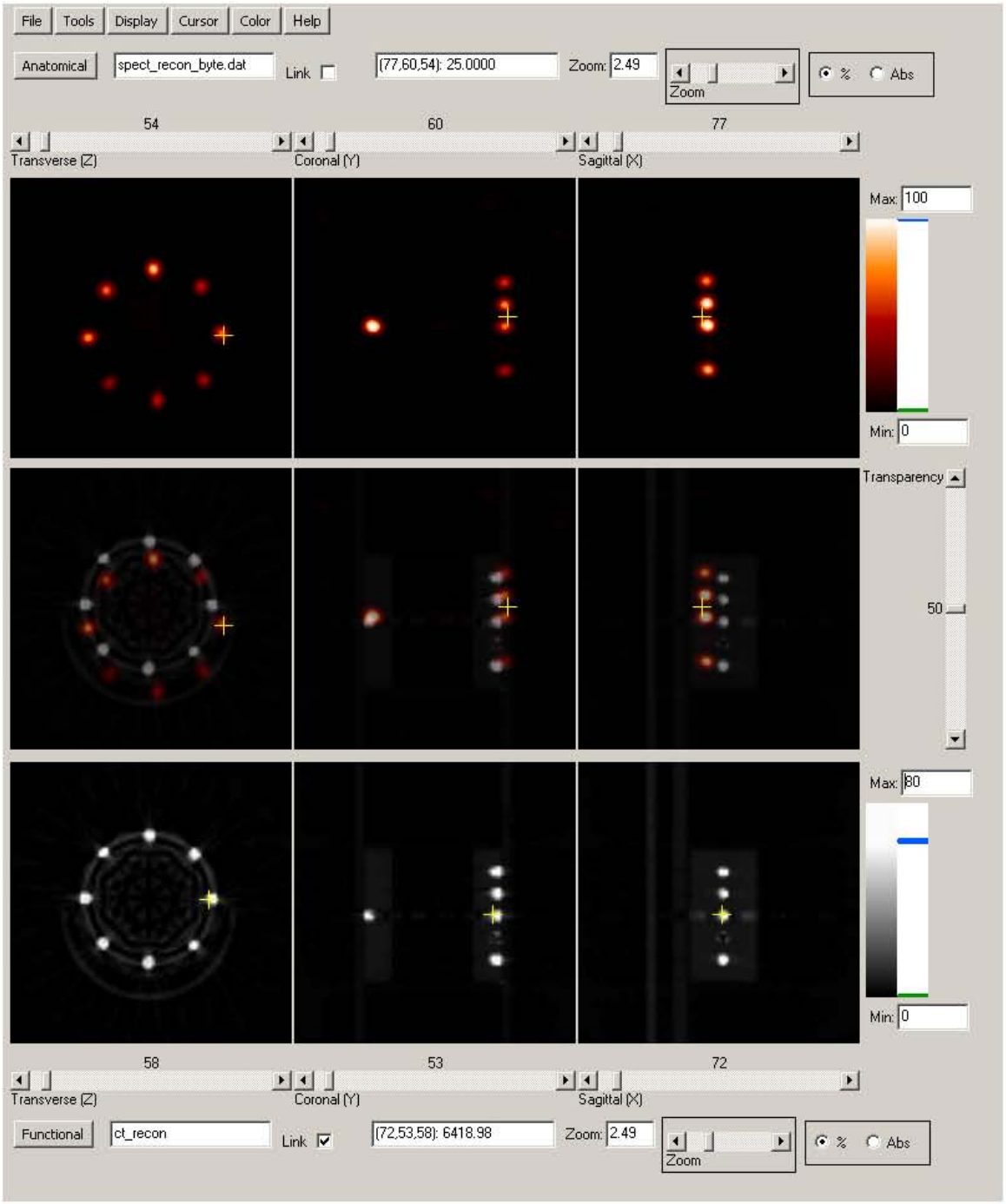

Fig.5.22.*Snapshot of ASI Pro data processing software*

Both volumes are loaded into the program and re-binned to a common voxel size. Images from one modality (usually SPECT) are translated and rotated until sufficient amount of alignment is achieved. Maximum intensity projection of phantom's merged volume is shown in Fig.5.23.

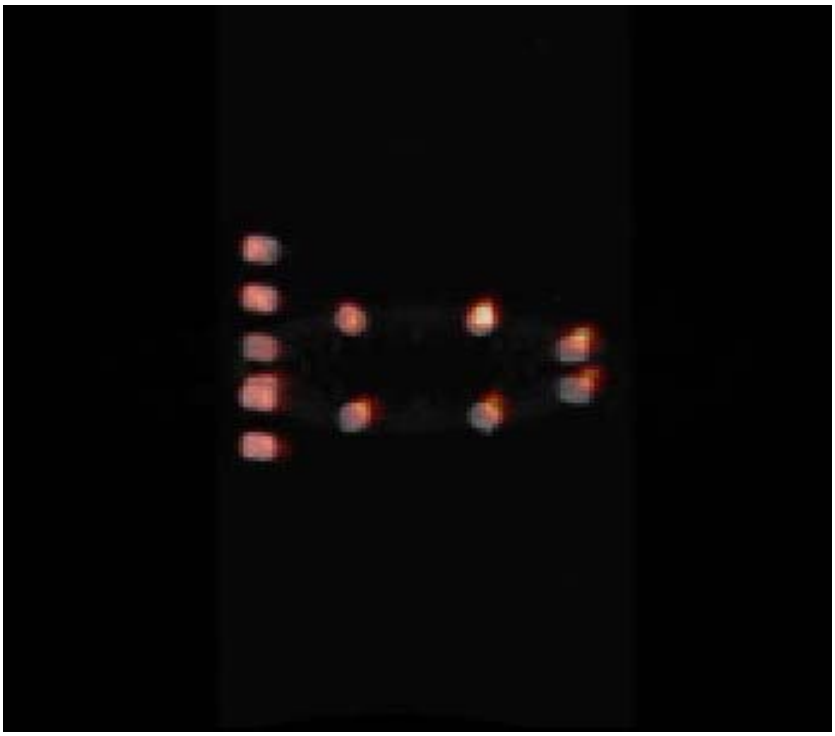

Fig.5.23.*Maximum intensity projection of dual modality merging phantom*

The program keeps track of every image manipulation and once the volumes are aligned, a simple text file with a sequence of translations and rotations is saved on a PC hard drive. Provided there are no alterations in the scanner geometry, the sequence of geometrical transformations can be applied to any other dual modality scans.

The results of first of such scans are shown in Fig.5.24. After acquiring SPECT data of microSPECT phantom, the phantom was translated into the field of view of CT system and a data set was acquired. Transformation parameters saved from the previous operation were applied to the reconstructed volumes.

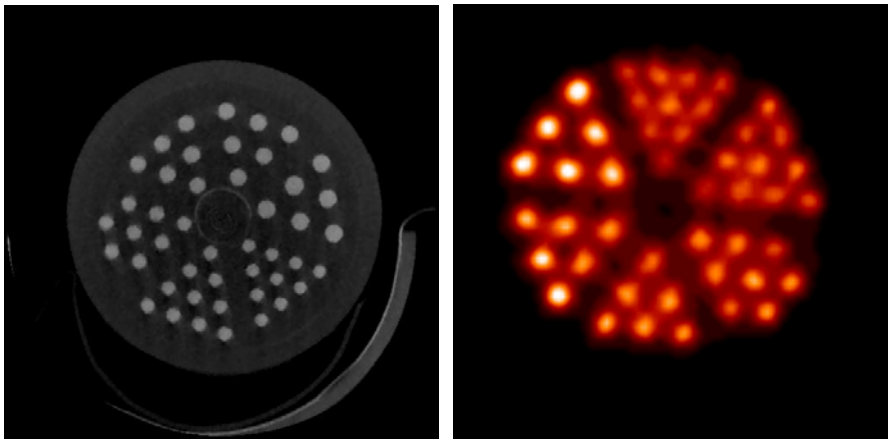

(a) (b)

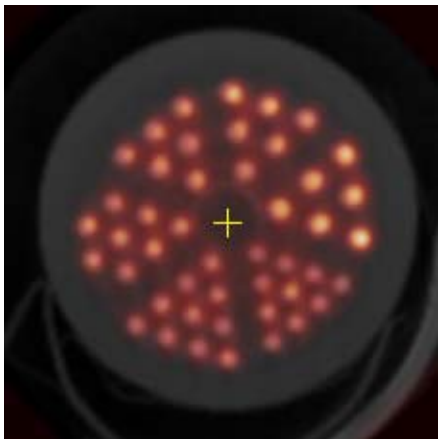

(c)

Fig.5.24.CT (a), *SPECT (b) and merged (c) axial slices through microSPECT phantom reconstructed volume*

Merging process resulted in a well-aligned dual modality images. So a final step was taken – an *in vivo* study of a live mouse. A mouse was injected with ~ 0.65 mCi of Tc-99m-Sestamibi compound. Imaging was done immediately after administering injection. SPECT data was obtained using full-cone acquisition geometry. Pinhole with

0.5 mm diameter was used. 60 frames over 360 degrees scan angle were obtained at magnification factor of 2.3. Fig.5.25 displays results of this scan.

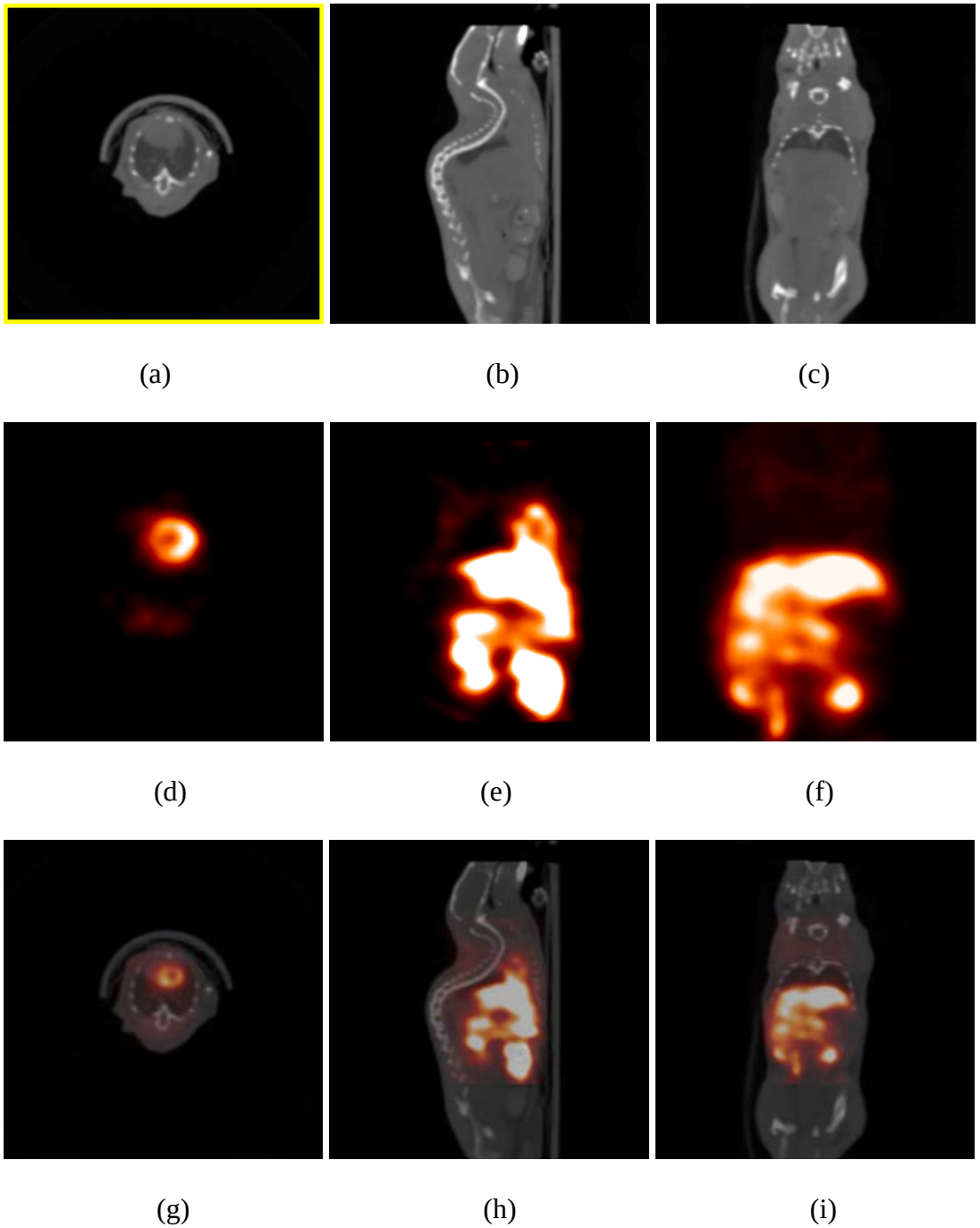

(a) (b) (c)

(d) (e) (f)

(g) (h) (i)

Fig.5.25.*Axial (a),(d),(g); saggital (b),(e),(h); and coronal (c),(f), (i) slices through the CT, SPECT and dual modality reconstructed volumes respectively*

Although most of the activity accumulated in the abdominal region, mouse heart can be clearly identified in the merged axial slice. Gastro-intestinal system can also be viewed in the combined image.

Some general conclusions can be drawn from presented data. We were able to demonstrate possibility of acquiring and reconstructing high spatial resolution data in both CT and SPECT modalities. SPECT system can be operated in two different geometric arrangements, which can be chosen based on the application requirements. SPECT modality is able to resolve objects separated by 2.4 mm center-to-center distance and 1.2 mm active area – to – active area distance. X-ray CT system can provide ultra-high spatial resolution images for both *in vivo* imaging and extracted sample scanning. We were able to successfully merge data from different modalities to present images, where functional information provided by SPECT is overlaid on a structural map of the object obtained from an x-ray CT scan.

References

[1] L. M. Logory, D. R. Farley, A. D. Conder, E. A. Belli, P. M. Bell, P. L. Miller, "Characterization of an x-ray framing camera utilizing a charge coupled device or film as recording media", Rev. Sci. Instr., vol. 69, no. 12, 1998

[2] Glenn D. Boreman, "*Modulation Transfer Function in Optical and Electro-Optical Systems*, SPIE PRESS, Tutorial Texts in Optical Engineering, Volume TT52, Washington, 2001.

[3] Feldkamp L.A., Davis L.C., Kress J.W., "*Practical cone-beam algorithm"*, J. Opt. Soc. Am., vol.1, pp. 612–619, 1984

[4] K. Lange, R. Carson,"EM reconstruction algorithms for emission and transmission tomography," *J. Comput. Assisted Tomogr.*, vol. 8, pp.306–316, 1984

[5] Jia Li Koral, K.F., "An algorithm to adjust a rigid CT-SPECT fusion so as to maximize tumor counts from CT VoI in I-131 therapies", IEEE Nucl. Sci. Symp. Conf. Rec., vol.3, pp.1432 – 1436, 4-10 Nov. 2001

[6] Meei-Ling Jan et.al., "A three-dimensional registration method for automated fusion of micro PET-CT-SPECT whole-body images", IEEE Trans. Med. Imag., vol. 24, no 7, pp. 886 – 893, July 2005

CHAPTER 6
Summary, conclusions and future work

6.1 Summary and conclusions

This work covers design and implementation of a dedicated dual modality small-animal CT/SPECT scanner. An open-barrel type gantry was chosen to permit easy rearrangement of imaging components to optimize data acquisition strategy for a specific imaging task. Imaging characteristics of individual components were evaluated. Analysis of x-ray detectors' performance was carried out to determine their basic imaging characteristics and determine their applicability to small-animal imaging. It was found that the CCD-based detector exhibited superior imaging properties to that of the CMOS flat panel detector. Dynamic range of the CCD detector turned out to be 4240 compared to 990 for the CMOS array. Larger dynamic range translates into a wider variety of tasks, which detector can be employed in. Spatial resolution, measured by the detector modulation transfer function, was also higher for CCD detector. CCD detector's 10% of MTF value was found to be 16 cycles/mm, compared to 4.5 cycles/mm for CMOS. Finally, detective quantum efficiency of CCD and CMOS detectors was measured and CCD again came out on top of the competition, dominating overt the major portion of frequency range.

Two x-ray sources were identified and incorporated into the scanner. X-ray shutter was installed on one of the sources to allow for fast delivery of x-rays. Detectors and

sources were installed on the gantry and the system resolution limits were estimated by calculating contrast value for two acquisition geometries. Big Chip and Hamamatsu detectors were able to resolve 20 lp/mm and 10 lp/mm respectively at the axis of rotation, and for magnification factor of ~ 7 their MTF values at 20 lp/mm were found to be 24.5 % for Hamamatsu and 57.9 % for Big Chip detector.

Imaging characteristics of gamma detector were measured. The detectors were found to perform very similarly. Their intrinsic spatial resolution turned out to be around 1.7 mm, energy resolution around 20 % and detecting efficiency about 40%. Comprehensive study of imaging performance of a pinhole collimator was presented. It was found advantageous to use pinholes with full opening angles of 60 degrees or less. It was determined that for sources located at angles about 30 degrees with respect to pinhole axis collimators' sensitivity drops and depth of interaction effect overpowers effective pinhole closing, reducing spatial resolution. As a result of the study, new data acquisition geometry for SPECT was introduced. Square shape pinhole collimators, as the best possible solution for data completeness problem in half-cone geometry with conventional collimators, were characterized. Analytical model proved to be impossible to implement, thus simulation was performed. It was found that a square pinhole of 1 mm wide opening has about 23% efficiency than a conventional round pinhole of the same diameter. Simulations showed that sensitivity and spatial resolution of a square pinhole do not vary with azimuthal position of the source. As a result of our investigations square pinhole collimators inserts were employed.

Scanner alignment procedures were carried out resulting in axis of rotation localization to within 400 microns. Calibration procedure for CT system was successfully

implemented using in-house designed phantoms and commercial software. SPECT calibration did not yield satisfactory results, but it was demonstrated that mechanical shift can be determined precise enough to reconstruct data without significant artifacts.

Tomographic data sets of phantoms on both modalities were obtained and reconstructed. Spatial resolution of the SPECT system was estimated to be around 1 mm.

Live animal scans were performed on both modalities. It was determined that the scanner is able to image live animals. Data merging process was presented. Finally, fused images of real *in vivo* experiment were produced.

6.2 Future work

6.2.1 Improvements on existing hardware

Although fully functional in its present state, the performance of the scanner will benefit from some extra effort. Most immediate need is the completion of gamma part according to the intended design. Gamma detector 4 needs to be assembled, tested, calibrated and installed. This task will be accomplished in the very near future. Precise calibration of the gamma subsystem geometry, under investigation at the present moment, is expected to improve quality of reconstructed images. Big Chip detector is scheduled to undergo some modifications to improve read-out speed, so it can be used for *in vivo* studies. There is a demand for cardio activity gated x-ray CT imaging. It is possible to implement that in the current scanner if a fast enough x-ray beam shutter can be identified. Finally, new design for a sample rotating hardware needs to be implemented to increase magnification of x-ray CT setup.

6.2.2 Future expansions of the scanner

Flexible design of our scanner allows for easy expansion of the system. Two very interesting projects are already in progress.

6.2.2.1 Ultra-high resolution gamma detector

The UVa Detector Group is collaborating with Lintech Inc on constructing an ultra-high spatial resolution gamma camera. This detector is based on the next generation of position sensitive photomultiplier tubes. Hamamatsu H 9500 PSPMT, the basis of the new detector, has four times the number of anode pads than the previous version, which is installed in our cameras. Detector will utilize a single phototube coupled to an array of CsI crystals with center-to-center spacing of 0.9 mm. Fine signal sampling and small detector element size should provide very high resolving ability. Ultra high spatial resolution detector is sought after in a variety of small animal research projects. Our camera is planned for immediate use in imaging of formation of vulnerable plaque in mouse arteries, one of the hottest topics in small animal research these days. Design of housing, collimator and mounting options as well as software development are ongoing projects in our lab.

6.2.2.2 Monochromatic *x-ray CT*

Another project, that our group is involved in, is to incorporate a source of monochromatic x-ray radiation and a dedicated x-ray detector. Monochromatic source is always preferential, since it allows for scatter rejection and eliminates effect of beam hardening. Initial testing of a monochromatic x-ray filter prototype, developed by MXF

Technologies (College Park, Md), was performed in our lab. Intended primarily for digital mammography applications, this filter can be coupled to a microfocus x-ray tube and used in small animal imaging. Our tests showed that the prototype filter can deliver a fan beam of 20 keV x-rays with energy uncertainty of 2 keV FWHM. This filter is a highly attenuating device, so x-ray flux may not be high enough for existing detectors. Our group is developing a dedicated x-ray detector, using commercially available photodiode array. This project promises an improvement in small animal CT image quality and when combined with an ultra-high resolution SPECT data will take performance of our scanner to a new level.